Nano-structured Materials using ICP-CVD Nanotechnology Process

Lee Yi Chau

School of Electrical & Electronics Engineering

A thesis submitted to the Nanyang Technological University

in partial fulfillment of the requirement for the degree of

Doctor of Philosophy

2010

Acknowledgements

I would like to extend my sincere gratitude to my supervisor, Prof. Tan Ooi Kiang for the encouragement, guidance and support rendered by him throughout the whole course of work. His wide knowledge, foresight and methodology in this area of research have been of great value for me.

I wish to express my warm and sincere thanks to Assoc Prof Tse Man Siu for his invaluable advice and discussion especially on the hardware setup and design of experiments.

I am greatly indebted to Dr. Huang Hui for his guidance, constructive comments and extensive discussions around my work. I would like to express my special thanks to Dr. Huang Hui, Ms. Fang Xiaoqin, Ms. Guo Jun, for their help on the XPS and TEM characterization.

I want to thank the laboratory executives of Sensors & Actuators Lab, as well as the staff of Microfabrication Lab for their technical support and the kind help rendered at different stages of this work. I would also like to express my sincere thanks to Dr. Hu Ying, Dr. Sun Lingling, the graduate and undergraduate students at the Sensors & Actuators Lab for their help and support throughout the project.

I would also like to acknowledge the financial support from A*STAR and NTU in this research work. Last but not least, I wish to thank my family for their unwavering love and encouragement that have kept me going with my pursuit.

Table of contents

Summary

Nanostructured materials are anticipated to revolutionize the various technological fields with their unique novel properties. The research on metal oxides gas sensors has benefited from the materials at nano-scale with their better sensing performance than the conventional bulk materials. Currently, the novel synthesis of quasi one-dimensional (1-D) nanostructures, the various strategies to improve the selectivity and the design for manufacturability of the nanostructures are the three directions pursued by the researchers in this field.

In this thesis, a custom-designed inductively coupled plasma-chemical vapor deposition (ICP-CVD) was used to prepare different types of SnO_2 nanostructures for gas sensing applications. For the nanocrystalline SnO_2 thin films prepared using bubbler delivery of chemical precursors, the effects of substrate-nozzle distance, RF power, and gas flow ratio of Ar/O_2 on the structural properties were systematically studied. The gas sensing response of the SnO_2 thin films deposited at various substrate-nozzle distances was characterized.

Hybrid structure of 1-D SnO_2 nanorods formed on two dimensional (2-D) SnO_2 thin films were successfully prepared by subjecting the as-deposited SnO_2 thin films to post plasma treatment using the same ICP-CVD system. The effects of RF power, gas flow ratio of Ar/O_2, and type of plasma on the formation of nanorods were studied. A sputtering-redeposition mechanism was proposed to explain the growth of SnO_2 nanorods on 2-D thin film. The sensitivity to CO, H_2 and ethanol of the hybrid SnO_2 nanorods thin film was found to enhance by twofold and above, together with a significant decrease in optimal operating temperature up to 130 °C compared to the as-

deposited SnO_2 thin films. Surface addition with Pd noble metal further improved both the sensitivity and selectivity of the SnO_2 nanorods thin film towards H_2 gas with 6 times better sensitivity compared to the un-doped SnO_2 nanorods thin film.

Direct one-step SnO_2 nanorods array was successfully prepared using a reduced flow rate of carrier gas and oxygen. The effects of substrate-nozzle distance and RF power on the nanorods array formation were studied and a growth mechanism based on vapor-solid growth was proposed. The gas sensing properties of the as-deposited and Pd-doped SnO_2 nanorods arrays were studied, with the latter showing 6 times better sensitivity to H_2 at a reduced optimal temperature of 400 °C. Both the post thermal annealed and post oxygen plasma treated SnO_2 nanorods arrays showed improved sensitivity to CO and H_2 compared to the as-deposited nanorods array, in particular the 40-minutes post oxygen plasma treated sensor exhibited 13 times higher sensitivity to H_2. The role of oxygen vacancies and chemisorbed oxygen species for the improved gas sensing properties were substantiated by the XPS characterization results.

SnO_2 nanocolumns array was successfully prepared with the use of direct liquid injection ICP-CVD. The effect of substrate-nozzle distance on the formation of nanocolumns array was studied. The gas sensing properties of nanocolumn arrays showed similarity with that of the nanorods array. The role of chemisorbed oxygen in optimizing the gas sensor response was elucidated by the XPS analysis.

List of Figures

List of Tables

CHAPTER ONE

INTRODUCTION

1.1 Motivation

The famous visionary lecture, "There's Plenty of Room at the Bottom", by the late physicist and Nobel laureate Richard Feynman in 1959 has planted the seed of nanotechnology research with his view on the possibility to manipulate matter on the atomic scale. The explosion in both academic and industrial interests in this burgeoning scientific discipline over the past two decades has seen a vast amount of literature devoted to the development and study of nanotechnology. The topics range from fundamental study at atomic scale behavior [1,2] to the introduction of novel nano-fabrication routes [3,4] and demonstration of nanostructured materials applications in a wide variety of technological areas [5-8]. The core of nanotechnology, nanostructured materials, distinguished by its length scale between 1 to 100 nm in at least one of the three dimensions [9,10] have shown novel electrical, mechanical, chemical and optical properties not previously attainable with conventional bulk materials, which are largely believed to be the result of surface and quantum confinement effects [11,12].

In the field of semiconductor metal oxide gas sensors, nanostructured materials present new opportunities in enhancing the properties and performance of gas sensors owing to their much higher surface-to-bulk ratio in nanomaterials compared to coarse micrograined materials. Current yearly production of semiconductor type gas sensors in the world is estimated to be around 20 million pieces [13]. These remarkable figures signify that the gas sensor technology is important in our society to address the increasing concerns with pollution on our health and safety. The mechanism for gas detection in these materials is based, to a large extend, on the reactions that occur at the sensor surface, resulting in a change in the concentration of adsorbed oxygen. This gives rise to conductivity change of the materials as the sensing response. As an inverse relationship exists between surface area and particle size, nanostructured materials thus become favorable to improve the sensing properties. In 1991, Yamazoe and co-workers [14,15] showed that reduction of crystallite size greatly enhanced the sensor performance. For porous sintered SnO_2 elements fabricated with pure SnO_2 and foreign-oxide-stabilized SnO_2 in the crystallite size range of 5 – 32 nm, they found that the sensitivity towards target gas species of H_2, CO and i-C_4H_{10} increased steeply as the crystallite size decreased to 6 nm or lower.

The recent decades have seen the progressive development from the early form of bulk SnO_2 ceramic to thin film type gas sensors owing to the trend of miniaturization in electronic components. The utilization of silicon manufacturing technology in the fabrication of gas sensor, by physical and chemical vapor deposition, is promising to achieve small size, low cost, low power consumption, high reproducibility and multi-sensor gas detection systems. However, technological improvement went along with a reduction of sensing performances due to a lower porosity of the prepared devices.

Besides that, the stability of the nanostructures has been a challenging issue to address since the relatively high operating temperature of metal oxide sensors for surface reactions to take place induces grain growth by coalescence, resulting in the drift of the sensor output [16]. More recently, the successful preparation of stable single crystal one-dimensional (1-D) and quasi 1-D semiconducting oxides nanostructures (so-called nanobelts, nanowires, nanorods, or nanoribbons) [17-20] has spurred new ideas to improve the stability of nanostructures for gas sensing. The 1-D nanostructures are very promising for gas sensors due to the fact that the surface-to-volume ratio is very high, the oxide is single crystalline, the faces exposed to the gaseous environment are always the same and the size is likely to produce a complete depletion of carriers [21]. The possibility to functionalize the surface of 1-D nanostructures with a target-specific receptor species [22], modulation of their operating temperature to select proper gas semiconductor reactions [23], and the potential of field-effect transistors (FET) configuration that allows the use of gate potential controlling the sensitivity and selectivity [24] have also drawn remarkable interests in these materials.

Various synthesis methods have been reported to prepare 1-D SnO_2 nanorods and nanowires, such as evaporation-condensation method [25], chemical vapor deposition [26,27], pulsed laser deposition [28], hydrothermal synthesis [29], thermal evaporation [30], and spray pyrolysis [31]. However, the integration of individual or arrays of 1-D nanostructures with planar technology still poses a major challenge for the realization of functional devices that can be mass produced at reasonably low cost. In this work, a custom-designed inductively coupled plasma-chemical vapor deposition (ICP-CVD) system, which is readily compatible with silicon manufacturing, has been adopted to

study the preparation of various SnO_2 nanostructures for gas sensing application. The effects of processing parameters, the growth mechanism of nanostructures, together with their sensing properties and strategies to enhance the performance of the fabricated sensing devices are investigated and discussed.

1.2 Objectives

In this thesis, the main objectives are:

1. To deposit SnO_2 nanostructured thin films using the custom-designed ICP-CVD system. The processing window of the deposition is then characterized by systematically investigating the effects of process parameters on structural properties of the thin films. The structural properties are characterized using X-ray diffraction (XRD), field-emission scanning electron microscopy (FE-SEM), and transmission electron microscopy (TEM).
2. To modify the microstructures of the as-deposited nanostructured thin films by subjecting the thin films to post plasma treatment using the same setup. The aim is to increase the surface area for gas adsorption in gas sensing application. The effects of processing parameters on plasma-treated thin films are investigated to formulate the growth mechanism of the plasma-modified nanostructures.
3. To fabricate the SnO_2 nanostructures into sensor devices with interdigital Au electrodes using electron beam evaporation. The gas sensing properties to reducing gases like CO and H_2 can then be characterized using an in-house gas sensing characterization system based on direct current (dc) electrical measurement. This also leads to the study on possible enhancement of gas sensing properties by surface addition of Pd noble metal and microstructures

modification using post plasma treatment for the ICP-CVD derived SnO_2 nanostructures.

1.3 Major contributions to the thesis

The major contributions achieved in this research work are summarized as follows:

1. Nanocrystalline SnO_2 thin films have been successfully deposited by ICP-CVD system using both bubbler delivery and direct liquid injection of the chemical precursors. Structural characterization by XRD indicated the tetragonal rutile Cassiterite SnO_2 phase with grain size in the range of 5 – 45 nm depending on the processing parameters.
2. Hybrid structure of 1-D SnO_2 nanorods grown on two-dimensional (2-D) SnO_2 thin films have been successfully prepared by subjecting the as-deposited nanostructured SnO_2 thin films to post plasma treatment using the same ICP-CVD setup. The two-step processing has increased the surface area of the nanostructures via plasma surface modification. A sputtering-redeposition mechanism has been proposed to explain the formation of nanorods on the thin film structure. The sputtered film species generated from the bombardment of Ar ions during plasma treatment rearranged themselves on the films and grew up along their preferential orientation to form nanorods.
3. The gas sensing properties of as-deposited thin films and plasma-treated SnO_2 nanorods grown on thin films have been characterized. Enhanced gas sensing properties have been obtained for the latter owing to the higher surface-to-volume ratio of the hybrid nanorods thin film structure. An improvement of 6.5 times better sensitivity to CO gas, together with a 95 °C reduction in optimal operating temperature has been obtained. The surface modification by plasma treatment has proven to be an effective solution to improve the gas sensitivity of

the SnO_2 gas sensor. Further enhancement by surface addition of Pd noble metal has increased the selectivity of SnO_2 nanorods thin film to H_2 with 6 times better sensitivity compared to the un-doped SnO_2 nanorods thin films.

4. Direct one-step SnO_2 nanorods array has been successfully prepared using the ICP-CVD system. The needle-shape SnO_2 nanorods were directly grown from the SiO_2/Si substrate in random outward direction. A typical SnO_2 nanorods cluster have a diameter of 5 – 16 nm and a length of 160 – 250 nm from TEM observation. The growth mechanism of the nanorods array is attributed to the vapor-solid growth where the initially deposited molecules form a seed layer that serve as the nucleation sites for the subsequent directional growth to minimize the surface energy.

5. The gas sensing properties of SnO_2 nanorods array has been characterized and enhanced gas sensing properties were obtained using noble metal doping of Pd. An improvement of 6 times in sensitivity to H_2 with a reduced optimal operating temperature has been achieved with Pd-doped SnO_2 nanorods array. Post thermal annealing and post oxygen plasma treatment have also shown to increase the gas sensitivity to both CO and H_2 other than Pd doping method. XPS analysis confirmed the change in oxygen vacancies is the contributing factor of post annealed sensor while the increase in chemisorbed oxygen species is responsible for the enhancement of post oxygen plasma treated sensor. It should be highlighted that a 13 times improvement in sensitivity to H_2 has been achieved with the 40-minutes post oxygen plasma treated SnO_2 nanorods array.

6. Direct one step SnO_2 nanocolumns array has been successfully prepared using the direct liquid injection ICP-CVD process. The column-shape nanostructures were found to grow outwardly in random direction at certain substrate-nozzle

distance. Similar gas sensing properties of nanocolumns array to the nanorods array has been attained and the use of post oxygen plasma treatment has proven effective in enhancing the gas sensitivity to both CO and H_2 by 7 times. XPS analysis has again shown the role of chemisorbed oxygen in enhancing the gas sensing properties of nanocolumns arrays.

7. A total of 10 papers have been published and referred in the international journals, 11 papers have been presented in the international conferences, a chapter titled "Low-dimensional nanostructured materials for chemical sensing applications" of a book "Handbook of Nanoceramics and Their Based Nanodevices" has been published, and a chapter titled "Growth and properties of nanorod arrays" of a book "Encyclopedia of Nanoscience and Nanotechnology" has been accepted and in press.

1.4 Organization of the thesis

The thesis is organized into six chapters in the following manner:

In chapter one, the motivation, objectives, main contributions, and organization of the thesis are presented.

Chapter two presents the background theory on semiconducting metal oxide gas sensors, including their working principles, methods in improving sensitivity and selectivity, as well as the current status and problems of SnO_2 gas sensors. A brief background on plasma-enhanced chemical vapor deposition with emphasis on the deposition mechanisms and inductively coupled plasma sources is also presented.

In chapter three, the experimental procedures used in this research work are presented, starting with the description on the various functional modules of the custom-designed ICP-CVD system. Next, the structural and gas sensing characterization techniques for the prepared SnO_2 nanostructures are presented.

Chapter four presents the nanocrystalline SnO_2 thin films prepared by the ICP-CVD system using bubbler delivery of chemical precursors. The effects of process parameters on the structural properties are discussed. The gas sensing properties of the nanocrystallline SnO_2 thin films are presented.

Chapter five presents the formation of nanorod SnO_2 thin films by post plasma treatment, together with the effects of plasma processing parameters and growth mechanism. The gas sensing characterization results of the SnO_2 nanostructures, both as-deposited and post plasma treated are compared and described in detail.

In chapter six, the preparation of direct one-step SnO_2 nanorods/nanocolumns array is presented. The effects of process parameters on the microstructures and the associated growth mechanism are discussed. The gas sensing properties of the SnO_2 nanorods array, with emphasis on the improvement strategies besides noble metal doping, i.e. thermal annealing and post oxygen plasma treatment are discussed based on the XPS analysis results.

Finally, the conclusions and recommendations for the future work are listed in chapter seven.

CHAPTER TWO

BACKGROUND

2.1 Chemical sensors

A chemical sensor is a device that transforms chemical information, ranging from the concentration of a specific sample component to total composition analysis, into an analytically useful signal [32]. It is made up of two basic functional units, namely the receptor part and the transducer part. In the receptor part of a sensor, the chemical information is transformed into a form of energy which can be measured by the transducer. The transducer part is responsible in transforming the energy carrying the chemical information about the sample into a useful analytical signal.

Based on the detection principles of chemical sensors, they can be classified into electrical, thermal, mechanical, and optical sensors. For the sensors based on electrical properties, the output signal is either generated by a reaction involving charge transport or is modulated by the reaction. For example, electrochemical gas sensors rely on the conductance changes caused by an electrical current passing through the electrodes during interaction with the gaseous compositions. Chemical sensors based on thermal properties measurements are mostly used to detect flammable gases because of the exothermic character of their reaction with oxygen. The devices are

often referred to as pellistors, which typically consist of a catalytic material enclosing a temperature sensor and a heater. The increase in temperature of the catalytic material due to combustion of flammable gas is detected by the temperature sensor. For mechanical type of gas sensors, surface acoustic wave (SAW) sensors detect the changes to the mass of the sensors surface upon exposure to the gas atmosphere under investigation. Optical gas sensors detect the changes in light properties such as absorbance, reflectance, fluorescence, light scattering or refractive index as their sensing response. A fibre-optic chemical sensing device for example consists of a light source, a fibre coupler to lead the light into the fibre, the light guide, a decoupler, and a light detection and amplification system.

An ideal chemical gas sensor should possess high sensitivity towards chemical compounds, high selectivity, high stability, high reproducibility and reliability, short reaction and recovery time, and low power consumption [33]. Among the large variety of sensors available, the conductometric gas sensors based on semiconducting metal oxides remain a widely used choice for flammable and toxic type of gases because they can be made very small and cheap and are compatible with silicon technology, which opens up the possibility to integrate the sensors in the processing electronic circuit. They can be classified as n-type or p-type according to the direction of the conductance change upon exposure to reducing gases. N-type materials (e.g. SnO_2, ZnO, and In_2O_3) show an increase in conductance while p-type materials (e.g. Cr_2O_3 and CuO) show a decrease in conductance during their interaction with the reducing gases. This classification is based on the dominant charge carriers (electron or hole) at the surface of the oxides that determines the surface conductivity type of the oxides [34].

The idea of utilizing semiconductors as gas detection devices dates back to 1953 when Brattain and Bardeen [35] first reported the change in electrical conductance of Ge with the adsorption of gases onto its surface. It was not until Seiyama and co-workers [36] that applied this knowledge for gas detection using ZnO in 1962. The first commercial gas sensors based on SnO_2 was developed by Taguchi [37] not long after the work of Seiyama. SnO_2 has since emerged as the most widely used metal oxide material in gas sensors ranging from domestic gas detectors to breath alcohol analyzers, automatic cooking control in microwave ovens, air quality in parking garages, and fire alarms [38]. Much technological effort has been made in this field, aiming at improvement in gas response, selectivity, stability, and feasibility for practical use.

2.1.1 Working principle of metal oxide gas sensors

According to Yamazoe [15], for conductometric gas sensors based on semiconducting metal oxides, the receptor function is associated with the ideally specific interaction of the surface with the target analyte that leads to the recognition of a particular gas species, whereas the transducer function refers to an effective transduction of this molecular information into a macroscopically accessible output signal, i.e. the change of the electrical conductance.

The most widely accepted explanation for the sensing mechanism of a typical metal oxide gas sensor, such as SnO_2 in a commercial Figaro TGS sensor, is that negatively charged oxygen adsorbates play an important role in detecting inflammable gases such as H_2 and CO [39]. In oxygen containing atmosphere without any humidity, oxygen is ionosorbed on the metal oxide surface, forming adsorbates such as O_2^-, O^-, and O^{2-} depending on the temperature. O^- ions, the most reactive with inflammable gases, are

the prevailing adsorbates between 150-400 °C where most metal oxide gas sensors operate [40]. The ionosorbed species act as electron acceptors due to their relative energetic position with respect to the Fermi level, E_F. The presence of negative surface charge (ionosorbed oxygen species) bends the band upward and generates a surface potential barrier, eV_s. The Fermi level is pushed into the band gap of the metal oxide, effectively reducing the charge carrier concentration and thus leading to an electron depletion surface region or so called space-charge layer. This is illustrated in figure 2-1 for negatively charged chemisorbed adsorbate on n-type semiconductor (e.g. SnO_2 material). Both the barrier height of eV_s and the depth of depletion layer depend on the surface charge [41], which is determined by the amount and type of ionosorbed oxygen species. The depth of the depletion layer can be characterized by the Debye length L_D, which is defined as:

$$L_D = \sqrt{\frac{\varepsilon_0 \varepsilon k_B T}{e^2 n_d}} \tag{2-1}$$

where k_B is Boltzmann's constant, ε the dielectric constant, ε_0 the permittivity of free space, T the operating temperature, e the electron charge, and n_d the carrier concentration assuming full ionization. For SnO_2, with $\varepsilon = 13.5$, $\varepsilon_0 = 8.85 \times 10^{-12}$ Fm^{-1}, $n_d = 3.6 \times 10^{24}$ m^{-3}, and $T = 523$ K, the value of L_D is about 3 nm [42].

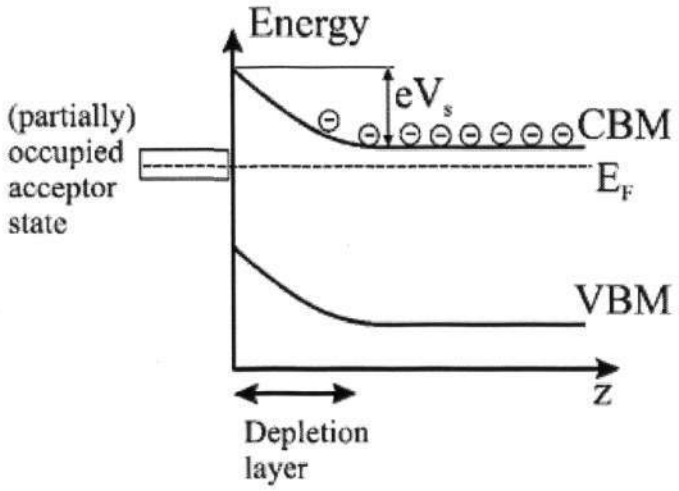

Figure 2-1 Schematic representation of band bending in the near surface region of an n-type semiconductor induced by a (partially) filled donor state of an adsorbed molecule [43].

In polycrystalline sensing materials, electronic conduction occurs via grain-to-grain contacts and therefore the combination of eV_s of each grain with the adjacent grains leads to the formation of Schottky barrier. Figure 2-2 shows schematically the situation that can be found along a grain boundary. The conductance G of the sensing material in such case can be written as:

$$G \approx \exp\left(\frac{-eV_s}{k_B T}\right) \tag{2-2}$$

The conduction electrons have to overcome the barrier to carry the current across the grain boundaries. Reducing gases like CO will react with the ionosorbed oxygen species and remove them through the oxidation process. As a consequence, the height of the Schottky barrier is reduced as the captured electrons are restored to the conduction band, thus resulting in an increase of conductance. The change in conductance is used as the sensing signal in metal oxide gas sensors. The reactions of a typical n-type SnO_2 gas sensor are as follow:

Oxygen adsorption process: $(SnO_2 + e^-) + \frac{1}{2}O_2 \leftrightarrow SnO_2(O^-)_{ad}$ (2-3)

Oxidation by reducing gas: $SnO_2(O^-)_{ad} + CO \rightarrow (SnO_2 + e^-) + CO_2$ (2-4)

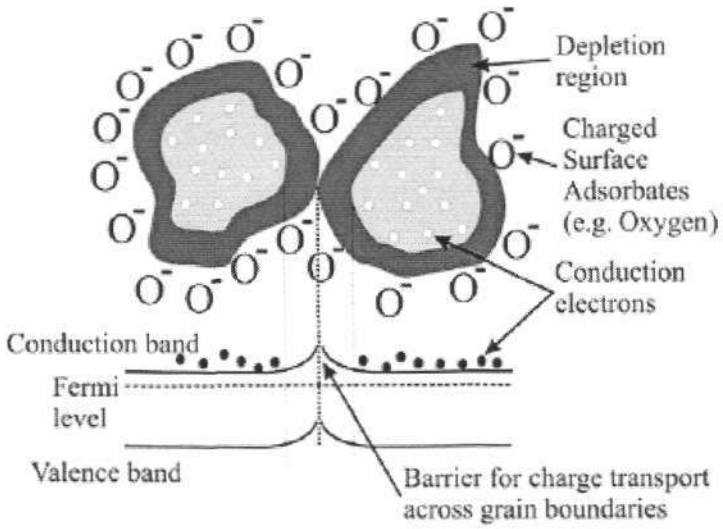

Figure 2-2 Schematic diagram of charge carrier concentration in SnO_2 grains. Negatively charged chemisorbed oxygen species cause an upward band bending and consequently a depletion layer in the near-surface region. This causes a Schottky-like barrier across grain boundaries [43].

Similarly for p-type semiconducting metal oxides, the adsorbed oxygen acts as a surface acceptor state, capturing electrons from the valence band and therefore giving rise to an increase in the charge carrier (hole) concentration at the interface. The grain junctions will have a lower resistivity than the bulk. The presence of reducing gases will result in the opposite effect as in n-type sensing materials, in which the decrease in the surface coverage of oxygen ions will lead to a decrease in the charge carrier concentration and hence, a decrease in the conductance.

2.1.2 Methods in improving sensitivity and selectivity

2.1.2.1 Reduction of grain size to nano-scale

Since the working principle of metal oxide gas sensors is based on the surface reaction between the metal oxide and the gas molecules in the ambient, nanoparticulate metal oxides are anticipated to enhance the sensitivity, as well as the response and recovery

time of the sensor as their higher surface-to-bulk ratio offers more surface reaction sites between the oxygen adsorbates and gas molecules in the ambient compared to conventional microcrystalline materials. Minimizing the radius of the particle down to the range of space-charge layer will lead to the convergence of Schottky barrier at the grain boundaries. With further decrease in radius smaller than the space-charge layer, the depleted zones start to overlap and consequently the electrical properties are predominantly determined by surface states. If the remaining differences of the adjacent Schottky barriers fall below the thermal energy, that is, $eV_s \leq k_BT$, the so-called "flat-band condition" is realized and the energetic difference between surface and bulk vanishes, whereby the conductance is proportional to the difference of the Fermi level E_F and the bottom of the conduction band E_C as depicted in figure 2-3:

$$G \approx \exp\left(\frac{-(E_C - E_F)}{k_B T}\right) \tag{2-4}$$

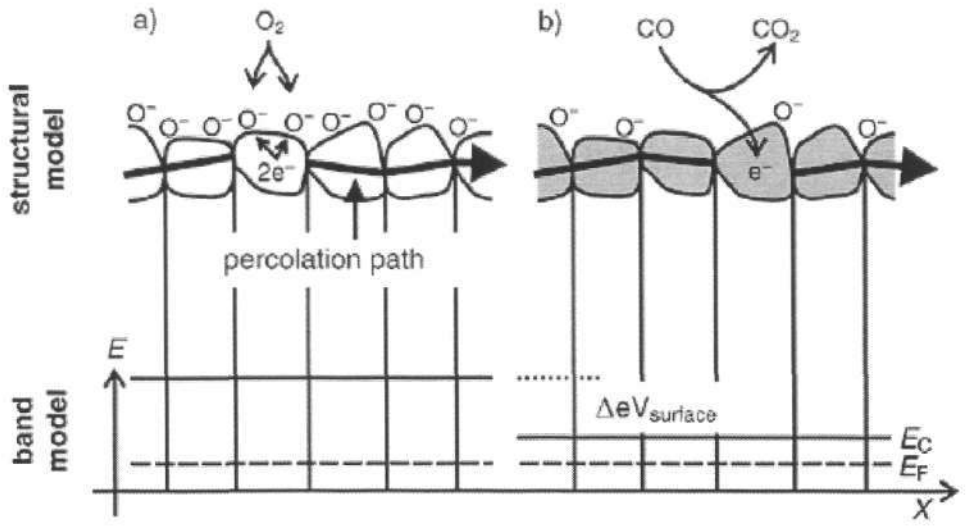

Figure 2-3 Structural and band model for particles with radius less than space charge layer leading to the so-called "flat-band" condition: a) the initial state, and b) the effect of CO on the position of the conduction band E_C [44].

Much work has been done to investigate the effect of grain size on gas sensing. In 1991, Yamazoe and co-workers found a strong correlation between grain diameter D and gas sensitivity for the porous sintered SnO_2 elements in the size range of 5–32 nm [14,15]. The sensitivity to H_2, CO, and i-C_4H_{10} increase steeply as D decreased, especially for the small D region in the range of two times the depth of the surface space-charge layer ($\approx$ 6 nm). When the grain size of the SnO_2 crystalline is close to 6 nm, its resistance increases drastically, resulting from the formation of a space-charge region in the whole crystallite. The amount of oxygen adsorbates per volume of SnO_2 grain increases with decreasing grain size, causing a further increase in resistance [39].

2.1.2.2 Surface addition of noble metals

The promoting effects of noble metals such as Pt, Pd, and Ag have been widely recognized in semiconducting metal oxide gas sensors. It is essentially the addition of catalytically active sites to the surface of the base materials in the form of dispersed clusters, resulting in improved sensing performance in increasing the sensitivity, favoring the selective interaction with the target analyte and thus increasing the selectivity, and decreasing the response and recovery time, respectively, which is then accompanied by a reduction of the working temperature. Furthermore, the surface noble metal addition may enhance the thermal and long-term stability of the sensors. The control parameters involved include composition, size, habit, and redox state of the surface modifiers, as well as their dispersion on and/or into the metal oxide surface.

Two different mechanisms, namely chemical and electronic sensitization as shown in table 2-1, have been applied to explain the promoting effects of surface metal additives. Chemical sensitization comes from the ability of an additive to activate the

inflammable gases by enhancing their spillover. Spillover is a mechanism where the oxidation of the reducing agents can be accelerated on the semiconductor surface in the presence of dispersed metallic catalysts. In semiconductor gas sensor, catalyst such as Pd can increase its resistance in air drastically. Oxygen molecule from the gas phase can be easily dissociated and oxygen atoms migrate to the surface of the metal oxide gas sensor, presumably providing oxygen by spillover. In the presence of reducing gas such as H_2, Pd showed remarkable spillover effect to H_2, thus resulting in tremendously decrease of the resistance. This effect enhances the sensitivity of a sensor significantly and also reduces the response time. The spillover phenomenon is also typical for oxides sensor with surface additive of Pt and Au [44] .

	Chemical sensitization	Electronic sensitization
Model	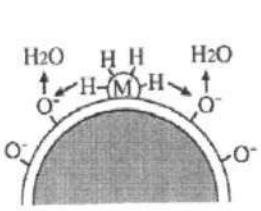	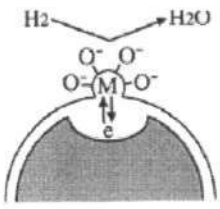
Role of additive Origin of resistance change	Activation of gas followed by spilling over Change in surface oxygen concentration	Acceptor of electrons Change in redox state of additive

Table 2-1 Mechanism of sensitization by metal additive [41].

Electronic sensitization arises mainly from the change in the oxidation state of the loaded metal. Pd and Ag are known to form stable oxides (PdO and Ag_2O) in air [15], which causes the resistance of n-type metal oxides to increase in air. The reason is the electron work function of loaded metal additive is higher than the electron affinity of SnO_2 [39]. This implies that the conducting band energy of loaded metal is lower than the conducting band energy of SnO_2. Hence, electrons on the oxide surface layer are transferred to the metal loaded onto SnO_2 surface, in order to align the Fermi level of

metal and SnO_2. This corresponds to an increase in L_D. When the metal surface is covered with oxygen adsorbates at elevated temperatures in air, i.e. the metal is oxidized, the oxygen adsorbates extract electrons from this metal, which in turn extract electrons from the SnO_2, leading to a further increase in L_D. It means that the additive, not oxygen adsorbed on the surface, controls the depletion layer in the semiconductor. In the presence of reducing gas, consumption of oxygen adsorbates on the loaded metal, in addition to those on the SnO_2 surface, gives rise to the enhanced sensitivity by reaction with the reducing gas.

2.2 Current status and problems of SnO_2 gas sensor

Of all the gas sensing solid state materials, metal oxides were one of the first considered and are still the most widely used. For instance SnO_2 is popular for the detection of reducing and flammable gases. The great interest in SnO_2 is due to its suitable physical and chemical properties, i.e. good adhesion and strong hardness, high stability and resistance to chemical etching under standard conditions, low operating temperatures, relatively low resistivity and high sensitivity that can improved through the introduction of different dopings [33]. The SnO2 gas sensors have evolved from the first generation devices prepared by thick film technology starting from powders to the second generation devices fabricated using thin film technology that offers sensor miniaturization, automated production method and higher batch-to-batch reproducibility. Higher gas sensitivity achieved by the fabrication of sensing material at nano-scale level has identified the role of nanotechnology in the subsequent development of conductometric type SnO_2 gas sensor. Nanotechnology, nowadays, is producing sensing materials in the form of quasi 1-D nanostructures like nanobelts, nanowires, nanotubes, and nanowires. These unique materials with high crystallinity

exhibit improved stability and the nanosized lateral dimension comparable to L_D delivers good sensing properties. The conductivity of the 1-D nanostructures could vary from a fully nonconductive state to a highly conductive state entirely on the basis of the chemistry transpiring at its surface. Their peculiar characteristics and size effects make them a potential candidate as the third generation gas sensor device.

Table 2-2 summarizes the recent work presented in the literature on the 1-D nanostructures of SnO_2 as conductometric gas sensor classified according to the type of 1-D nanostructures.

Type of 1-D nanostructures	Preparation method	Dimension	Gases detected	Working temperature (°C)	References
Mesh of nanowires	Thermal CVD	L: 5-20 μm D: 20-60 nm	NO_2	100-300	[45]
Mesh of nanowires	Thermal evaporation	L: tens of μm D: 50-100 nm	NO_2	200	[30]
Mesh of nanowires	Thermal evaporation	L: several mm D: tens – hundreds of nm	CO	200 – 400	[46]
Mesh of nanotubes	Sol-gel template	L: few μm D: 200 nm	C_2H_5OH, NH_3	200	[47]
Mesh of nanorods	Solid state reaction and annealing	L: several μm D: 20 nm	C_2H_5OH	300	[48]
Mesh of nanobelts	Evaporation-condensation	100 nm wide 20 – 40 nm thick	Ozone	400	[25]
Mesh of nanowhiskers	Thermal evaporation	L: tens of μm D: 50 – 200 nm	Ethanol	300	[49]
Mesh of nanowires SnO_2-Pd	Thermal evaporation	L: tens of μm D: 30-200 nm	H_2	RT-300	[50]

Mesh of nanowires SnO_2-La_2O_3	Thermal evaporation; aqueous solution deposition for La_2O_3	L: tens-hundreds of μm D: 50-100 nm	C_2H_5OH, CH_3COCH_3, C_3H_8, CO, H_2	400	[51]
Mesh of nanowires SnO_2-Sb	Thermal evaporation	L: tens of μm D: 40 – 100 nm	Ethanol	300	[52]
Single nanobelt	Thermal evaporation	L: tens of μm 80 – 120 nm wide; 10 – 30 nm thick	NO_2	UV activated	[23]
Single nanowire	Catalytic supported CVD	L: 5-15 μm D: 70-90 nm	0.5 ppm NO_2	50 – 300 by self heated nanowire	[53]
Single nanowire	Evaporation/CVD	L: 7.7 μm D: 70 nm	CO	200 - 340	[54]
Single nanowire	Spray pyrolysis	L: several 100 μm D: 30 – 400 nm	CO, CH_4	200	[55]
Single nanowire		D: 60 nm	CO, O_2	200 – 300	[56]
Single nanowire	CVD	D: 20 – 200 nm	Water vapor	295	[57]
Single nanowire	Thermal evaporation	D: 100 nm	NH_3, CO	60 – 300	[58]
Single nanowire SnO_2-Pd/Ni	Thermal evaporation	D: 60 nm	H_2, CO	350	[22]

*L: Length; D: Diameter

Table 2-2 Recent published work on 1-D SnO_2 nanostructure gas sensors.

With the widely reported literature that shows the feasibility of using both multiple and single 1-D nanostructures like nanobelts, nanotubes, and nanowires as a new form of gas sensors with high sensitivity and stability, the current focus in this research area

is to improve other performance parameters, especially their selectivity towards the target gas of interest. There are four directions currently being studied with the aim to improve the selectivity of the 1-D nanostructures [59]:

(I) Functionalizing the surface of nanostructure with a target-specific receptor species. The functionalized species can chemically gate the conducting channel of the nanostructure when the receptor-target recognition process occurs. This is the favoured strategy being pursued for bio-sensing. For gas sensing, an array of different sensing materials, also known as "electronic nose", functions as the target-specific receptor species. The electronic nose enables the detection of various chemicals via pattern recognition method, which is similar to the human olfactory system in odor detection.

(II) Ramping or modulating the operating temperature of the sensing element. Usually a target analyte has a characteristic optimal or threshold temperature above which the redox reaction occurs on the sensor's surface.

(III) Functionalizing the surface of nanostructure with specific catalyst particles which either promote certain catalytic reactions and/or inhibit competing reactions. A few reported works summarized in Table 2-2 which introduced Pd, Ni, La_2O_3, Sb as catalyst on the SnO_2 1-D nanostructure have shown improvement in terms of selectivity towards the target analyte.

(IV) Configuring the 1-D nanostructures as ultra-miniature field effect transistors (FET). The FET configuration offers the possibility of controlling the sensitivity and selectivity, and potentially even allowing the operating temperature of the 1-D nanostructure sensor to be reduced by varying the gate electrode potential thereby changing the electrostatic field strength in the active channel.

1-D nanostructures are promising materials for gas sensors, but most synthesis techniques reported produce either dispersed or randomly oriented assemblies of these 1-D SnO_2 nanostructures [60]. These disordered 1-D nanostructures are too small to handle during the preparation of sensor devices and the reliability of these sensor devices could also be doubted. These 1-D nanostructures are incompatible with the contemporary devices fabrication process based on thick and thin films. If quasi-1-D nanosystems are to be exploited in massively parallel sensor applications, one needs to consider engineering strategies for producing ordered structures consisting of a large number of individual cells that can be regionally functionalized and individually read [61].

Some strategies have been proposed as possible solutions for creating arrays of 1-D nanostructures, with most of the reported work utilizes template-assisted method. Semiconductor SnO_2 nanowire arrays were fabricated by Zheng et al. [62] using electrochemical deposition and thermal oxidizing methods based on highly ordered nanoporous alumina membrane (AAM). The diameter of SnO_2 nanowires is about 70 nm, which is basically equal to that of pores of the AAM used. Kolmakov et al. [56] reported a new paradigm for producing SnO_2 nanowire sensor arrays with possibly thousands of addressable sensing elements that can each be individualized, either through the manipulation of their material composition or the manner in which they are functionalized. Metallic Sn nanowires are first grown in highly ordered porous anodic alumina (PAO) template by alternating current (ac) electrodeposition in an electrolyte containing 0.05 M $SnCl_2.H_2O$ and later removed from the PAO template. The Sn nanowires are then oxidized by gradual annealing up to 825 K for a few hours in air.

Liu et al. prepared nanoporous SnO_2 plates through anodization of tin plates at 5-14 V with oxalic acid serving as the electrolyte [63]. Wu et al. [64] fabricated arrays of nanoporous tin oxide nanorods by electrodeposition of tin into anodic aluminum oxide (AAO) membranes followed by anodization of tin nanorods to create nanochannels. The nanoporous SnO_2 nanorods were 300-700 nm long and 250 nm in diameter, restricted by the pore dimension of the original AAO membrane, with nanochannels of 15-35 nm in diameter. SnO_2 nanohole arrays have been prepared by Hamaguchi et al. [65] using a liquid phase deposition method. Anodic alumina disks were used as the starting material. The outside diameter and inside diameter of the tubes were about 250 and 200 nm, respectively. The SnO_2 tubes consisted of many grains with almost 20 nm diameters. SnO_2 nanohole array sensors equipped with noble metal (Pt, Pd, and Au) electrodes exhibited reversible response to H_2 gas in air. Among the electrode materials used, the largest response was achieved with Pd and the maximum value of sensitivity was 187 at 623 K.

The integration of individual or arrays of 1-D nanostructures with planar technology still poses a major challenge for the realization of gas sensing devices that can be mass produced at reasonably low cost. To become successful third generation gas sensors, the nano-sized SnO_2 materials, in particular the 1-D nanostructures, will have to be prepared in a manner that posseses the characteristics of simplicity, versatility and good compatibility with existing microelectronics-based technology.

2.3 Plasma-enhanced chemical vapor deposition

In the microelectronics industry where conformal film is a requirement, various chemical vapor deposition techniques have been used routinely for the deposition of

conductor, dielectric, and semiconductor films. The plasma-enhanced chemical vapor deposition (PECVD) is a combination of physical and chemical process with the aim to meet the demand for chemical reaction at a lower substrate temperature. It is an established commercial technique introduced in the early 1970s for low-temperature deposition of a number of important materials, especially insulating films such as silicon nitride and silicon oxide [66].

In PECVD, the electrical power is coupled into the reactant gases via the kinetic energy of free electrons. These electrons gain energy rapidly from the electric field and subsequently the inelastic collisions between high-energy electrons and reactant gas molecules will lead to the formation of highly reactive species, such as excited neutrals and free radicals, as well as ions and additional electrons. By this mechanism, the electrons generate the reactive species without substantially increasing the gas temperature. Such species will have lower energy barriers to physical and chemical reactions than their parent species, thus enabling the reaction to occur at lower temperature. This has made the film deposition possible at temperatures lower than that in conventional CVD, which is thermally activated.

2.3.1 Deposition mechanisms

In general, the deposition mechanisms for PECVD can be qualitatively divided into four distinct stages, as shown in figure 2-4. Stage one includes the primary initial electron-impact reactions between the free electrons and reactant gases to form ions and radical reactive species. The typical initial electron-impact reactions are summarized in table 2-3. Stage two is the transportation of excited molecules, atoms,

radicals, molecular or atomic ions from the plasma to the substrate surface through diffusion, concurrently with the occurrence of many elastic and inelastic collisions in both the plasma and sheath regions. Stage three is the adsorption of reactive species on to the substrate surface sites, often after some migration on the surface, which is then followed by surface chemical reaction between the reactive species. Dissociation of molecules during adsorption may also occur. Finally in stage four, the reactive species and reaction products incorporate into the deposited films or re-emit from surface back to the gas phase. In PECVD, ion bombardment and various heterogeneous reactions between ions and radicals with the substrate surface play a significant role in determining the film properties, such as conformality, density, stress and "impurity" incorporation.

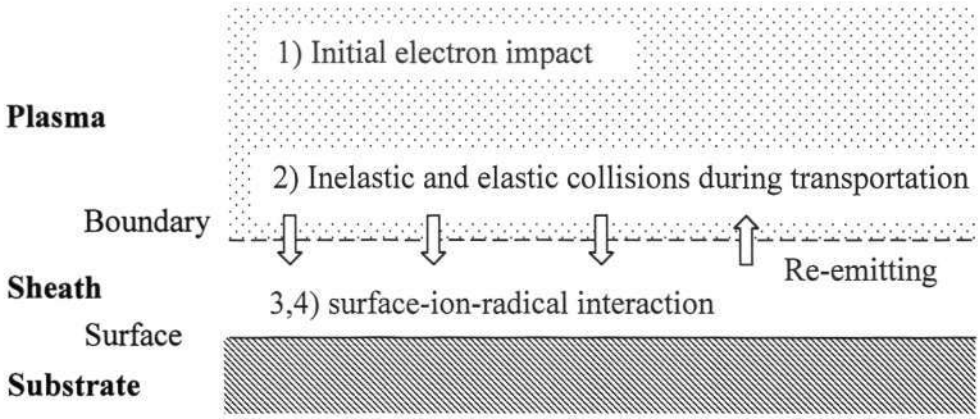

Figure 2-4 The four steps in PECVD deposition mechanisms.

Excitation	$A + e^- \longrightarrow$	$A^* + e^-$
Ionization	$A + e^- \longrightarrow$	$A^+ + 2e^-$
Dissociation	$A_2 + e^- \longrightarrow$	$2A + e^-$
Electron attachment	$A + e^- \longrightarrow$	A^-
Dissociative attachment	$A_2 + e^- \longrightarrow$	$A^- + A$
Charge transfer	$A^+ + B \longrightarrow$	$A + B^+$

Table 2-3 Initial electron-impact reactions. A, A_2 and B refer to reactants, e^- is an electron, A* is reactant A in an excited state, and A^+, A^- and B^+ are ions of A and B.

When the flow rate of reaction gas per unit electric power used to sustain the plasma is relatively small, the deposition rate of the film will be limited by the effective flow rate of the reaction gas. For the case of high reaction gas flow rate, the deposition rate is limited by the externally supplied electric power. Deposition rate also varies with substrate temperature, but the activation energy of the deposition rate is often very small.

2.3.2 Inductively coupled plasma (ICP) sources

Inductively coupled plasma (ICP) sources are known for more than one hundred years [67]. In the past, they had been used at high gas pressures to make plasma torches that heat up gases for spectral analysis besides the application in lighting area [68]. More recently, low pressure ICPs with non-equilibrium plasmas are attracting researchers' interest in microelectronics integrated circuits processing [69]. The ICP source has indeed become one of the dominant high-density plasma sources for the etching processes of semiconductor films [70]. High-density typically means the electron density is above 10^{11} cm^{-3}, with an ion-to-neutral ratio in the range of a few percent and the plasma potential can be made very low, around 10 V. The high-density plasma can offer high process rates due to higher electron density that enables the efficient generation of chemically reactive species. The high ion-to-neutral ratio allows the control of film microstructure and mechanical properties via ion bombardment on the substrate surface. It will also help to enhance the anisotropy of the processing because the plasma ions can be directed to the substrate surface that is potentially biased.

The ICP is the simplest type of high-density source because it does not require an applied magnetic field as in electron cyclotron resonance (ECR) and helicon sources.

Figure 2-5 shows the most common ICP geometries. The coil configuration can be cylindrical, planar or reentrant. The cylindrical coil is the oldest and simplest type of configuration. The planar coil is a recent development for semiconductor etching with close coupling between the wafer and the coil [69]. The reentrant coil is less common but is useful in plasma immersion ion implantation devices [69]. An external circuit is normally used to generate a resonance condition at the driving frequency and cause large current to flow through the radio frequency (RF) coils. These currents generate RF magnetic flux that penetrates through the discharge volume. The time-varying magnetic flux induces a solenoidal RF electric field that accelerates free electrons in the discharge and sustains the plasma. In an ICP source, capacitive coupling is present between the RF coil and the plasma. However, this capacitive coupling is small compared to that of a diode source, because the coils are separated from the plasma by the thick dielectric wall, normally with thickness of more than 1 cm. The presence of capacitive coupling may be needed to initiate breakdown in the plasma [71]. Plasma and process uniformity in ICP sources are controlled by the location of the RF coils, the gas feed and the overall source geometry.

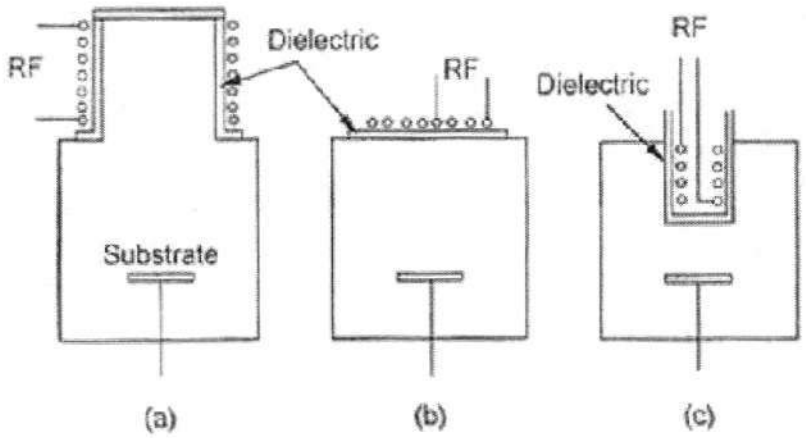

Figure 2-5 ICP sources in (a) cylindrical, (b) planar, and (c) reentrant configurations [69].

CHAPTER THREE

EXPERIMENTAL PROCEDURES

3.1 ICP-CVD system overview

The custom designed ICP-CVD system is comprised of four major modules in terms of functionality. They include the reactive source delivery, deposition chamber and pressure control, plasma generation, and software integration modules. A front view of the ICP-CVD system is shown in figure 3-1. To better illustrate these functional modules, a block diagram of the system is shown in figure 3-2.

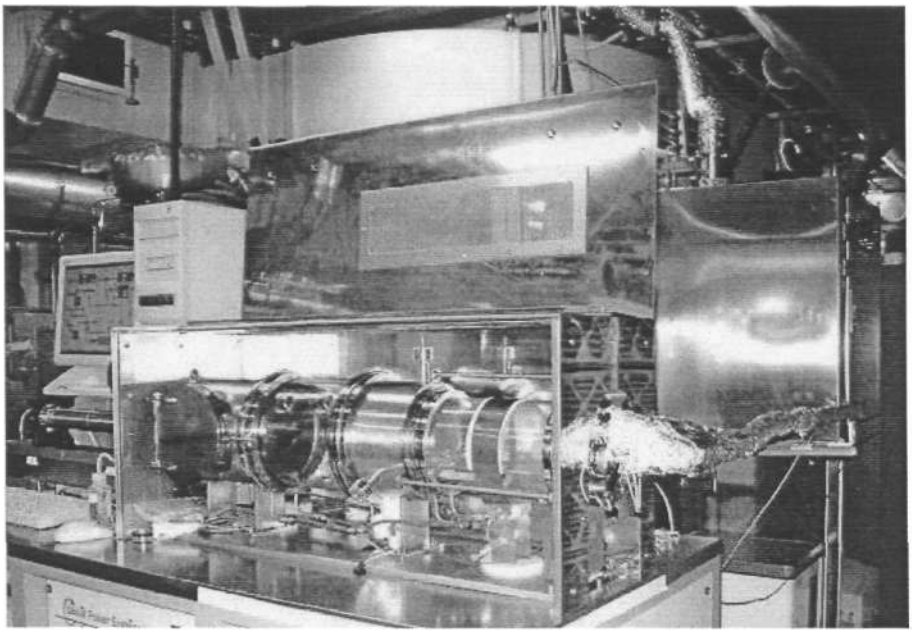

Figure 3-1 Front view of ICP-CVD system.

3.1.1 Reactive source delivery

The reactive source delivery is comprised of a bubbler module and a direct liquid injection module, together with their respective gas handling manifold that acts to regulate and direct the flow of reactants into the deposition chamber.

3.1.1.1 Bubbler delivery module

The bubbler is custom fabricated from stainless steel 304 material with a capacity of 0.5 liter. The sealing of the bubbler is achieved using Teflon encapsulated Viton o-ring that sits onto the machined groove at the top portion of the bubbler. A carrier gas is passed through the bottom of the liquid reactant via the dip tube or inlet line that bubbles out of the liquid and carries the reactant vapor through the outlet line. The internal surface of the bubbler is electro-polished for passivation purpose.

The precursor vapor pressure is an important factor that determines its mass flow rate. The strong dependence of vapor pressure on temperature has made temperature control indispensable to ensure accurate vapor delivery. For the ICP-CVD system, the liquid precursor temperature can be precisely controlled in the range of 50-110 °C using a Schumacher Temperature Control System. The Schumacher system is made up of the temperature control unit (TCU) and the source temperature controller (STC). The bubbler is placed inside the STC, which is equipped with a heater and a temperature sensing probe. The temperature setting operation is performed using the TCU unit which furnishes corresponding voltage pulses at different rates to the heater, thereby maintains the temperature of the liquid within ±0.3 °C of the set temperature.

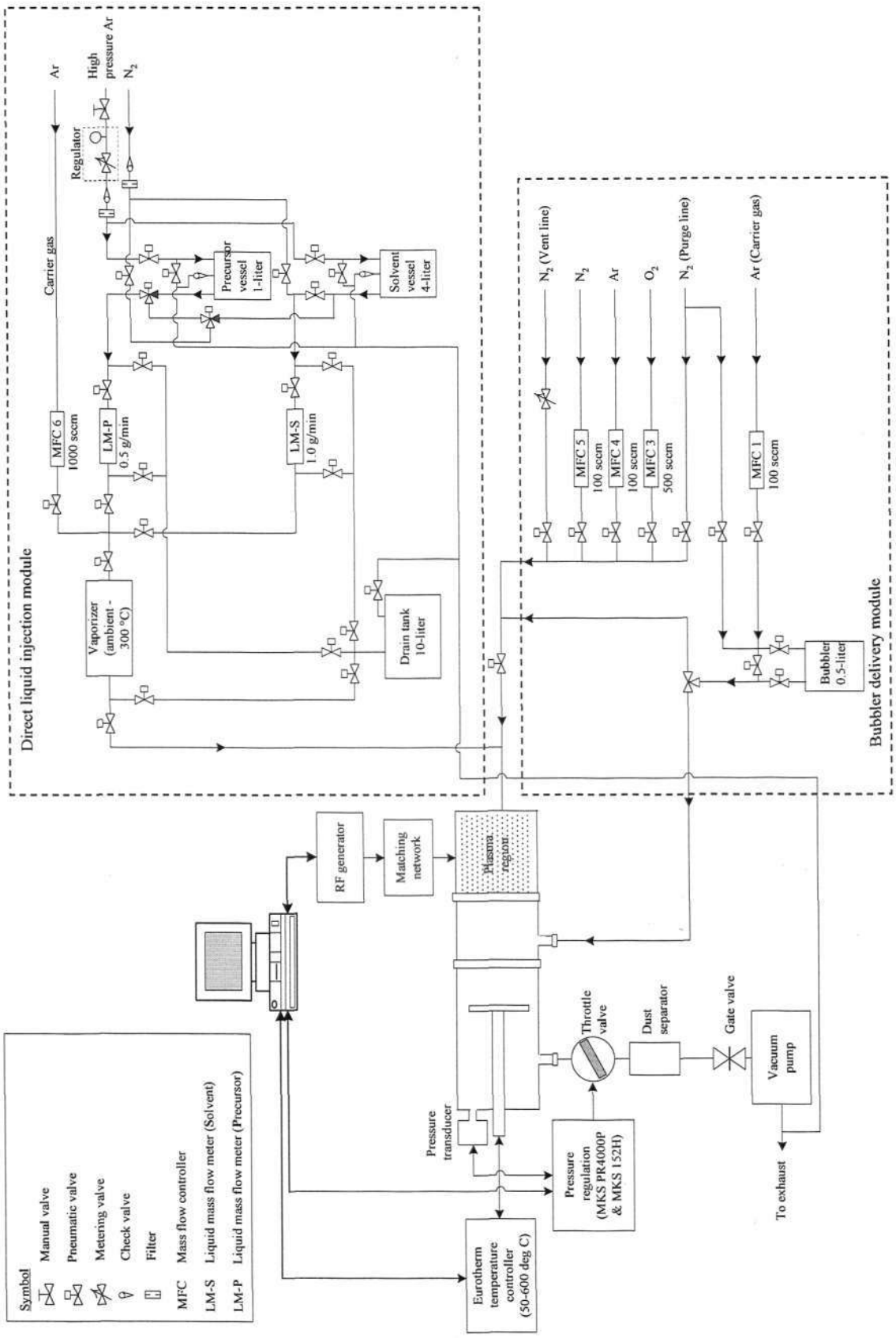

Figure 3-2 Block diagram of the ICP-CVD system.

The gas handling manifold comprises of pneumatic valves, solenoid valves, metering valve, ball valve, mass flow controllers, and ¼" stainless steel tubing that serve to regulate and direct the flows of gases and reactants. Precise control of flow rate into the deposition chamber is achieved using the MKS mass flow controllers (MFCs). These MFCs are electronically controlled via a MKS 647B 8-channel flow programmer. A normally-closed (N-C) pneumatic valve is installed at each gas line tubing to provide a firm shutoff that serves to isolate the gas supply from entering the chamber for the gas that is not in use.

3.1.1.2 Direct liquid injection (DLI) module

The ICP-CVD system is equipped with a Lintec low pressure liquid vaporization and supply system for its DLI module. The Lintec system is composed of two liquid mass flow meters and a vaporizer unit that also serves as a flow rate controller. The DLI module differs from the bubbler delivery method where the liquid precursor is dissolved in a suitable solvent and directly metered into a vaporizer, which the resulting vapor is then transported into chamber with or without a carrier gas.

The Lintec DLI features two separate delivery lines, denoted as the precursor and solvent lines that lead to the vaporizer section. The solvent line allows on-line cleaning of the vaporizer without the need to dismantle and change the liquid in the vessel. Pressurized argon gas is used as the push gas that delivers the liquid to the vaporizer passing through the mass flow meter. The liquid introduced to the vaporizer is flow rate controlled by a control valve equipped with a shutoff function. The liquid is mixed instantaneously with the argon carrier gas after passing through the control valve, which is subsequently fed through a nozzle and vaporized in a vaporization chamber

built with embedded heaters. The vaporizer can be heated up to 300 °C due to its all metal structure and finally the vaporized liquid is transported to the deposition chamber. The liquid handling manifold is made up of pneumatic valves and ¼" stainless steel tubing. A 10 liter drain tank is provided to collect the precursor residues that dissolve into the solvent during cleaning process. The whole Lintec DLI module is housed inside a two tier stainless steel cabinet.

3.1.2 Deposition chamber and pressure control

The ICP-CVD chamber is comprised of three main sections as shown in the schematic diagram in figure 3-3. The first section includes the stainless steel covering end-plate with multi-insertion ports and the 150 mm diameter quartz cylinder wound with copper band for the high-density plasma generation. The second section is the stainless steel adaptor with the alternative precursor entry port. The third section consists of the 200 mm diameter quartz cylinder and the stainless steel housing that contains the substrate holder mounted on a horizontal manipulator, a process door for sample loading and unloading, together with a mounting port for pressure transducer.

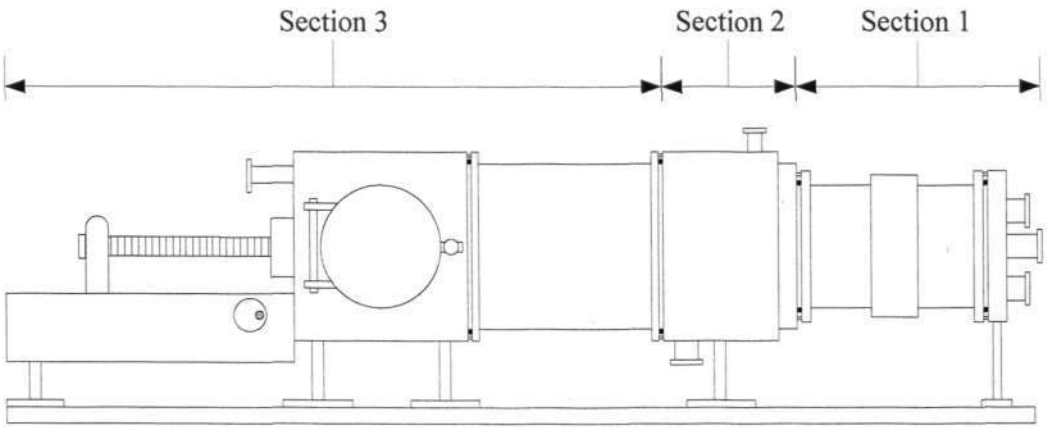

Figure 3-3 The three sections of ICP-CVD deposition chamber.

The substrate holder is equipped with heating function to provide annealing effect to the substrate during deposition. The heating coil with type-K thermocouple is in direct contact with the backing plate and the temperature range can be controlled between 50 to 600 °C using a Eurotherm 2416 PID controller. There are two MKS Baraton pressure transducers mounted in the stainless steel housing, one in the 1000 Torr range and another in the 1 mTorr range. The chamber pressure control process in the ICP-CVD system forms a closed-loop control where a MKS 152 pressure controller reads the signal from the MKS pressure transducer through a MKS PR4000P pressure read-out unit, compares it to a predefined set point, and places a MKS 253 throttle valve in a position to maintain, or achieve the set point pressure in the chamber.

The vacuum generation module in the ICP-CVD system comprises of a rotary vane pump and a root blower from Alcatel, with pumping speed of 35 m^3/h and 150 m^3/h respectively. The chamber can be evacuated to 10^{-3} Torr within minutes, and the lowest achievable pressure is 16 mTorr. A Pfeiffer vacuum dust separator with particle size limit of 1 μm is installed at the intake line of the vacuum pump to prevent large quantities of particles from getting into the pump. A gate valve is fitted between the dust separator and the vacuum pump inlet to isolate the chamber from the pump during venting. The outlet of the pump is connected to the main exhaust duct for safety and environmental purposes.

3.1.3 Plasma generation

The RF generator operates at 13.56 MHz, which is one of the standard frequencies allocated by the United States Federal Communication Commission for industrial usage. The generator is capable of delivering up to 2 kW of RF power. A matching

network is placed between the RF generator and the glow discharge. This serves to increase the power dissipation in the discharge and minimize the reflected power, thus protects the generator. In order to avoid large RF currents flowing round a circuit, most RF generators are generally designed to have a pure resistive output value of 50 ohms. Similarly the RF generator in the ICP-CVD system has an output impedance of 50 ohms. For ICP-type loads, the reactive part of the impedance is of an inductive nature and therefore a capacitive reactive component is required in the matching network that serves to transform the complex impedance of the plasma load to a pure 50-ohm impedance for maximum power transfer. The matching network of ICP-CVD system can function either in automatic or manual mode whereby the loading and tuning capacitors will be tuned to find a precise impedance match between the plasma load and the RF generator.

3.1.4 Software integration

The various functional modules of the ICP-CVD system are interfaced to a PC with an integrated custom-designed Graphical User Interface (GUI). The integrated software system serves as a platform for the user to operate the ICP-CVD system remotely. The five modules listed in table 3-1 are linked to the Moxa Smartio C168H 8-port serial board in the PC. The hardware components under the control of each module are also depicted in table 3-1. The Borland Delphi 5.0 is used as the software development platform for the GUI application program. The interfacing between each module and the PC is established using the standard RS-232 serial communication protocol.

No	Module	Component
1	Blackstar I/O controller	- Solenoid valves - RF generator
2	MKS Multi-channel flow/pressure controller	- MFCs - Throttle valve
3	Eurotherm PID controller	- Substrate heater
4	ADAM 5000 data acquisition and control system (DLI module)	- Solenoid valves - Thermocouples output
5	Lintec LV-2100 controller (DLI module)	- Liquid MFCs

Table 3-1 The interfaced modules of the ICP-CVD system for computer control.

Besides operating the ICP-CVD system remotely via the user-friendly GUI window, manual control is also made possible through the front panel of system where the control modules are fitted. The MKS mass flow programmer and pressure controller, Eurotherm PID controller, Lintec liquid MFCs, on-off control of the pneumatic valves, and RF generator are all accessible through the front panel of the system. The manual control mode allows the user to perform diagnostic work on the system.

3.2 Structural characterization and chemical analysis

Various characterization tools were utilized to investigate the properties of interest including surface morphology, crystalline structure, grain size, surface elemental and chemical state information of the deposited films. The films deposited using the ICP-CVD system were characterized by field emission scanning electron microscope (FESEM) for surface morphology, transmission electron microscope (TEM) for film microstructure, x-ray diffraction (XRD) for crystallography information and grain size

estimation, and x-ray photoelectron spectroscopy (XPS) for surface elemental, chemical state and semi-quantitative composition determination.

FESEM is a widely adopted technique in thin film and coating characterization work for the investigation of film microstructure and surface topography. The FESEM is capable of producing a plan view that shows the grain size and shape, their uniformity and coverage, presence of hillocks or whiskers, evidence of film voids, and microcracking. In addition to that, FESEM is also used to obtain cross sectional views of multilayer structure that show the interfacial information between the substrate and the film. A Leo 1550 FESEM was used to characterize the microstructure and morphology of the deposited films. It is a field emission type SEM capable of producing brighter and finer electron beam, which enhances the resolution of the SEM compared to the conventional type of SEM. A range of 10-15 keV electron energy beam was used to characterize the films where micrographs up to 100k magnification could be captured.

TEM is an important analysis tool in nanotechnology research as it is capable in imaging and analyzing the microstructure of materials down to atomic scale resolution. The high resolution imaging mode of the TEM images the crystal lattice of a material as interference pattern between the transmitted and diffracted high energy electron beams. This allows one to observe planar and line defects, grain boundaries, interfaces etc at atomic scale. The bright and dark field imaging modes of TEM, combined with electron diffraction are also invaluable in giving information about the morphology, crystal phases and defects in a material. A Jeol JEM-2010 high resolution TEM with accelerating voltage up to 200 kV and a point resolution of ~2 Å was used to study the

microstructure of the films. Selected area diffraction (SAD) was also performed to obtain the crystallographic information of the nanostructured films.

XRD technique is a convenient tool in characterizing crystalline materials. It is non-destructive and simple in terms of sample preparation. XRD analysis was performed using a Rigaku Dmax 2200 x-ray diffractometer. The copper K_α radiation x-ray with a wavelength of 1.5406 Å at 40 kV and 30 mA was used. The sample was tilted 0.5° towards the x-ray beam and fixed throughout the 2θ detector scan from 20 – 60°. The tilt angle was kept small to minimize the penetration of x-ray beam into the substrate. Scherrer's equation is employed to estimate the average grain size, D, along the surface normal direction [72]:

$$D = 0.9\lambda / B\cos\theta \qquad (3\text{-}1)$$

where B is the full width at half maximum (FWHM) of the broadened diffraction line on the 2θ scale (radians) and θ is the diffraction angle.

XPS has been developed into the key surface characterization method over the past few decades which combines surface sensitivity with the ability to quantitatively obtain both elemental and chemical state information. XPS characterization was carried out using a Kratos-Axis spectrometer with monochromatic Al Kα (1486.71 eV) X-ray radiation (15 kV and 10 mA) and a hemispherical electron energy analyzer. The base vacuum of the chamber was 2×10^{-9} Torr. Survey spectra in the range of 0-1100 eV were recorded in 1 eV steps for each sample, followed by high-resolution spectra over different elemental peaks in 0.1 eV steps, whereby the detailed composition was calculated. Curve fitting was performed after a Shirley background by nonlinear least square fitting using a mixed Gauss/Lorentz function. To remove the surface

contamination layer, Ar ion bombardment was carried out for 600 seconds using a differentially pumped ion gun (Kratos MacroBeam) with an accelerating voltage of 4 keV and a gas pressure of 1×10^{-7} Torr. The bombardment was performed at an angle of incidence of 45 ° with respect to the surface normal.

3.3 Gas sensing characterization

The direct current (dc) conductance measurement aims to investigate gas sensing properties of the sensing materials whereby the presence of a reducing gas such as CO or H_2 will cause an increase in the conductance of the sensing materials. The gas sensing properties based on the dc electrical measurement were characterized using a home-designed gas sensing experimental system, as shown in figure 3-4. The measurement was performed in an enclosed gas chamber with a volume of 640 cm^3. A Keithley 236 source measure unit was used for the direct current-voltage measurement. Sample heating was performed using a Linkam heater stage with a heating rate of 1-5 °C/min. The ambient conditions inside the gas chamber were set by flowing desired test gas in background diluting gas of either air or nitrogen. The humidity level of the ambient can be set by directing a portion of the diluting gas through the bubbler filled with water. The flow rate and concentration of test gas were controlled using four MKS MFCs. Figure 3-5 shows a pictorial view of the gas sensor characterization system.

Au interdigital top electrodes with 1 mm spacing in between the fingers were deposited on the sensing materials for electrical measurement by electron beam evaporation using shadow mask. The device was attached to an alumina substrate with two gold pads. A gas sensor device was made by connecting the interdigital gold

electrode on the sensing material to the respective gold pads on the alumina using gold wire bonding. Before testing, air sweep from room temperature to 450 °C with heating rate of 1 °C/min was carried out to age the device. In this process, only dry air was introduced to the chamber. After the resistance of the device was stabilized, the device was cooled down to room temperature at 1 °C/min. Then, the device was heated to 450 °C step by step with the heating rate of 1 °C/min. At each step of 150 °C, 200 °C, 250 °C, 300 °C, 350 °C, 400 °C and 450 °C, test gas was introduced into the chamber with dry air while maintaining the total combined flow rate of 500 sccm. The test gases used include CO, H_2, C_2H_5OH, and NH_3. The gas sensitivity S is given by the relative resistance, $S = R_{air}/R_{gas}$, where R_{air} and R_{gas} are the resistance of the sensor in air and in detecting gas respectively.

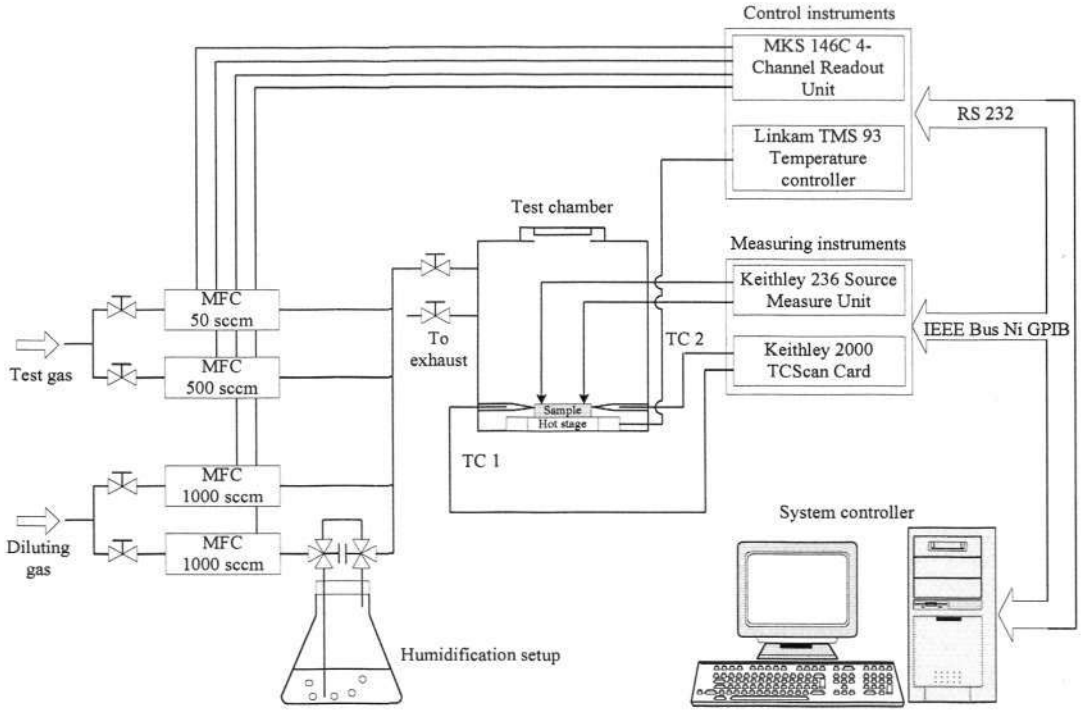

Figure 3-4 Block diagram of the gas sensor characterization system.

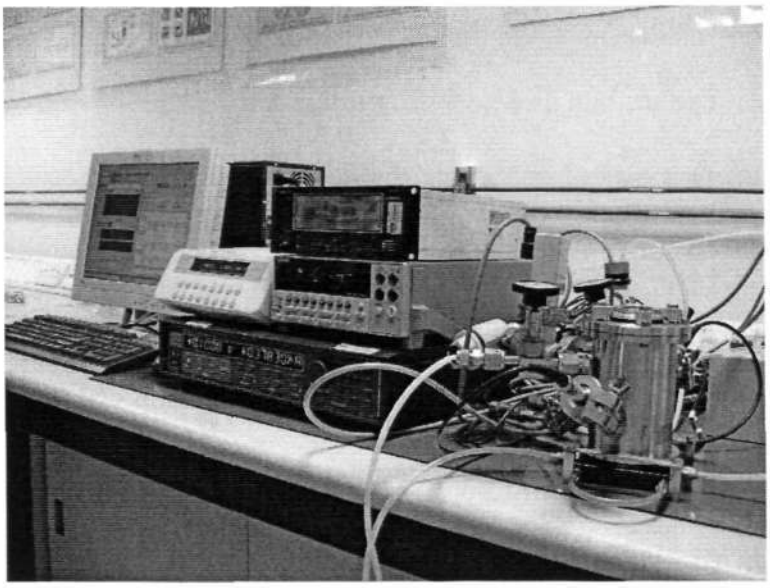

Figure 3-5 Pictorial view of the gas sensor characterization system.

CHAPTER FOUR

NANOCRYSTALLINE SnO_2 THIN FILMS

4.1 Introduction

The gas sensing mechanism of SnO_2 gas sensors is largely based on the surface reactions and hence, nanostructured SnO_2 thin films are of great interests due to the large surface-to-volume ratio and the small grain size which is comparable to the depth of the surface space charge layer. Nanostructured SnO_2 films have been successfully prepared using many thin films technologies, such as thermal evaporation [73], spray pyrolysis [74], atomic layer deposition (ALD)[75], magnetron sputtering [76], PECVD [77,78], and metal-organic CVD [79]. The results reported in the literature have clearly demonstrated that the microstructures and surface morphologies of the films are strongly dependent on the deposition method and the processing conditions during the film preparation, which in turn determine the properties, performance and reliability of the SnO_2 sensing films. Therefore, a systematic investigation on how the preparation parameters will affect the microstructure of SnO_2 thin films is necessary to understand the microstructure-property relationships of sensing materials based on SnO_2 thin films. In this chapter, we first study the effect of processing parameters on the microstructures and crystal phase of the SnO_2 thin films prepared using the custom-designed ICP-CVD system with bubbler delivery method. The microstructures

and surface morphologies of the films are investigated by XRD, FE-SEM, and TEM. Next, the gas sensing properties of the fabricated sensors device are characterized for the detection of CO and H_2.

4.2 Nanocrystalline SnO_2 thin films deposited by ICP-CVD with bubbler delivery method

4.2.1 Experimental details

In this section, the SnO_2 thin films deposited by ICP-CVD system using bubbler delivery method will be presented. Dibutyltin diacetate (Aldrich, 98% purity), $(C_4H_9)_2Sn(OOCCH_3)_2$, was used as the tin precursor. The precursor was soaked at 90 °C. Ar was used as the carrier gas at a flow rate of 100 sccm together with 100 sccm O_2 as the reaction gas. A 4″ SiO_2/Si wafer was used as the substrate and it was placed inside the ICP zone for deposition. There was no additional substrate heating during deposition or post annealing of the films. The effects of various process parameters, namely the substrate position, RF power, gas flow ratio of O_2/Ar on the thin film microstructures were investigated.

4.2.2 Effect of substrate-nozzle distance (D_{sn})

It should be indicated that the substrate was exactly located in the middle of the plasma at a substrate-nozzle distance D_{sn} of 12.5 cm and the substrate position shifted to the downstream of the plasma for D_{sn} larger than 12.5 cm. Figure 4-1 shows the XRD patterns of the SnO_2 thin films deposited at various D_{sn}. The as-deposited SnO_2 thin films were well crystallized even without substrate heating. Liu et al. [77] reported that crystallization of the SnO_2 thin films prepared using their home-made apparatus of PECVD was achieved at a substrate temperature of 350 °C. While

Hellegouarc'h et al. [80] reported that SnO_2 thin films prepared by PECVD with a substrate temperature of below 80 ° was amorphous and required post annealing at 600 °C to stabilize the films. In contrast, well crystallized SnO_2 thin films were obtained using the ICP-CVD method without any additional substrate heating or post annealing. All the diffraction peaks could be indexed as those for Cassiterite SnO_2 (PDF 41-1445). A shift of the preferred orientation from (101) plane to (110) plane was noted with the increase of D_{sn} from 12.5 cm to 24.5 cm. The (101) orientation is a stable low energy face for SnO_2 and exists mainly in nature [81,82] while the (110) orientation is the lowest energy surface for SnO_2 with surface-tin atoms in their bulk Sn^{4+} oxidation state [43]. Figure 4-2 shows the effects of D_{sn} on the film thickness and the mean grain size as calculated by Scherrer's equation. With the increase of D_{sn} from 12.5 cm to 24.5 cm, there were lesser reactants reaching the substrate due to insufficient energy of the reactants and the loss via deposition on the chamber side wall. The slower growth rate of the substrate placed at larger D_{sn} was evidenced by the decrease in grain size from 17.5 nm (D_{sn} = 12.5 cm) to 5.3 nm (D_{sn} = 24.5 cm), as well as a dramatic decrease in the thickness of the films from 144 nm down to 20 nm correspondingly. This result has been published in [83].

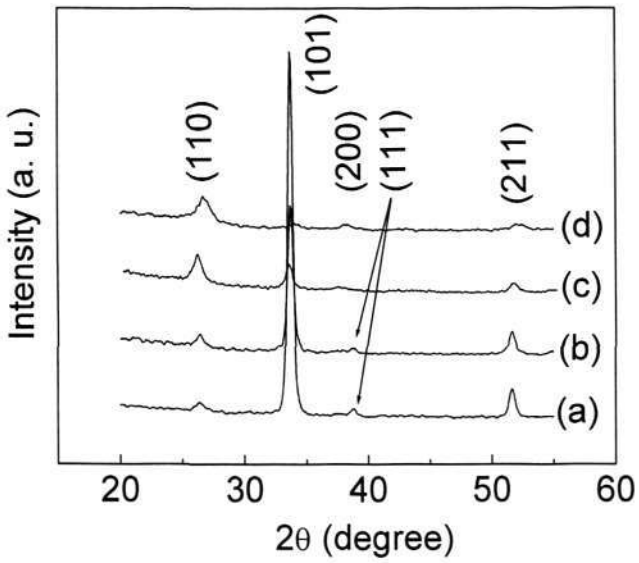

Figure 4-1 XRD patterns of the SnO_2 thin films deposited at D_{sn} = (a) 12.5 cm, (b) 16.5 cm, (c) 20.5 cm, and (d) 24.5 cm [83] .

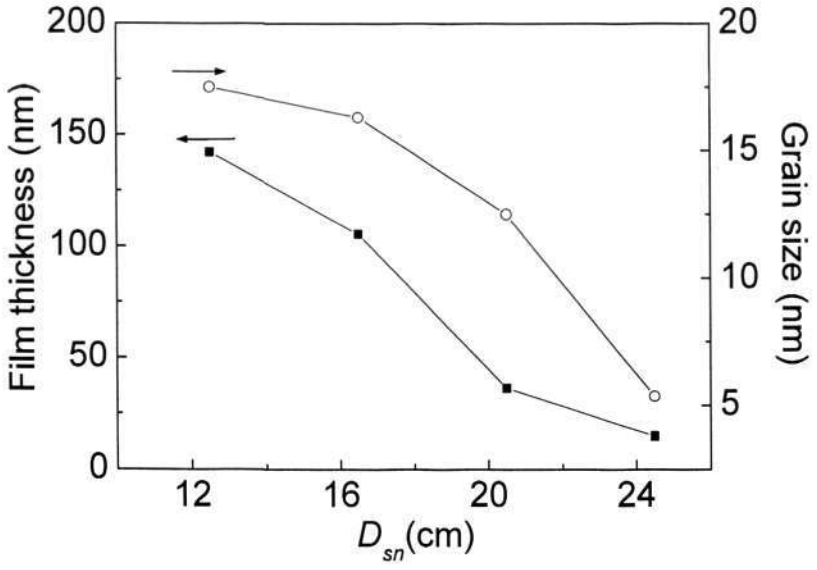

Figure 4-2 Effects of D_{sn} on the thickness and grain size of the SnO_2 thin films [83].

Figure 4-3 shows the SEM micrographs of the SnO_2 thin films deposited at D_{sn} = (a) 12.5 cm, (b) 16.5 cm, and (c) 20.5 cm. The SnO_2 thin film deposited in the middle of the plasma (D_{sn} = 12.5 cm) was rough with irregular shape grains interconnected among each other (figure 4-3(a)). This rough microstructure was possibly formed as a result of the strong plasma sputtering effect that co-existed with the film deposition process at D_{sn} = 12.5 cm. The grains in the SnO_2 thin film deposited at 16.5 cm was regular in uniform size of 40 nm, and some tetragonal grains could be observed (figure 4-3(b)), which indicated that the films were well crystallized and developed. Some large particles were observed on the SnO_2 thin film deposited at 20.5 cm (figure 4-3(c)). The SEM micrographs confirmed that the grain size of the films decreased with the increase of D_{sn}.

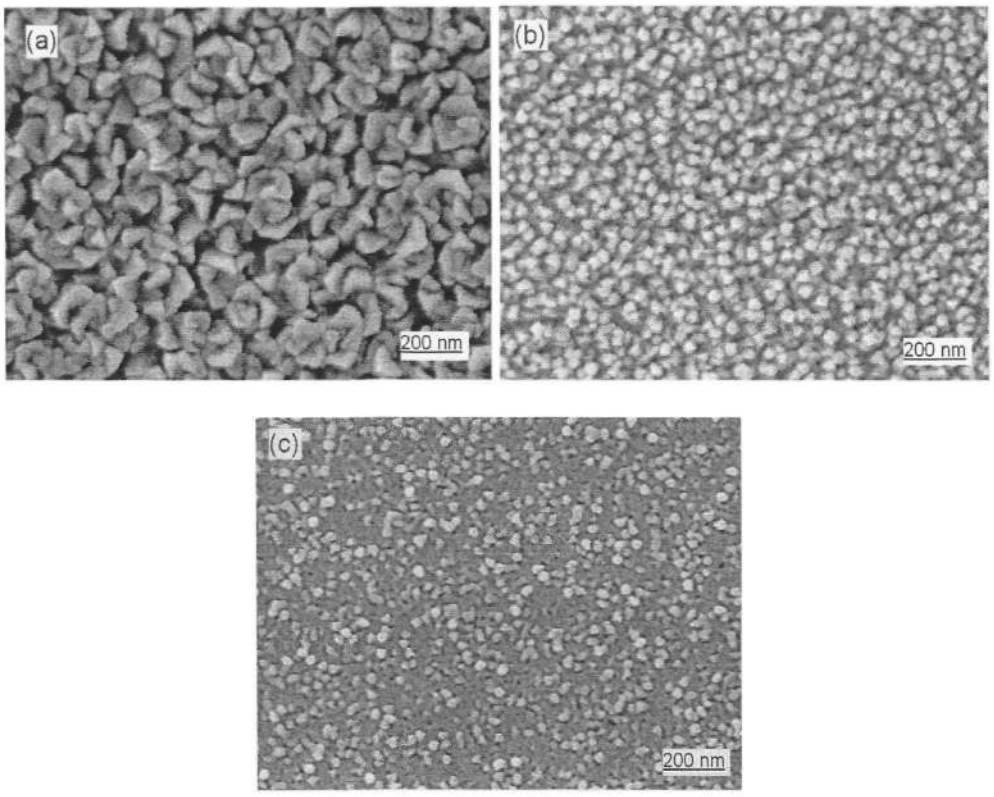

Figure 4-3 SEM micrographs of the SnO_2 thin films deposited at D_{sn} = (a) 12.5 cm, (b) 16.5 cm, and (c) 20.5 cm [83].

4.2.3 Effect of RF power

Figure 4-4 shows the XRD patterns of the SnO_2 thin films deposited at D_{sn} = 20.5 cm with RF power of (a) 400 W, (b) 800 W, (c) 1200 W, and (d) 1500 W. Similar shift of the preferred orientation from (101) plane to (110) plane as shown in figure 4-1 was also observed with the increase of RF power from 400 W to 1500 W. Figure 4-5 shows the effects of RF power on the thickness and grain size of the SnO_2 thin films. It showed that the grain size as well as the films thickness decreased with the increasing RF power. Higher RF power increases both electron density and energy, accelerating reactions of precursor in the plasma phase, which are both prerequisites for the formation of SnO_2 and SnO [84]. Thus, the concentration of the SnO_2 components was higher in the plasma, and resulted in a higher nuclei rate of SnO_2 in the plasma. A higher nuclei rate consumed more of the precursor in a shorter time and resulted in a smaller grain size. However, as the clusters in the plasma were more active at higher RF power, they were likely to deposit on the chamber wall and caused precursor loss. As a result, the films deposited were thinner.

Figure 4-6 shows the SEM micrographs of the SnO_2 thin films deposited at D_{sn} = 20.5 cm with RF power of (a) 400 W, (b) 800 W, (c) 1200 W, and (d) 1500 W. The SnO_2 thin films deposited at 400 W were very smooth and dense. As the RF power increased, small micro-particles were observed. The SnO_2 thin films deposited at higher RF power showed rough surface morphologies except for film deposited at 1500 W. Among the different RF power settings, the SnO_2 film deposited at 1500 W was thinnest at ~40 nm (figure 4-5). The rough morphology was beginning to evolve at such thickness with scattered SnO_2 clusters observed across the film. The grain size of

the SnO_2 thin films seemed to decrease with the increase of RF power, which was in accordance with the results obtained by Scherrer's equation (figure 4-5).

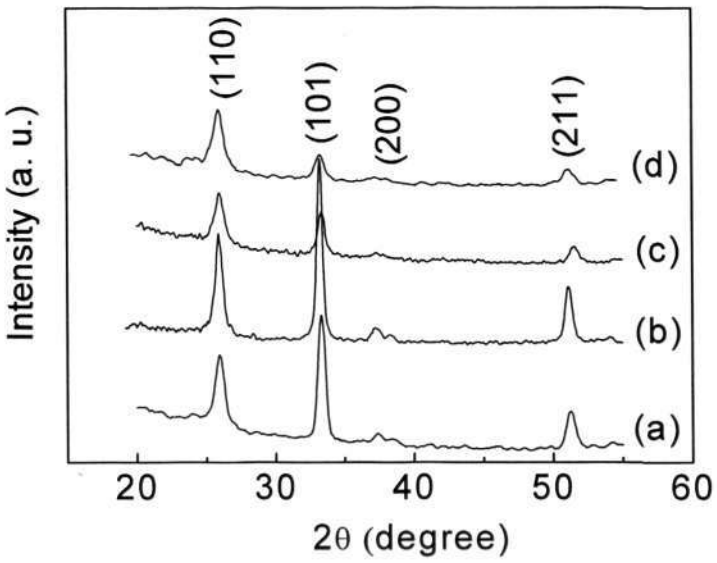

Figure 4-4 XRD patterns of the SnO_2 thin films deposited at D_{sn} = 20.5 cm with RF power of (a) 400 W, (b) 800 W (c) 1200 W, and (d) 1500 W [83].

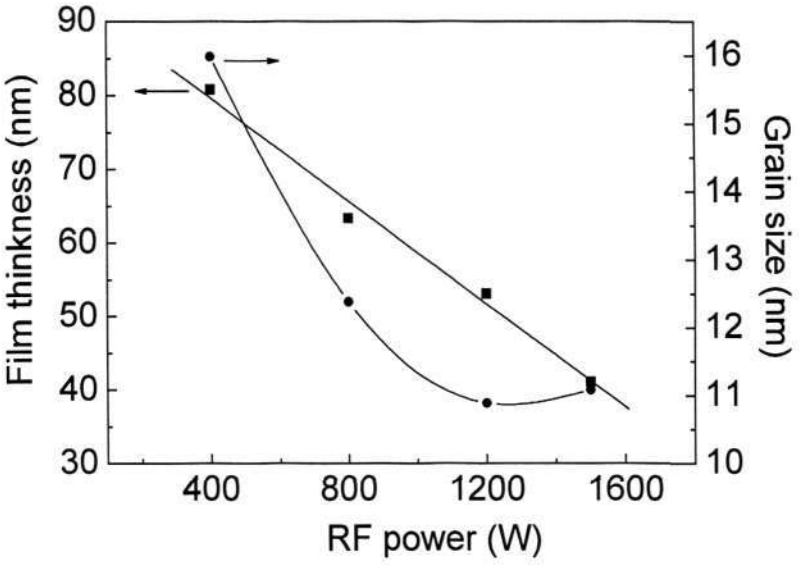

Figure 4-5 Effects of RF power on the thickness and grain size of the SnO_2 thin films [83].

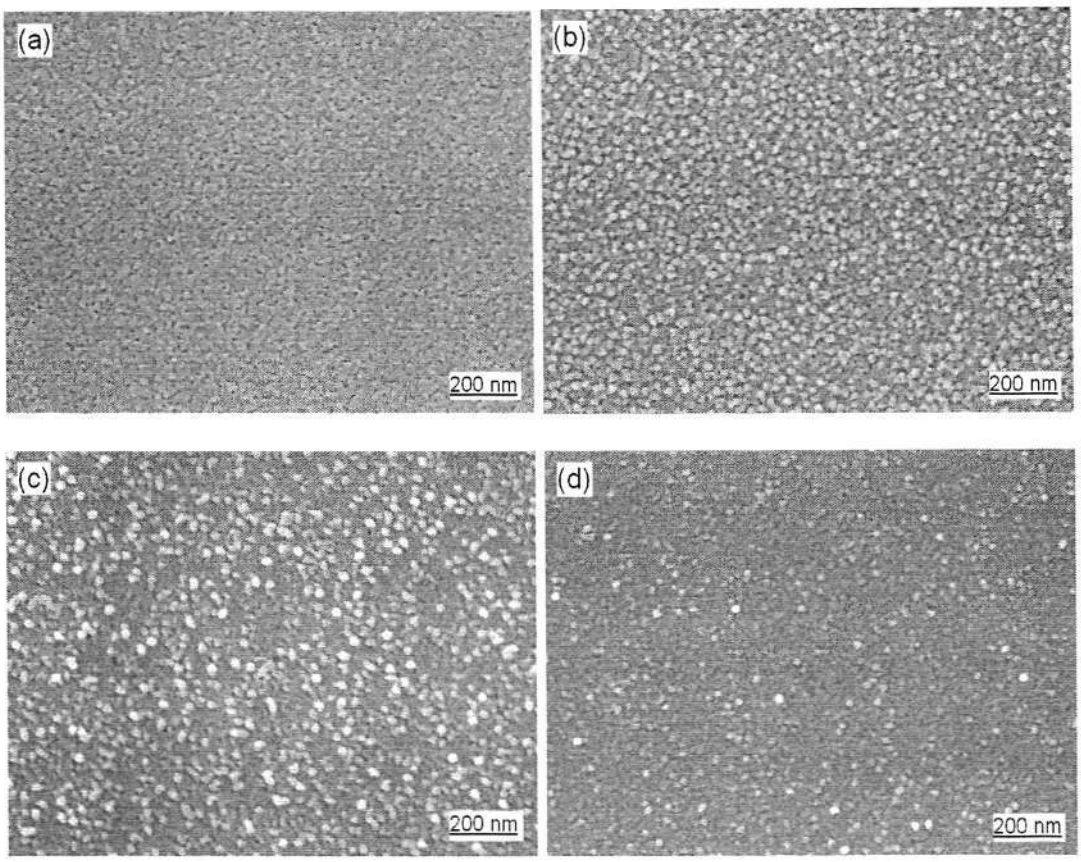

Figure 4-6 SEM micrographs of the SnO_2 thin films deposited at D_{sn} = 20.5 cm with RF power of (a) 400 W, (b) 800 W, (c) 1200 W, and (d) 1500 W [83].

4.2.4 Effect of gas flow ratio of O_2/Ar

Figure 4-7 shows the XRD patterns of the SnO_2 films deposited at 20.5 cm with the O_2/Ar ratio of (a) 2, (b) 1, (c) 1:2 and (d) 1:3. All the films were Cassiterite SnO_2, but some SnO phase was found in the SnO_2 thin film deposited at low O_2 flow rate. Figure 4-8 shows the thickness and grain size as function of the ratio of O_2/Ar. Both the SnO_2 grain size and thickness of the thin films increased with the increase of oxygen ratio initially. The deposition rate and the grain size reach its maximum at O_2/Ar = 1, then they decreased with further increase of the O_2 flow rate. It was noted that sufficient oxidation atmosphere was needed for the formation of SnO_2 phase and the growth of films and grains. Figure 4-9 shows the SEM micrographs of the SnO_2 thin films

deposited at 20.5 cm with O_2/Ar ratio of (a) 2, (b) 1, (c) 1:2 and (d) 1:3. It showed that the O_2/Ar ratio had no notable effect on the morphologies of the SnO_2 thin films.

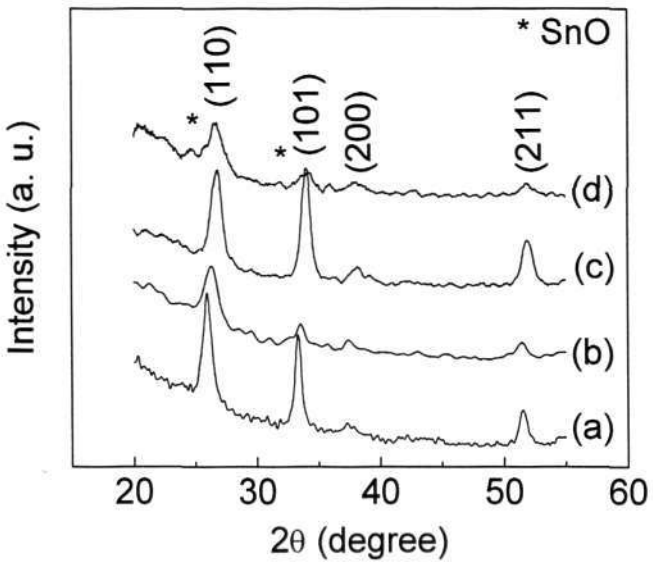

Figure 4-7 XRD patterns of the SnO_2 films deposited at 20.5 cm with O_2/Ar ratio of (a) 2, (b) 1, (c) 1:2 and (d) 1:3.

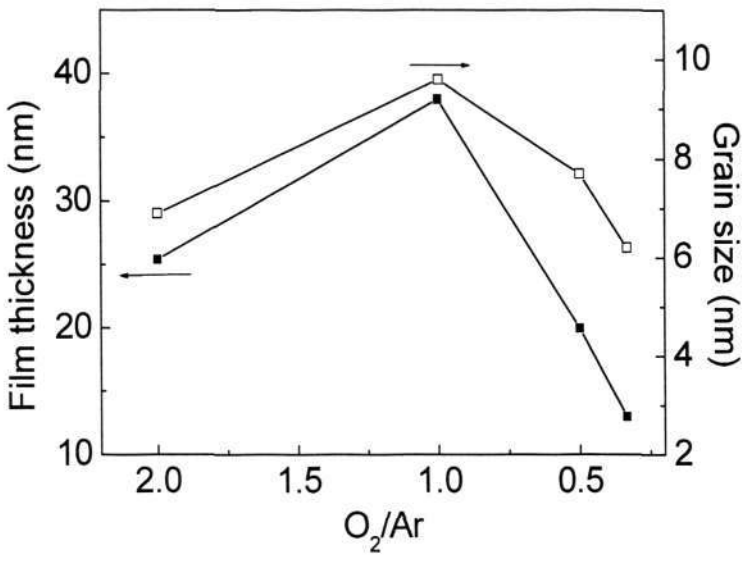

Figure 4-8 Film thickness and grain size as a function of the ratio of O_2/Ar.

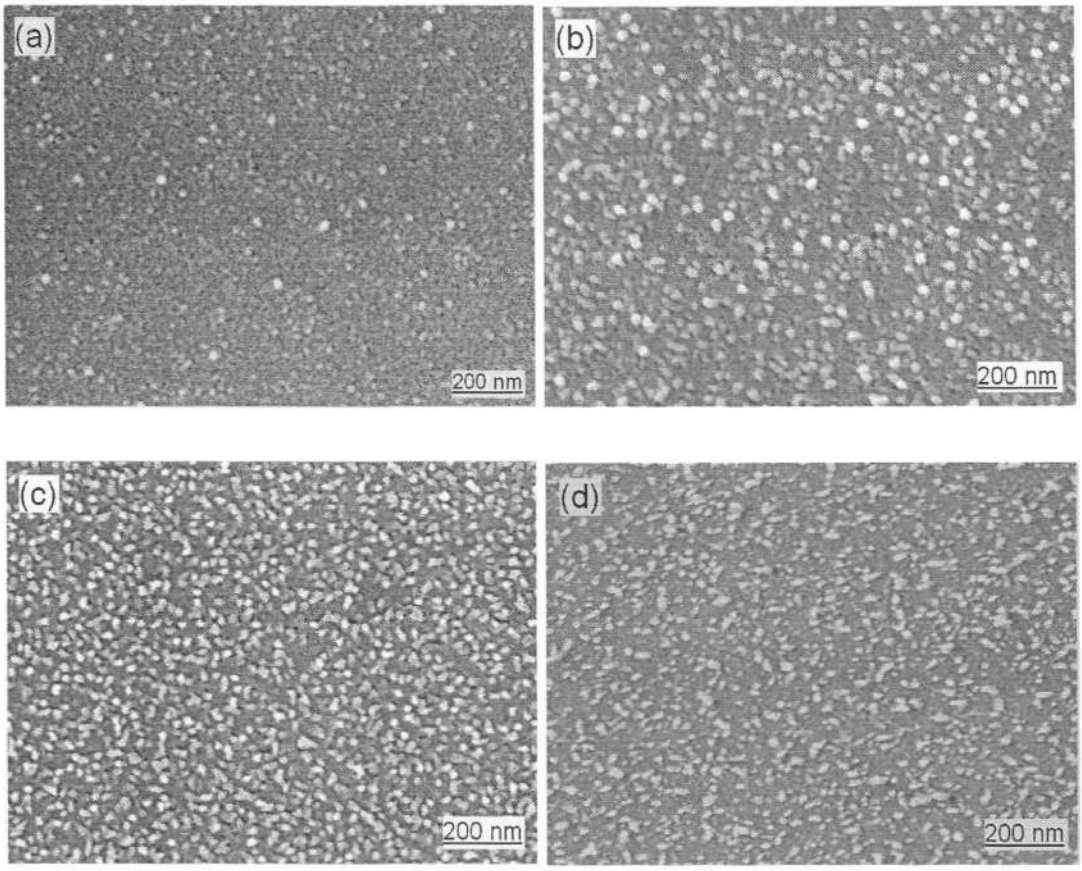

Figure 4-9 SEM micrographs of the SnO_2 films deposited at 20.5cm with O_2/Ar ratio of (a) 2, (b) 1, (c) 1:2 and (d) 1:3.

4.3 Gas sensing properties of nanocrytalline SnO_2 thin films

The gas sensing properties of the nanocrystalline SnO_2 thin films deposited at different D_{sn} were characterized using the gas sensing characterization system described in chapter 3. The test gases were CO and H_2 with a concentration of 1000 ppm in air. Figure 4-10 shows the gas sensitivity (R_{air}/R_{gas}) of the SnO_2 thin films deposited at various D_{sn} to CO and H_2 versus the sensor operating temperature. SnO_2 thin films deposited at D_{sn} = 16.5 cm and 20.5 cm showed the highest sensitivity to CO and H_2 respectively. The highest sensitivity to CO was 16 at 250 °C whereas to H_2 was 44 at 400 °C. The SnO_2 thin films deposited at D_{sn} = 24.5 cm showed the lowest sensitivity

to both CO and H_2. The gas sensing characteristics of the SnO_2 thin films deposited at various D_{sn} were seemingly influenced by the microstructures of the films.

From the grain size point of view, the SnO_2 thin film deposited at D_{sn} = 24.5 cm should exhibit the best sensing performance with its smallest grain size of 5.3 nm, which is close to twice the Debye length of SnO_2 (6 nm). Such a grain size leads to the achievement of maximum sensor response through the formation of a space-charge region in the whole crystallite as reported by Yamazoe and co workers [14,15]. However, it depicted the poorest sensitivity among the SnO_2 thin films deposited at different D_{sn}. One possible explanation for such observation could be attributed to the role of crystallographic structure of metal oxides on gas sensing besides the dimensional factors like grain size and film thickness. According to Korotcenkov [85], the external planes of nano-crystals participate in gas-solid interaction, and therefore these very planes determine the gas-sensing properties of nanostructured materials. Every crystallographic plane has its own combination of surface electron parameters, which include surface state density, energetic position of the levels, activation energy of native point defects and so on. This implies that the chemisorption characteristics change noticeably from one crystal surface orientation to another. With an increase of D_{sn} from 12.5 cm to 24.5 cm, the preferred growth orientation of SnO_2 thin films was found to shift from (101) to (110), and this has caused corresponding changes in atomic and electronic properties along with surface energy parameters.

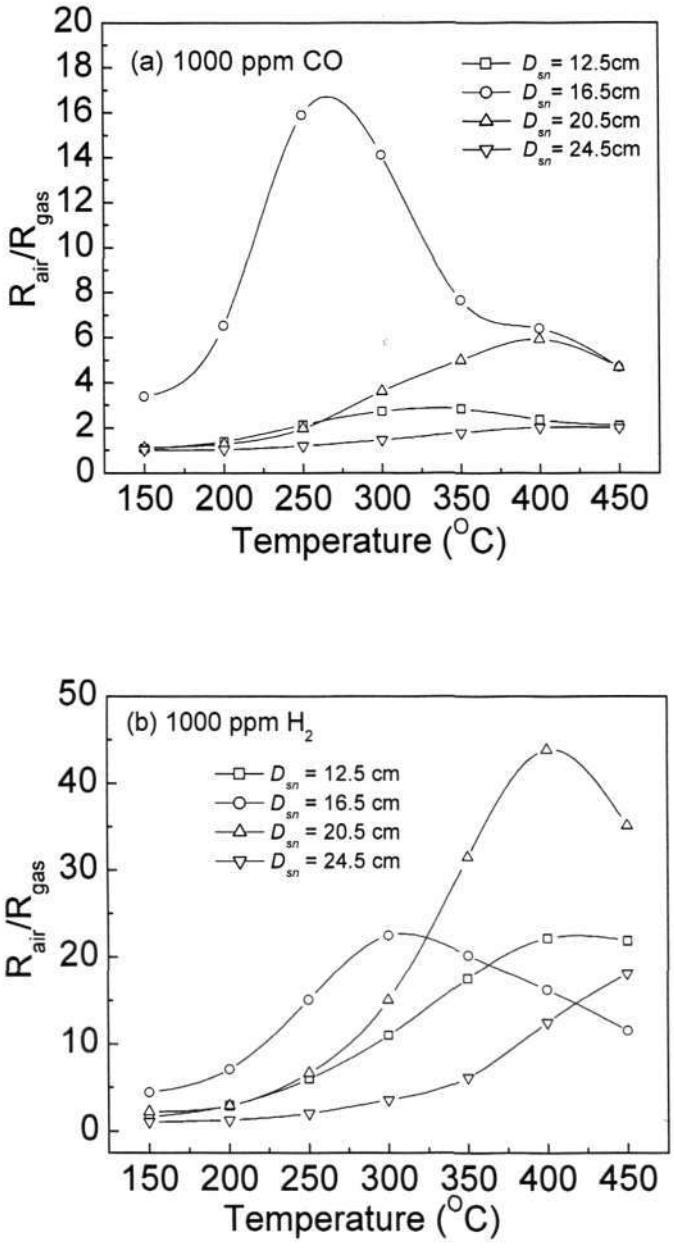

Figure 4-10 Gas sensitivity of SnO_2 thin films deposited at different D_{sn} to (a) 1000 ppm CO and (b) 1000 ppm H_2.

It has been reported that the different crystallographic planes have different distances between Sn atoms, according to the following series $d_{(110)} \sim d_{(100)} < d_{(101)} < d_{(001)}$ [86]. Tin atoms are centers of oxygen chemisorption, and therefore the change of indicated distance must influence the rate of dissociative oxygen chemisorption, which in turn

becomes a controlling factor of gas sensing phenomena [40]. The influence of the various structural parameters of metal oxides, namely thickness, grain size, porosity, grain faceting, agglomeration, film texture, sensor geometry, and others that have been listed by Korotcenkov [85] must be taken into consideration in addressing the overall gas sensor performance. For example, the SnO_2 thin films deposited at D_{sn} = 12.5 cm has a rough surface morphology with large grain size compared to others (figure 4-3), and the film was thickest with a preferred orientation of (101). While the SnO_2 thin films deposited at D_{sn} = 24.5 cm has the smallest grain size, lowest thickness, but with a preferred orientation of (110). The combination of these various structural parameters has given the sensing results shown in figure 4-10. Hence, it would be difficult to compare and explain the reasons behind the difference in gas sensitivity plot of SnO_2 thin films deposited at various D_{sn} as there was more than one structural parameters change that could affect the overall gas sensing performance. However, the possibility to produce different microstructures with specific growth orientation using the custom ICP-CVD system has opened up many opportunities to tailor the gas sensing performance of nanocrystalline SnO_2 thin films via microstructure modification.

CHAPTER FIVE

SnO_2 NANOROD THIN FILMS FORMATION BY POST PLASMA TREATMENT

5.1 Introduction

Surface modification and microstructure optimization of the SnO_2-based sensor materials have been demonstrated to be an effective way to obtain high gas sensitivity and selectivity. A traditional way to improve the performance of SnO_2-based sensors is the doping of tin oxide with small amounts of suitable dopants such as Pd, Pt, Cu, Fe, Co, Mn, F, etc. [87-89]. Surface modification of a SnO_2-based CO gas sensor with sulfuric acid or thiourea solution was reported by Ozaki and co-workers to notably enhance the sensitivity to CO, the selectivity against H_2, and the long-term stability of the sensor [90,91]. However, optimization of microstructure of sensor materials was also demonstrated to be an effective way to obtain high gas sensitivity and selectivity. Tan et al. [92] reported a promising method of using mechanical alloying in producing nanocrystalline $x SnO_2$-$(1-x)\alpha Fe_2O_3$ powders as ethanol sensor with good selectivity over CO and H_2 gases. The mechanical milling modified the powder microstructures by decreasing the agglomerate size by more than 20-fold and created nano-sized particles with enormous oxygen dangling bonds at their surfaces. Hyodo and co-

workers reported that the modification of conventional SnO_2 powder with mesoporous SnO_2 powder was effective in improving gas sensing properties of conventional SnO_2 powder to both NO and NO_2 at a concentration level of 10 ppm [93].

Motivated by the capability of ICP-CVD system in producing distinct surface morphology of the SnO_2 thin films at different D_{sn}, the as-deposited granular SnO_2 thin films were post-treated in the middle of ICP. The aim was to explore the microstructure modification of the granular SnO_2 thin films via plasma sputtering method. During the plasma treatment, SnO_2 nanorods in random orientation were in situ grown on the SnO_2 thin films. The effects of post plasma treatment parameters, namely the RF power, plasma treatment duration, gaseous composition, and plasma type on the growth of the SnO_2 nanorods have been systematically studied and discussed. The growth mechanism of the SnO_2 nanorod thin films was proposed and presented. Next, the gas sensing properties of the SnO_2 nanorod thin films were characterized, together with encouraging results of noble metal Pd addition to further enhance the gas sensitivity and selectivity.

5.2 Experimental details

The as-deposited SnO_2 thin films described in section 4.2 were subjected to post plasma treatment by placing them in the middle of ICP generated by 400 – 1200 W of RF power with a gas flow rate of 0 – 50 sccm for Ar and O_2 respectively. No precursor vapor was introduced in the chamber during the plasma treatment process.

5.3 Effect of post plasma treatment parameters

5.3.1 RF power

To study the effect of RF power on the microstructure of the SnO_2 thin films, the as-deposited SnO_2 thin films were treated in ICP plasma with different RF power settings. Figure 4-14 shows the XRD patterns of (a) as-deposited SnO_2 thin film and plasma-treated SnO_2 thin films in (b) 400 W, (c) 800 W and (d) 1200 W ICP for 40 minutes. The as-deposited SnO_2 thin film was well-crystallized even without substrate heating and all peaks can be indexed by Cassiterite SnO_2 (figure 5-1(a)). After plasma treatment, a second phase of Sn_2O_3 was found in the SnO_2 thin films treated in 800 W and 1200 W ICP (figures 5-1(c) and 5-1(d)). Sn_2O_3 could be regarded as an O deficient phase of SnO_2, and its presence was possibly caused by the strong ion bombardments effect in the high power plasma. It was noted that the intensity of diffraction peaks decreased with the increase of ICP power.

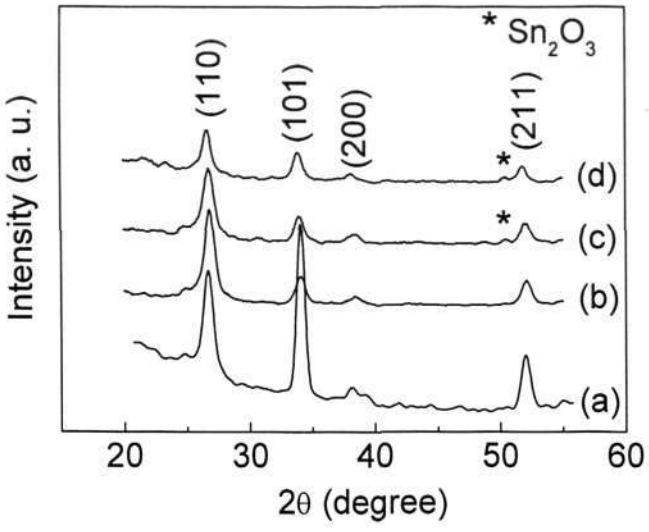

Figure 5-1 XRD patterns of (a) as-deposited SnO_2 thin films and plasma-treated SnO_2 thin films in (b) 400 W, (c) 800 W, and (d) 1200 W ICP for 40 minutes.

Figure 5-2 shows the SEM micrographs of the (a) as-deposited SnO_2 thin films and plasma-treated SnO_2 thin films in (b) 400 W, (c) 800 W and (d) 1200 W ICP for 40 minutes. The as-deposited SnO_2 thin films were granular and the grain size was 20 nm. Uniform SnO_2 nanorods with diameter of 10 nm and length of 90 nm were observed in the SnO_2 thin films treated in 400 W and 800 W ICP. However, the SnO_2 thin film treated in 1200 W plasma seemed to be damaged and only some large ball-like particles with short SnO_2 nanorods were found. The surface microstructure of the SnO_2 thin films was reconstructed during plasma treatment under different RF power settings.

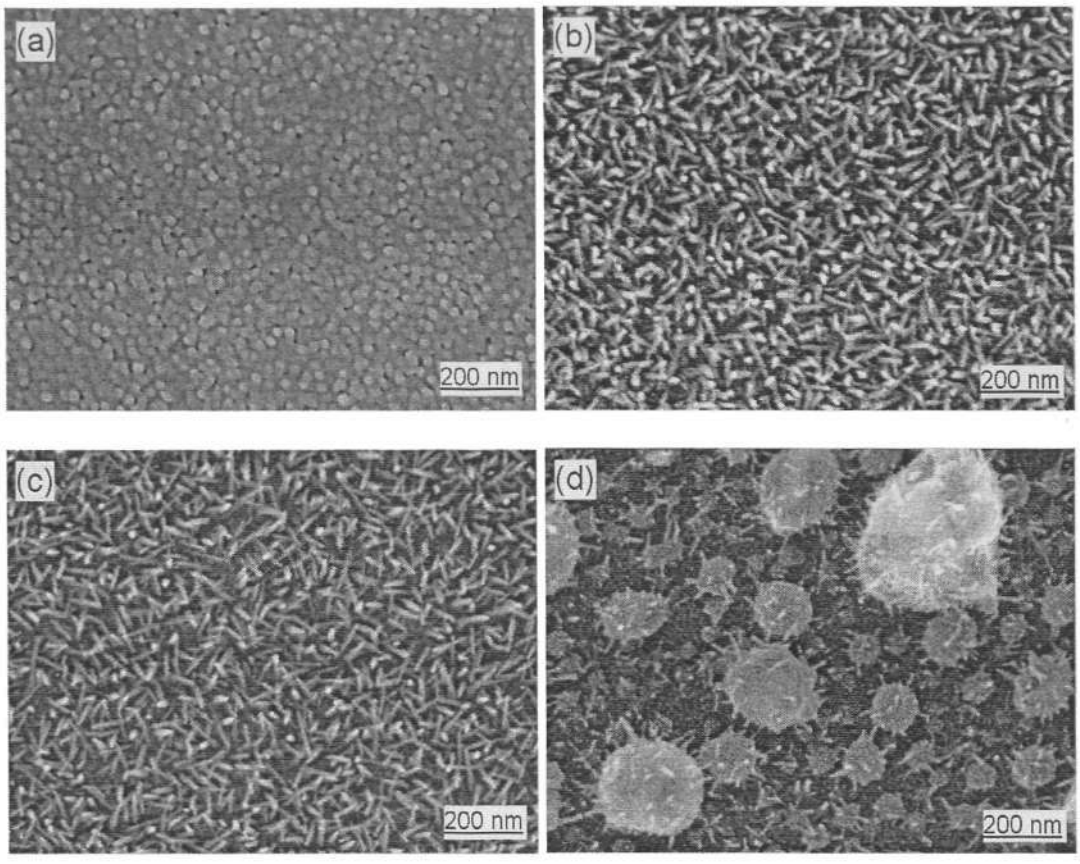

Figure 5-2 SEM micrographs of the (a) as-deposited SnO_2 thin film and plasma-treated SnO_2 thin films in (b) 400 W, (c) 800 W and (d) 1200 W ICP for 40 minutes.

A thick SnO_2 thin film with columnar grains was selected to undergo post plasma treatment in 400 W and 1200 W ICP for 120 minutes respectively. Figure 5-3 shows the XRD patterns of the (a) as-deposited SnO_2 thin films treated in (b) 400 W and (c) 1200 W ICP for 120 minutes. It is shown that the film was well crystallized and showed (101) preferred orientation after plasma treatment. Figure 5-4 shows the SEM micrographs of the (a) as-deposited SnO_2 thin films treated in (b) 400 W and (c) 1200 W ICP for 120 minutes. The as-deposited SnO_2 thin film was very dense and some flower-like particles were observed as shown in figure 5-4(a). The cross section view of the thin films showed that the grains in the film were columnar-like. After a post treatment at 400 W for 120 minutes, some nanorods grew from the film (figure 5-4(b)). As the RF power increased to 1200 W, the nanorods grew longer (figure 5-4(c)). High RF power processing showed different effects on the SnO_2 thin films with different microstructures, and no evidence of film damage at high RF power as shown in figure 5-4(c) was observed. It seems that high RF power is favored to the growth of nanorods from well-crystallized thin films.

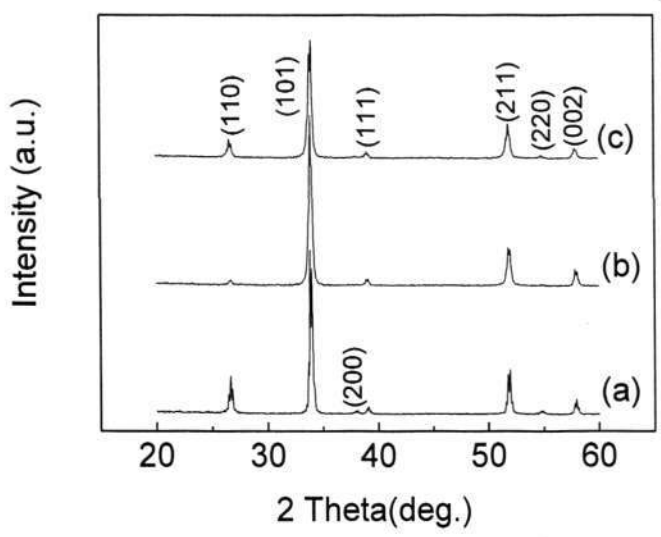

Figure 5-3 XRD patterns of the (a) as-deposited SnO_2 thin films treated in (b) 400 W and (c) 1200 W ICP for 120 minutes.

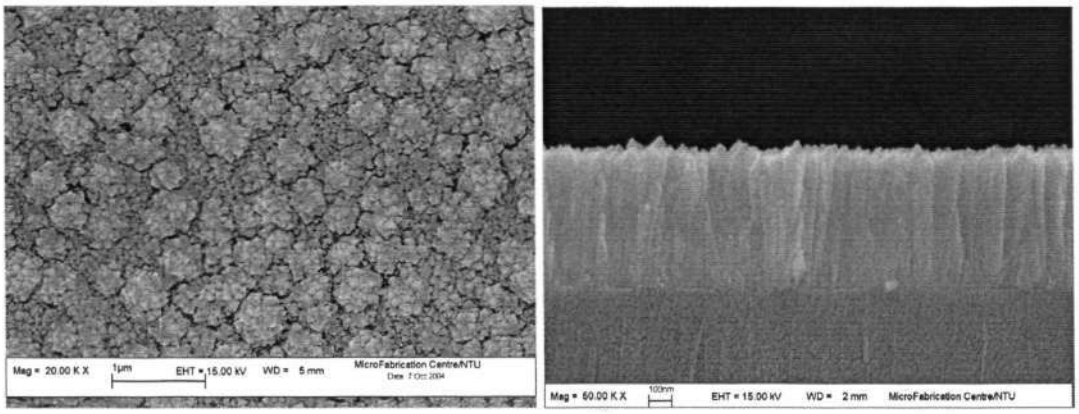

(a) as-deposited SnO_2 thin film

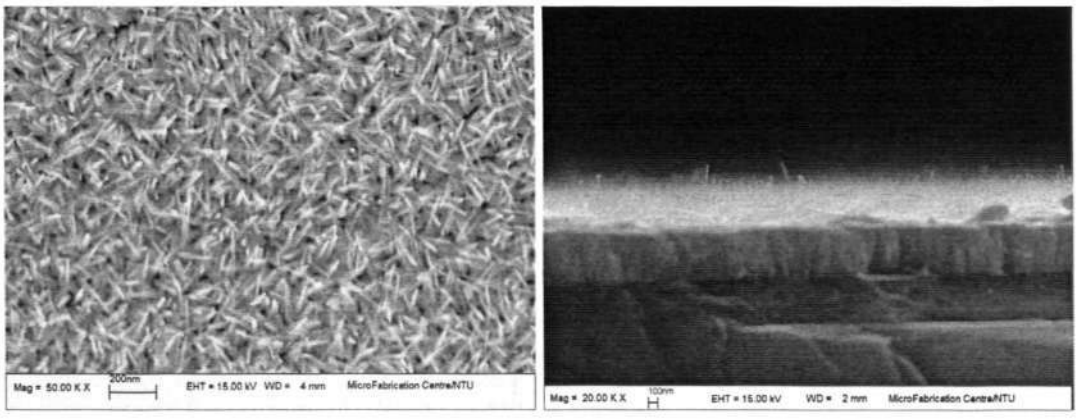

(b) 400 W

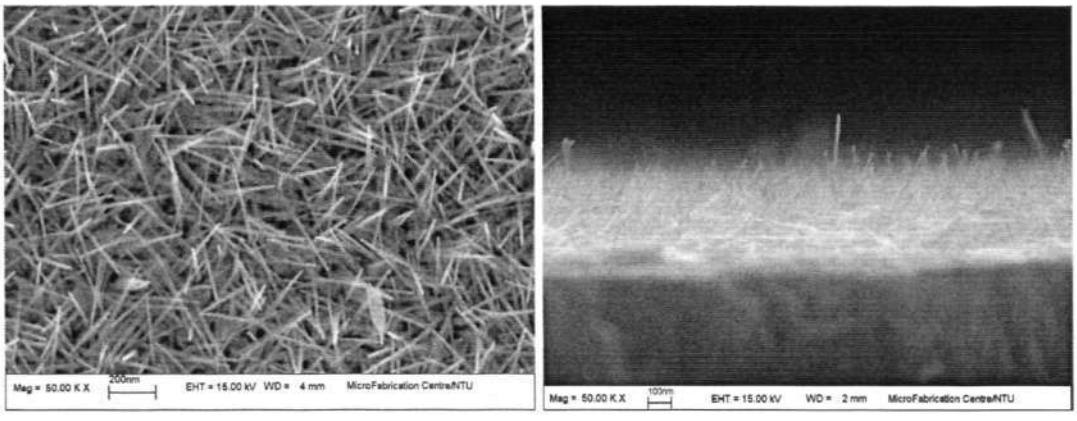

(c) 1200 W

Figure 5-4 SEM micrographs of the (a) as-deposited SnO_2 thin films treated in (b) 400 W and (c) 1200 W ICP for 120 minutes.

5.3.2 Gas flow ratio of Ar/O_2

The effect of gas flow ratio of Ar/O_2 for the plasma on the morphology of the plasma-treated SnO_2 thin films was also studied. Figure 5-5 shows the SEM micrographs of the SnO_2 thin films treated in 1200 W plasma with (a) Ar/O_2 = 25 sccm/25 sccm, (b) Ar/O_2 = 50 sccm/0 sccm, (c) Ar/O_2 = 0 sccm/50 sccm and (d) Ar/O_2 = 50 sccm/50 sccm for 40 minutes. It seemed that the ratio of Ar/O_2 played an important role in determining the morphology of the plasma-treated thin films. For Ar/O_2 = 50 sccm/50 sccm shown in figure 5-5(d), only short nanorods on particles were found in the plasma-treated sample. When Ar and O_2 flow rate decreased to 25 sccm respectively, some separated urchin-like structures formed by the coagulation of nanorods with diameter of 18 nm and length of 135 nm at one end were observed (figure 5-5(a)). When pure Ar plasma was used, the film was porous and no nanorods were observed (figure 5-5(b)). Pure O_2 plasma was also used to treat the SnO_2 thin films with only some dispersed short rod-like particles observed in the treated sample (figure 5-5(c)). Such findings indicated that the gaseous composition of the ICP showed strong effects on the microstructure of the plasma-treated sample. The plasma generated by a mixture of Ar and O_2 gas was necessary for the formation of SnO_2 nanorods.

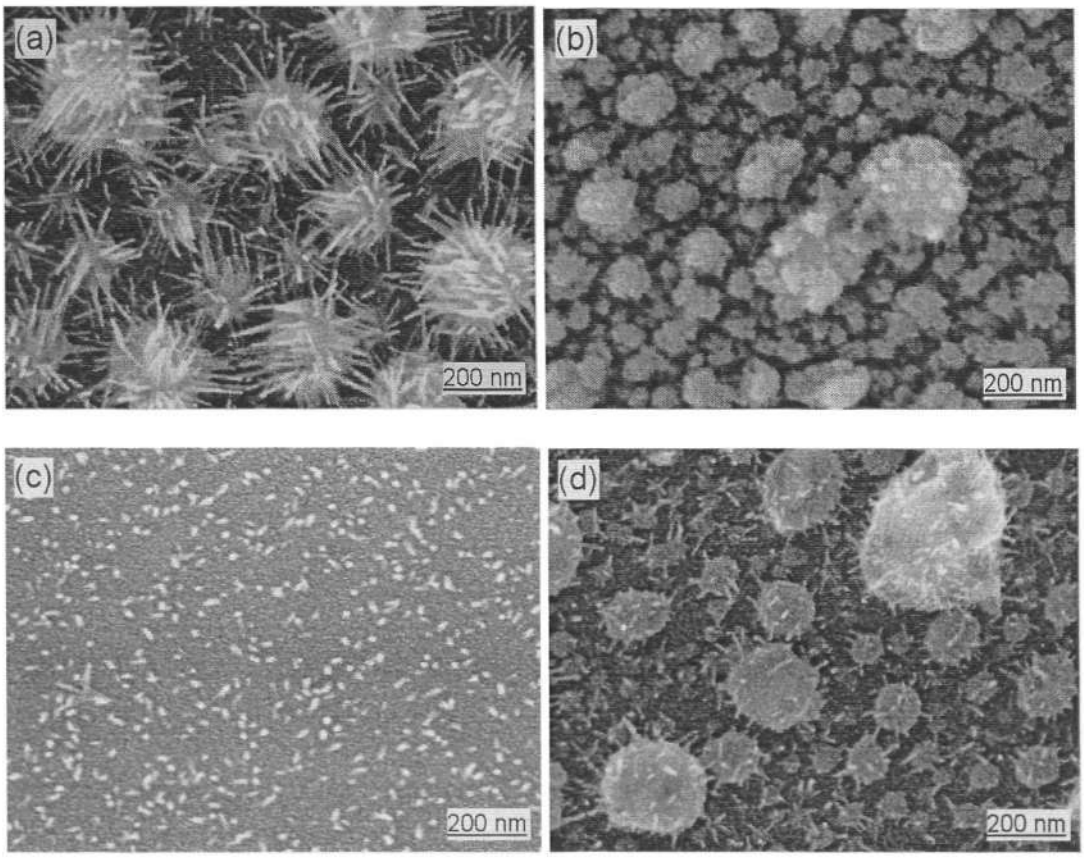

Figure 5-5 SEM micrographs of the SnO_2 thin films treated in 1200 W plasma with (a) Ar/O_2=25 sccm/25 sccm, (b) Ar/O_2=50 sccm/0 sccm, (c) Ar/O_2=0 sccm/50 sccm, and (d) Ar/O_2=50 sccm/50 sccm for 40 minutes.

5.3.3 Type of plasma

It has been shown that SnO_2 nanorods could in situ grow from the SnO_2 thin films deposited by ICP-CVD after post ICP treatment. This has led to the investigation if other type of low temperature plasma, namely, capacitively coupled plasma (CCP) treatment could deliver the same effect. For comparison, the as-deposited SnO_2 thin films were treated separately in a Plasma Therm 790 CCP system and the ICP-CVD system using an Ar/O_2 flow rate ratio of 50 sccm/50 sccm for 40 minutes. The RF power setting was 400 W and 300 W for ICP and CCP treatment respectively, and the lower RF power setting for the CCP is due to the system power limitation. There are

two parallel plates used as electrodes in the CCP system, one serves as a cathode while the other is grounded. The sample was placed in the grounded electrode during CCP treatment. Figure 5-6 shows the SEM micrographs of the (a) as-deposited SnO_2 thin films treated in (b) 400 W ICP, and (c) 300 W CCP for 40 minutes. No nanorods were observed in the samples processed in the CCP, but the grain size of the films was smaller after CCP treatment. The electrode configuration and plasma generation mechanism for ICP and CCP are different, and therefore different effects on the microstructure of the SnO_2 thin films were observed after ICP and CCP treatment.

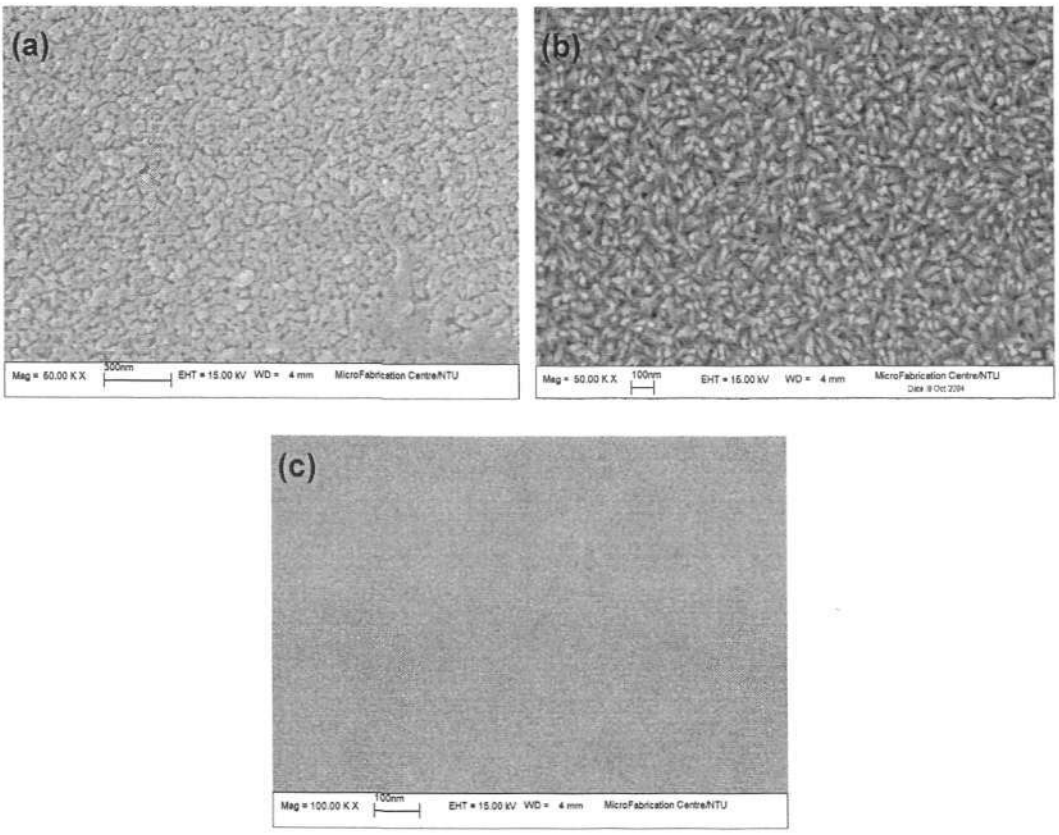

Figure 5-6 SEM micrographs of the (a) as-deposited SnO_2 thin films processed in (b) 400 W ICP and (c) 300 W CCP for 40 minutes.

5.4 Growth mechanism

Figure 5-7 shows the TEM image of a cluster of SnO_2 nanorods grown from the film matrix. The SnO_2 nanorods rooted in the SnO_2 thin film matrix could be described as a hybrid microstructure of one-dimensional SnO_2 nanorods grown on two-dimensional SnO_2 thin film. The nanorods are 5-15 nm in diameter and are 200-300 nm in length (figure 5-7(a)). A typical nanorod up to 500 nm long is shown in figure 5-7(b). The nanorod is needle-like and the diameter is 23 nm at the root and 5 nm at the tip. The lattice images were readily observed by HRTEM confirming that the nanorod is a single crystal. The interfacial spacing of the nanorod is 3.3 Å (figure 5-7(c)), corresponding to the (110) plane of tetragonal rutile crystal structure of SnO_2 (a = 4.738 Å and b = 3.187 Å). The fast Fourier transform (FFT) of the HRTEM image (inset in figure 5-7(c)) confirms that the facets of the nanorods are parallel to the (110) and $(1\bar{1}0)$ planes, respectively. The growth direction of the nanorod is determined to be [110], which is different from other reported growth directions such as [101] in [94,95], [001] in [31,96,97], $[11\bar{2}]$ in [98], [200] in [99], and [301] in [100].

The SnO_2 nanorods were directly grown from as-deposited SnO_2 thin films during ICP treatment without the assistance of metal catalysis and additional substrate heating. Therefore, no evidences support the vapor-liquid-solution (VLS) or vapor-solid (VS) growth mechanism. A sputtering-redeposition mechanism is proposed and published in [94]. During the plasma treatment, the films were sputtered by the bombardment of heavy ions such as Ar^+ in the plasma, and then the films species generated by the sputtering redeposited and rearranged back on the films. As the competing effects of plasma sputtering and redeposition of the films occurred simultaneously during plasma treatment, only those SnO_2 nuclei growing along their preferential growth orientation

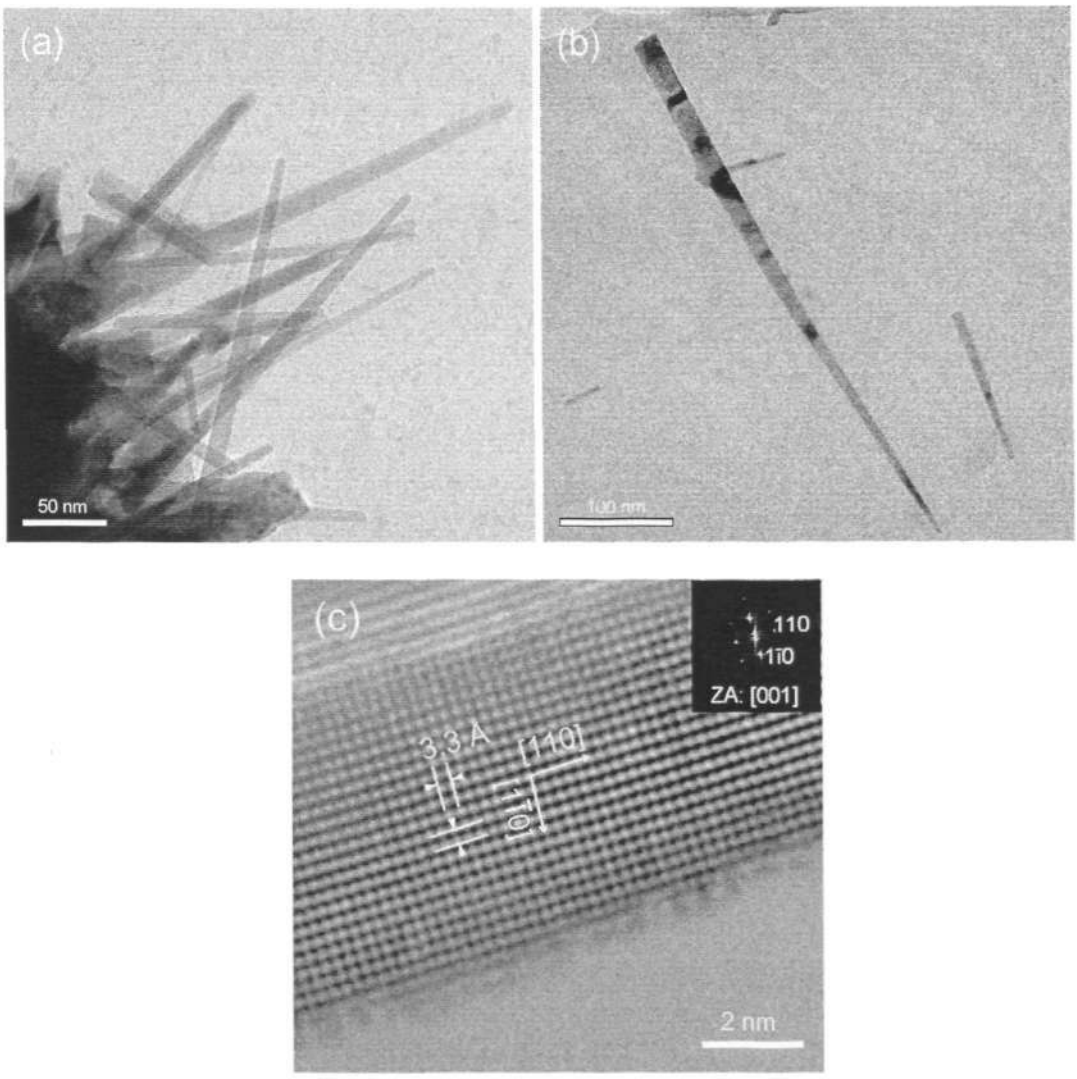

Figure 5-7 Bright field TEM images of (a) a cluster of SnO_2 nanorods and (b) a typical SnO_2 nanorod. (c) HRTEM image of the nanorod (inset is Fourier transform of the HRTEM image) [101].

could grow to form nanorods. The nanorod growth processes were observed by SEM (figure 5-8). It shows that the as-deposited SnO_2 thin film is well crystallized with a dense microstructure composed of compacted columnar grains grown directly from the SiO_2/Si substrate (figures 5-8(a) and 5-8(b)). After treating in the plasma for 5 min and 10 min, short SnO_2 nanorods in their initial growth stage of redeposition were observed (as shown in figures 5-8(c) and 5-8(d) respectively). The TEM observation shows that the nanorods grow in situ from the grains in the film matrix (figure 5-9(a)).

After treating in the plasma for 40 minutes, the SnO_2 nanorods grew longer in random direction while the thickness of the film matrix decreased (figures 5-8(b) and 5-8(f)). The film matrix was caverned by the continuous sputtering etching of the ICP, so the compacted columnar grains in the as-deposited film (as shown in figure 5-8(b)) became separated from each other after plasma treatment (figure 5-9(b)).

The effects of RF power, gas flow ratio of Ar/O_2 and plasma type on the growth of the SnO_2 nanorods can be explained based on the proposed sputtering-redeposition mechanism. The plasma sputtering etching rate increased with the increase of RF power and resulted in a decrease of films thickness after plasma treatment. Hence, the intensity of the XRD peaks shown in figure 5-1 decreased with the increase of RF power. When the RF power setting was too high, the sputtering etching effect was predominant and the etching rate was much higher than redeposition rate. Therefore, the films would be spoilt and redeposition was suppressed when the film was very thin (as shown in figure 5-2(d)). The influence of the gas composition of the plasma was also observed. The sputter effect of pure O_2 plasma was weak and thus no nanorods were formed. However, a total absence of O_2 could lead to a strong sputtering effect of the pure Ar plasma and the redeposition of the films species suppressed as SnO_2 were not formed under neutral or reducing atmospheres [101,102]. The type of plasma was also critical for the growth of SnO_2 nanorods on the SnO_2 thin films. The plasma sputtering etching effect in the CCP plasma was predominant and hence, the redeposition of the films was suppressed and no nanorods were observed on the films treated in CCP [102].

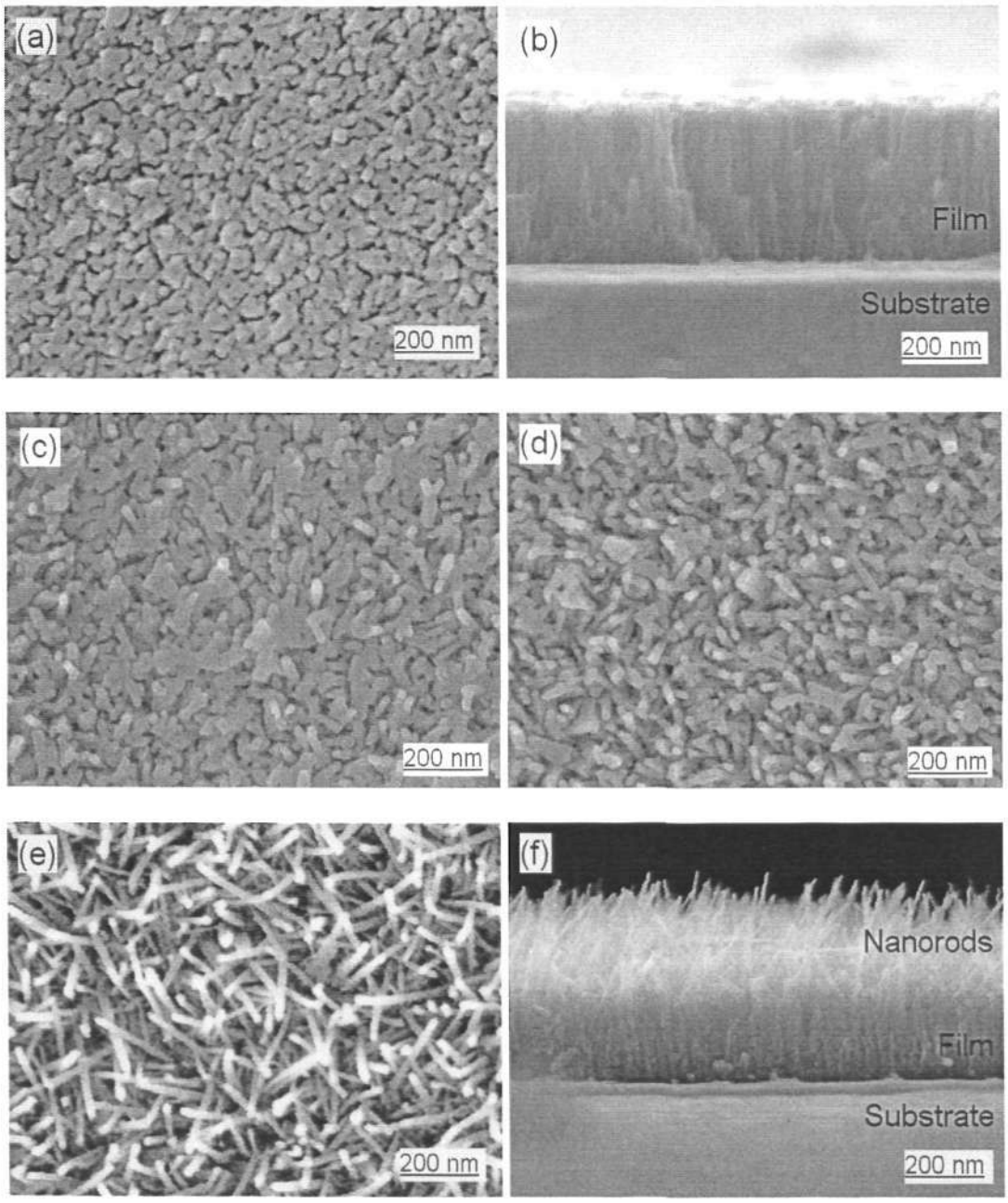

Figure 5-8 SEM images of as-deposited and plasma-treated SnO_2 thin films. (a) Planar view and (b) cross-sectional view of as-deposited SnO_2 thin film. Evolution of microstructure after treatment in 1.2 kW plasma for (c) 5 min and (d) 10 min. (e) Planar-view and (f) cross-sectional view of SnO_2 thin film treated in 1200 W plasma for 40 minutes [101].

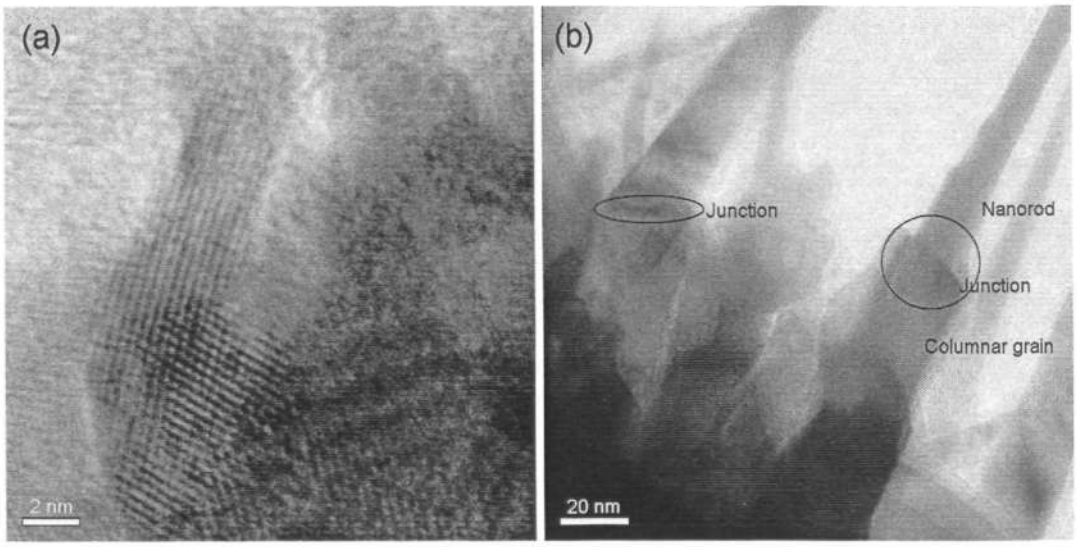

Figure 5-9 TEM images of (a) the nanorods in their initial growth stage and (b) the film treated in 1200 W plasma for 40 minutes [101].

5.5 Gas sensing properties

For the SnO_2-based sensors, the changes in resistance were mainly caused by the adsorption and desorption of gas molecules on the surface of sensing structure. It was reported that the sensitivity could be exponentially enhanced when grain size was reduced to a scale comparable to the space-charge length [39,103]. As grains size decreased, the optimal operating temperature also decreased remarkably and room temperature detecting CO gas was reported in the SnO_2 nano-wires and nano-ribbons gas sensors [23,104].

Figure 5-10 shows the FE-SEM micrographs of the (a) as-deposited SnO_2 thin film and (b) plasma-treated SnO_2 thin film. The as-deposited SnO_2 thin film was granular and the grain size was about 20 nm (figure 5-10(a)). After plasma treatment, SnO_2 nanorods in uniform size with diameter of 7 nm and length of 100 nm were observed

on the plasma-treated SnO_2 thin film (figure 5-10(b)). The thickness of the SnO_2 nanorod thin films are ~300 nm.

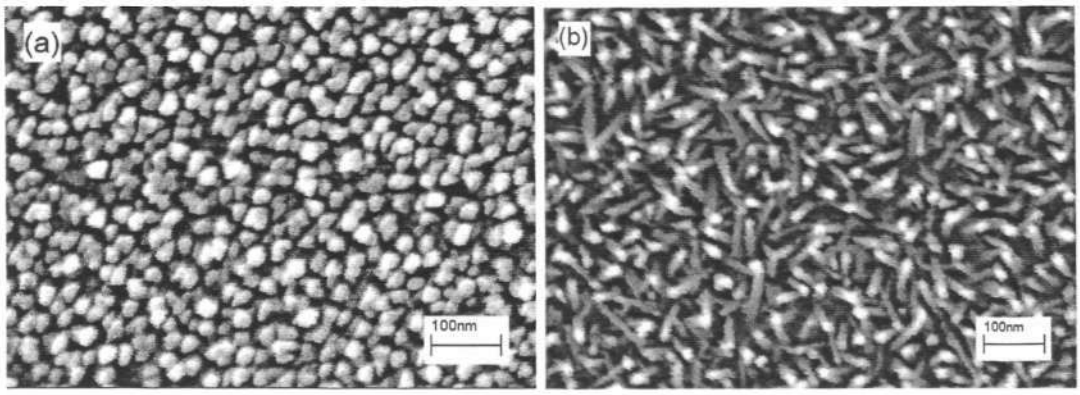

Figure 5-10 SEM micrographs of (a) as-deposited SnO_2 thin film and (b) plasma-treated SnO_2 thin film [94].

Figure 5-11 shows the gas sensitivity vs. operating temperature of the as-deposited SnO_2 thin film and SnO_2 nanorods thin film. The test gas was composed of either 1000 ppm CO, H_2 or ethanol in dry air with a total flow rate of 500 sccm. The maximum sensitivity (S = 3.8) towards CO gas of the as-deposited SnO_2 thin film was optimal at 360 °C. After plasma treatment, the maximum sensitivity of the SnO_2 nanorods thin film towards CO gas increased 6.5 times with a 95 °C decrease in the optimal temperature. The ethanol and H_2 gas sensitivity of the SnO_2 nanorods thin film was found to increase twofold, while the associated optimized operating temperature decreased 70 °C for H_2 and 130 °C for ethanol respectively.

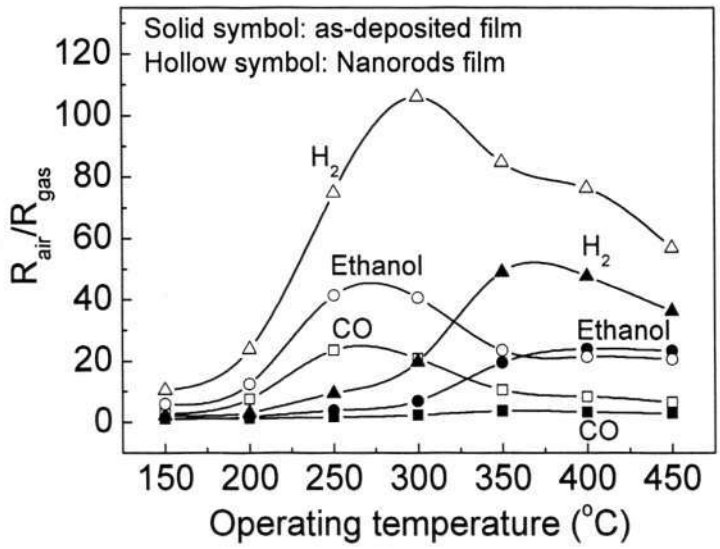

Figure 5-11 Gas sensitivity vs. operating temperature of the as-deposited SnO_2 thin film and SnO_2 nanorod thin film [101].

For the as-deposited SnO_2 thin film with surface grains in nano-scale, the surface-to-volume ratio, although high, is still relatively lower than plasma-treated SnO_2 thin film with nanorods. Furthermore, only a thin layer close to film surface can be activated during gas detection. For the plasma-treated SnO_2 thin film, diameter of the nanorods was 7 nm and was very close to the space-charge length 6 nm of SnO_2. Furthermore, the nanorods were rooted in the plasma-treated thin film in one end and randomly stretched outwards at the other end. This generated a highly porous structure and enabled both the analyte and the background gas to access all the surfaces of SnO_2 nanorods as well as the SnO_2 thin film. In this case, both the 1-D nanorods and 2-D thin film could contribute to the chemical reactions at all their surfaces. Hence, the whole device could be seen as SnO_2 nanorod antenna arrays integrated on the SnO_2 thin film matrix. This unique 1-D and 2-D hybrid structure of the plasma-treated SnO_2 thin film resulted in high sensitivity at lower optimal operating temperature. It

indicates that the nanorod thin films are a good candidate for miniaturized and ultrasensitive gas sensors. This result has been published in [101].

To determine the CO gas sensing properties of the as-deposited and plasma-treated SnO_2 thin films, the devices were cycled at their optimized temperatures, 330 °C for the as-deposited film and 250 °C for the plasma-treated film, through different CO concentrations. Figure 5-12(b) show the response and recovery time at various CO concentrations calculated from figure 5-12(a). Here, the response and recovery time were defined as the time needed for the resistance of the sensors to reach within 10% of the final equilibrium value for a given concentration. Figure 5-13 shows comparative study of the CO and H_2 response properties of the as-deposited SnO_2 thin film and SnO_2 nanorods thin film. In this case, the test gas was 200 ppm CO or H_2 in dry air and operating temperature was 270 °C for CO and 300 °C for H_2. Compared with the as-deposited SnO_2 thin film, the SnO_2 nanorod thin film showed higher sensitivity at lower operating temperature, faster response and shorter recovery time. It is well known that the response and recovery time of conductometric sensors are determined by the adsorption-desorption kinetics. Kolmakov and Moskovits reported that the average time taken by the photo-excited carriers to diffuse from the interior of an oxide nano-wire to its surface was greatly reduced with respect to electron-to-hole recombination times [61]. The rapid diffusion rate of electrons and holes to the surface of nanorods allows the analyte to be rapidly adsorbed/desorbed from the surfaces and it helps to decrease the response/recovery time of the nanorods.

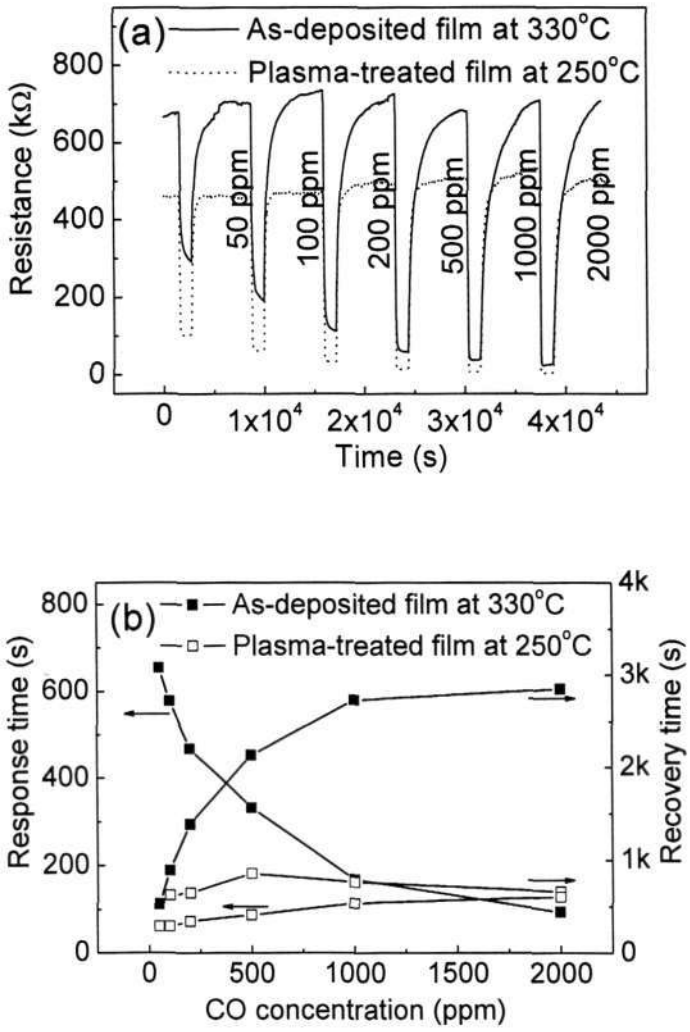

Figure 5-12 CO response properties of as-deposited and plasma-treated SnO_2 thin films. (a) CO gas response to various concentrations and (b) response time and recovery time vs. CO concentrations [94].

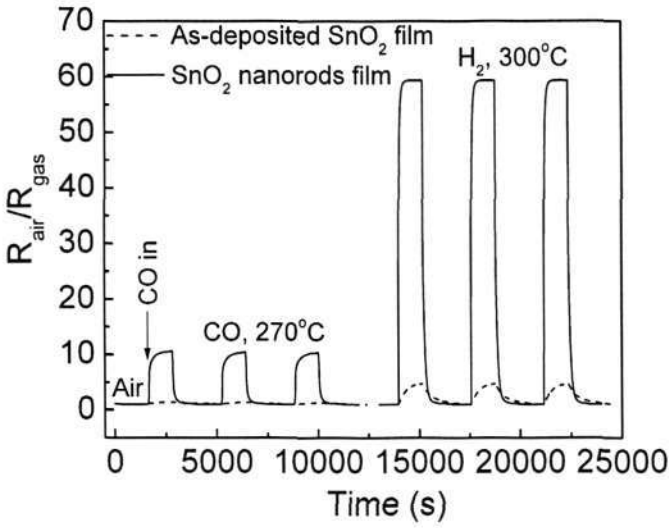

Figure 5-13 CO and H_2 response properties of the as-deposited SnO_2 thin film and SnO_2 nanorod thin film [101].

5.5.1 Surface doping with Pd

The 2 nm thick Pd clusters deposited by electron beam evaporation were used to modify the surface chemical state of the SnO_2 nanorods thin film. Figure 5-14 shows the TEM image of the Pd-functionalized nanorods. Well-dispersed Pd nanoparticles with an average size of 3 nm are clearly observed across the surface of SnO_2 nanorods under TEM observation. It has been reported that subsequent annealing after noble metal deposition in the temperature range of 300 – 600 °C was necessary to promote the forming of metallic clusters, improve the homogeneity of their distribution by layer thickness, and stabilize the properties of gas sensing matrix [105]. For our Pd-doped SnO_2 nanorod thin films, no agglomeration of Pd particles was found after 600 °C post annealing and the SnO_2 nanorods maintained its single crystalline structure after post annealing as observation under the HRTEM. The two interfacial spacings of the nanorod shown in figure 5-14(b) are 3.5 and 2.7 Å respectively, corresponding to (110)

and (101) planes of the tetragonal rutile crystal structure of SnO_2 (a = 4.738 Å and b = 3.187 Å). This result has been reported in [106].

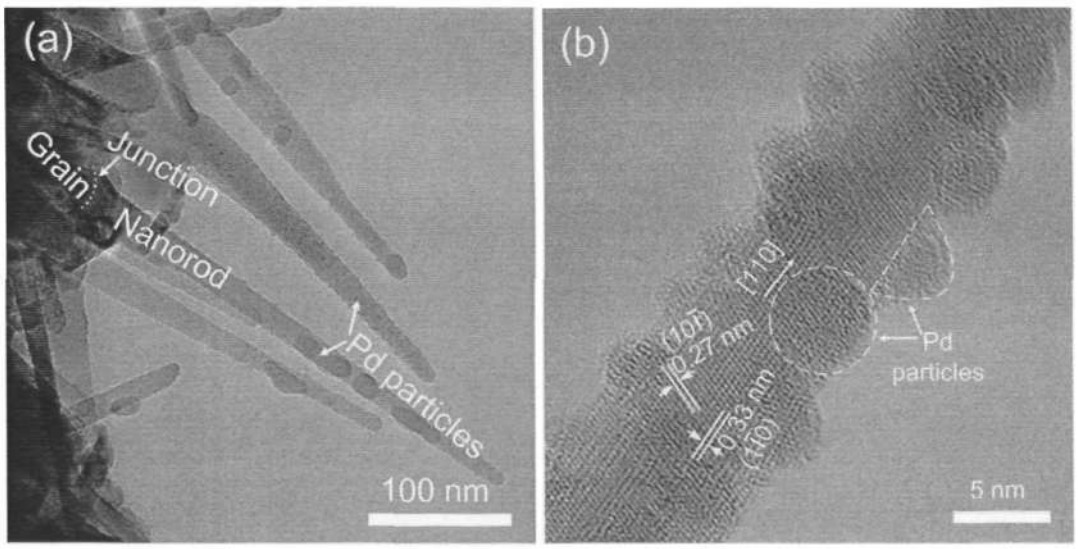

Figure 5-14 (a) TEM image of well-dispersed Pd nanoparticles on SnO_2 nanorods thin film and (b) HRTEM image of a typical Pd-doped SnO_2 nanorod [106].

Figure 5-15 shows the gas sensitivity of both un-doped and Pd-doped SnO_2 nanorod thin films as a function of operating temperature in the range from 150 to 450 °C. The testing gases were 1000 ppm CO, H_2, or ethanol in dry air with a total flow rate of 500 sccm. The Pd-doped SnO_2 sensor showed enhanced response to both H_2 and ethanol with 6 and 2.5 times better sensitivity compared to the un-doped SnO_2 sensor. Similar enhancing effect was however not found for CO. The un-doped SnO_2 sensor was 7 times more sensitive with a 100 °C lower optimized operating temperature. This behavior was opposite to those reported in the literature where Pd doping promotes an increase in the gas response and a shift of the response maximum towards lower temperature [107,108]. Possible explanation on such peculiar behavior could be associated with the Pd concentration in the SnO_2 nanorods thin film. The study on

different Pd doping concentrations has shown effect on the gas sensing performance. Kim and his co-workers [109] reported lower CO sensitivities comparing the 1.0 wt% Pd bulk-doping SnO_2 thin films to their pure SnO_2 thin films at the operating temperature of 200 and 250 °C. Optimum Pd concentration was found to be 0.5 wt% from their investigation on CO detection. In our work, the Pd doping was fixed at 2 nm thickness using e-beam evaporation and followed by annealing. The Pd concentration could be optimal for H_2 detection but not CO.

It was interesting to note that ethanol detection showed a unique sensing behavior where the Pd-doped SnO_2 nanorod thin films exhibited higher sensitivities than the undoped SnO_2 nanorod thin films in the operating temperature range of 300 °C to 450 °C, and vice versa in the operating temperature range of 150 °C to 250 °C. This unique sensing behavior could again be attributed to the Pd doping concentration in the SnO_2 nanorod thin films. Optimal sensing performance similar to H_2 could be identified for ethanol detection by varying the Pd doping concentration in the SnO_2 nanorods thin films. Though the 2 nm Pd doping could be not optimal for CO and ethanol detection, the existing sensing characteristics have shown good selectivity properties for H_2 detection.

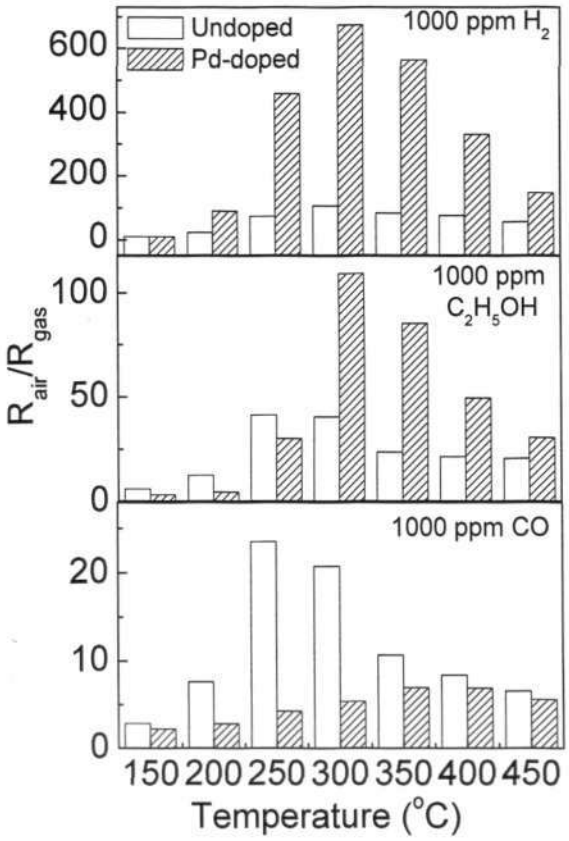

Figure 5-15 Gas sensitivity vs. operating temperature of un-doped and Pd-doped SnO_2 nanorod thin films [106].

The Pd-doped SnO_2 sensor was further tested at 20 times lower concentration than 1000 ppm. Figure 5-16 shows the sensitivity plot of the Pd-doped SnO_2 sensor towards 50 ppm CO, H_2, NH_3 and ethanol in dry air. Among the investigated gases, Pd-doped SnO_2 sensor showed the highest sensitivity towards H_2 with 33 times of relative resistance change following the introduction of the test gas. Similarly Mishra and co-workers found their Pd-doped SnO_2 thick film sensor possessed higher sensitivity for H_2 in comparison to LPG and CO [110]. The promoting effects of Pd in improving sensing performance have been attributed to the electronic sensitization mechanism which explained the formation of electron-depleted space charge layer inside the

semiconductor, induced by the changes in the oxidation state of Pd following oxygen adsorption and desorption [111]. The resultant increase in work function of semiconductor was casually observed from the increase in electrical resistance (R_{air}) [41]. In our case, the resistance of Pd-doped sensor was an order of magnitude higher than the as-deposited sample. Another chemical sensitization mechanism proposed that the dissociation of H_2 at the Pd surface forming atomic H that could lead to additional reaction schemes [110]. Reviewing the basic reaction scheme between adsorbed oxygen species on SnO_2 surface and molecular H_2 is a single step process presented as follows:

$$H_2\,(g) + O_{ad}^{-}(SnO_2) \rightarrow H_2O\,(g) + (SnO_2) + e^{-} \quad (4\text{-}1)$$

With the dissociation of H_2 at Pd surface, the additional reaction schemes are:.

$$H_2\,(g) \rightarrow H + H\ (\text{dissociation}) \quad (4\text{-}2)$$

$$H + SnO_2 \rightarrow H_{ad}(SnO_2) \quad (4\text{-}3)$$

$$H_{ad}(SnO_2) + O_{ad}^{-}(SnO_2) \rightarrow OH_{ad}^{-}(SnO_2) \quad (4\text{-}4)$$

$$OH_{ad}^{-}(SnO_2) + H_{ad}(SnO_2) \rightarrow H_2O\,(g) + (SnO_2) + e^{-} \quad (4\text{-}5)$$

In either reaction path, H_2O (g) is liberated as the final reaction product resulting in accumulation of electrons at the surface which is responsible for the increase in the conductance, and hence better sensitivity to H_2 for SnO_2 sensor doped with Pd was observed.

Shown in figure 5-17 is the response curve of the Pd-doped SnO_2 sensor for a step change in composition from air to 50 ppm H_2 in air at its optimized operating temperature of 300 °C. The response time was well within 120 s while the recovery time was within 15 min for the Pd-doped SnO_2 sensor. The Pd-doped SnO_2 sensor also

showed consistent response and full recovery throughout the cyclic test as shown in the inset of figure 5-17.

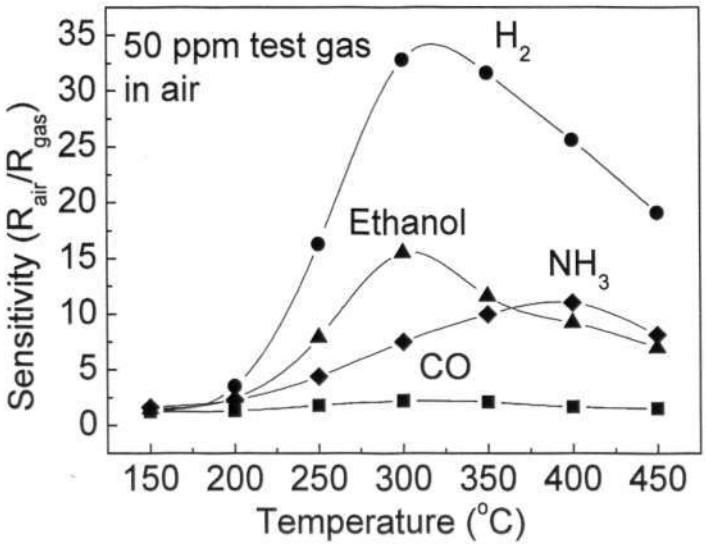

Figure 5-16 Sensitivity of Pd-doped SnO_2 nanorod thin films to H_2, CO, NH_3 and ethanol as a function of operating temperature [106].

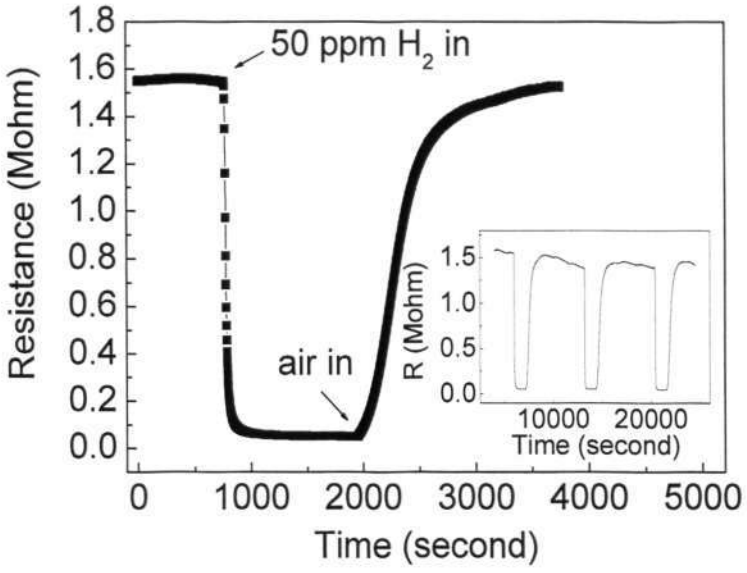

Figure 5-17 Response curve of Pd-doped SnO_2 nanorod thin films to 50 ppm H_2 at 300 °C [106].

CHAPTER SIX

DIRECT ONE-STEP SnO_2 NANORODS / NANOCOLUMNS ARRAY

6.1 Introduction

SnO_2 nanorod thin films formed by post plasma processing have brought forward a new way of tailoring the film microstructures to achieve a high surface area structure desirable for gas sensing application. The SnO_2 nanorod thin films form a unique hybrid structure of 1-D SnO_2 nanorods embedded in 2-D SnO_2 thin film matrix. The fabrication of gas sensors based on SnO_2 nanorod thin films is compatible with the prevailing microfabrication technology that emphasizes batch processing with good reproducibility. The very high surface-to-volume ratios and great surface activities of these nanostructures endow the gas sensors with inherently high sensitivity and short response time [94].

Following the promising results of the SnO_2 nanorod thin films, new attempt has been made to explore the possibility of depositing SnO_2 nanorods directly on the substrate. The 1-D nanorods structure with higher surface-to-volume ratios compared to conventional granular nanosized grains is anticipated to improve the sensing properties

of the gas sensor devices. In this chapter, we first report on the successful preparation of direct one-step SnO_2 nanorods array on SiO_2/Si substrate. The effects of various processing parameters on the structural properties of the synthesized nanorods array, together with the proposed growth mechanism are presented. The gas sensing characterization results obtained from the fabricated device of nanorods array are discussed with emphasis on the enhancement of sensing properties by Pd surface doping and oxygen vacancies alteration. Next, we report on the successful preparation of 1-D SnO_2 nanocolumns array by direct liquid injection ICP-CVD process. The effect of D_{sn} and gas sensing properties of the nanocolumn arrays are subsequently discussed.

6.2 SnO_2 nanorods array by ICP-CVD with bubbler delivery

6.2.1 Experimental details

In this section, the experimental details for the one-step SnO2 nanorods array prepared by ICP-CVD using bubbler delivery method will be presented. Dibutyltin diacetate (Aldrich, 98% purity), $(C_4H_9)_2Sn(OOCCH_3)_2$, was used as the tin precursor. The precursor temperature was maintained at 90 °C. Ar was used as the carrier gas at a flow rate of 50 sccm and 50 sccm O_2 was used as the reaction gas. The flow rate of Ar and O_2 used was reduced half compared to the preparation of SnO_2 nanocrystalline thin films described in section 4.2.1. A funnel-type quartz mixer was placed at the chamber nozzle inlet to homogenize the reactants prior to plasma activation. A 4″ SiO_2/Si wafer was used as the substrate and it was placed in the ICP zone for deposition. Again, there was no additional substrate heating during deposition or post annealing of the films.

6.2.2 Effect of substrate-nozzle distance

The substrate-nozzle distance, D_{sn} was denoted as the distance between the substrate and the injection nozzle inlet. The substrate was located in the middle of the plasma at D_{sn} = 8 cm and subsequent increase in D_{sn} indicated the downstream shift of the substrate from the middle of the plasma.

Figure 6-1 shows the XRD patterns of the SnO_2 nanorods deposited at D_{sn} = (a) 8 cm, (b) 10 cm, (c) 12 cm, (d) 14 cm, and (e) 16 cm for 2 hours. All diffraction peaks can be indexed as Cassiterite SnO_2 (PDF 41-1445). A shift of preferred orientation from (101) plane to (110) plane was noted with the increase of D_{sn} from 8 cm to 14 cm. The positioning of substrate at different locations in the plasma region could affect the growth orientation.

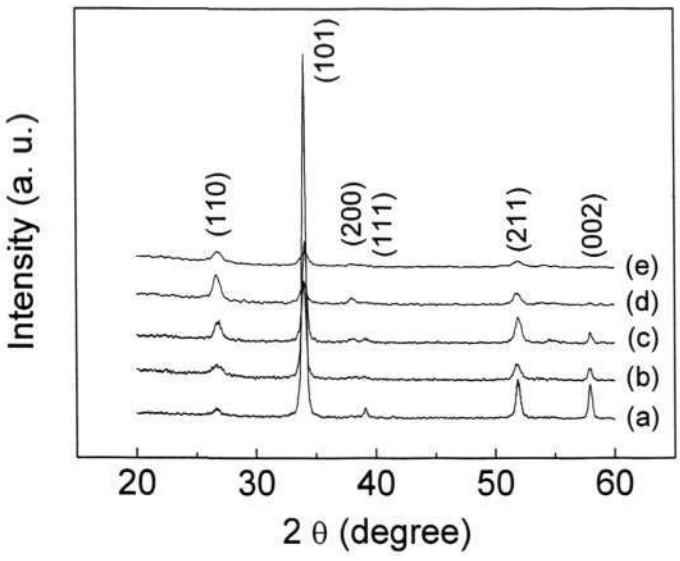

Figure 6-1 XRD patterns of the SnO_2 nanorods deposited at D_{sn} = (a) 8 cm, (b) 10 cm, (c) 12 cm, (d) 14 cm, (e) 16 cm for 2 hours.

Figure 6-2 shows the SEM micrographs of the SnO_2 nanorods deposited at D_{sn} = (a) 8 cm, (b) 10 cm, (c) 12 cm, (d) 14 cm, and (e) 16 cm. Both plane and cross-sectional views were shown to indicate the morphology and thickness of the deposited microstructure. Randomly oriented nanorods were observed in all the samples except for D_{sn} = 16 cm where the nanorods structure was just about to form. With the increase of substrate distance from the injection nozzle, the diameter and length of the nanorods structure was found to decrease owing to the slower growth rate with fewer precursor reactants reaching the substrate at the downstream of plasma.

(a)

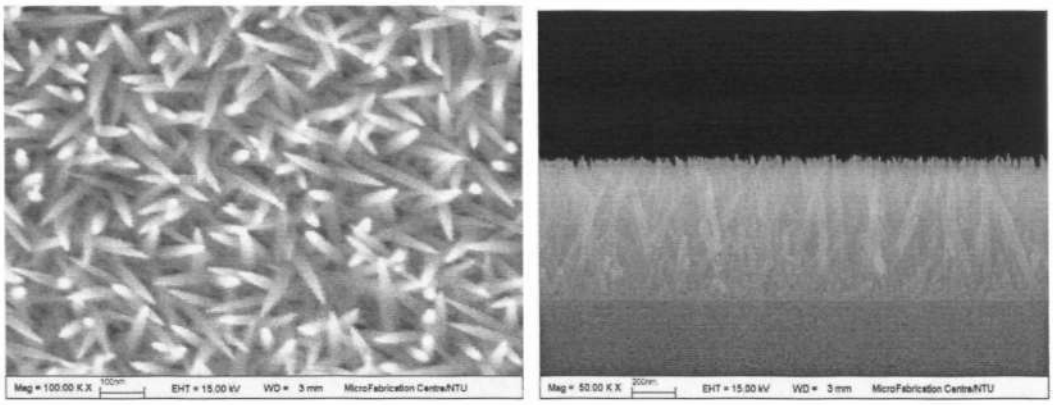

(b)

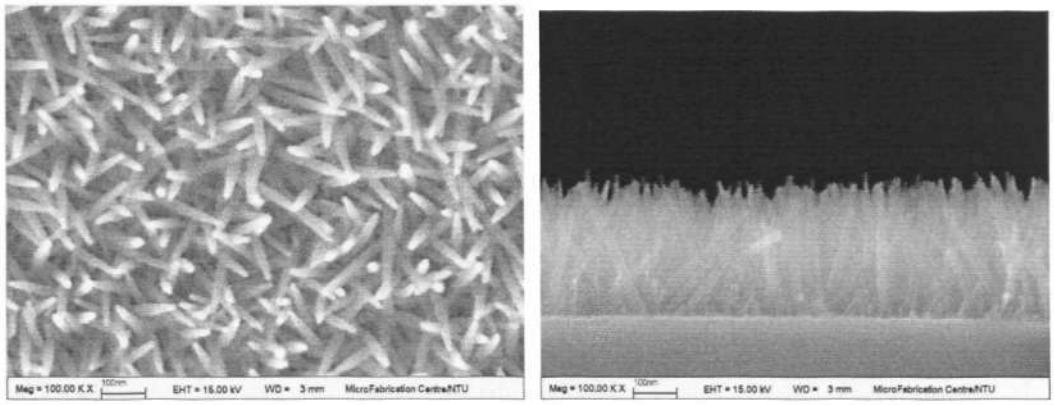

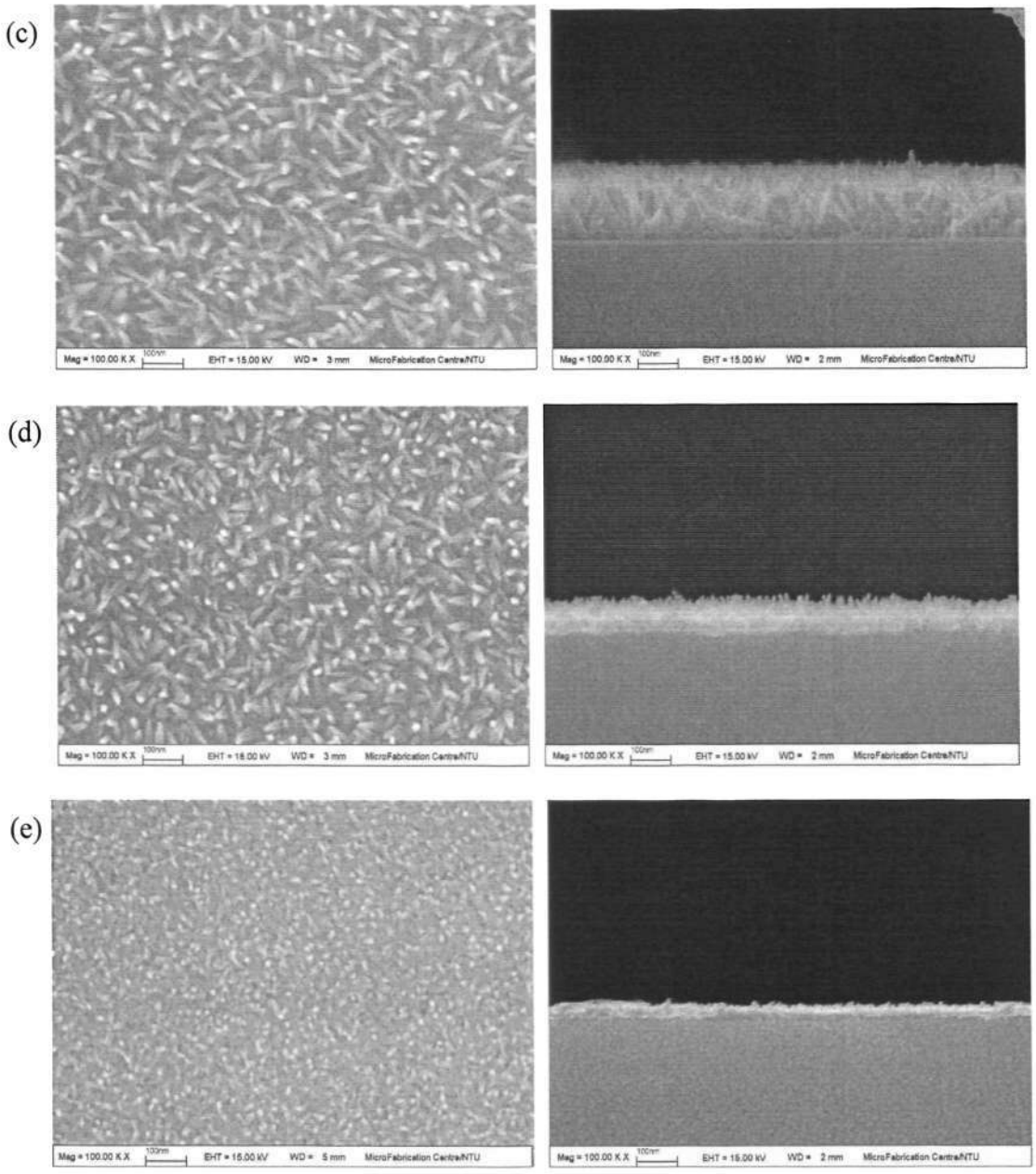

Figure 6-2 SEM plane view and cross-sectional views of the SnO_2 nanorods matrix deposited at D_{sn} = (a) 8 cm, (b) 10 cm, (c) 12 cm, (d) 14 cm, (e) 16 cm for 2 hours.

6.2.3 Effect of RF power

The RF power during deposition was found to affect the formation of SnO_2 nanorods. Figure 6-3 shows the XRD patterns of the SnO_2 nanostructures deposited at D_{sn} = 12 cm with RF power of (a) 400 W, (b) 600 W, (c) 800 W, (d) 1000 W, (e) 1200 W, and

(f) 1400 W for 2 hours. The nanostructures were well crystallized and all the peaks can be indexed as Cassiterite SnO_2 with a (101) preferred orientation observed. Figure 6-4 shows the SEM images of SnO_2 nanorods deposited at RF power of (a) 400 W, (b) 600 W, (c) 800 W, (d) 1000 W, (e) 1200 W, and (f) 1400 W for 2 hours. The nanostructures deposited at 400 W were composed of granular nano-sized grains while nanorods started to form at RF power of 800 W. The nanorods were found to grow 50 nm longer with the increase of RF power to 1400 W. The increase of RF power had promoted the sputtering by bombardment of heavy ions such as Ar^+ in the plasma, simultaneously with deposition. With the redeposition and rearrangement of the sputtered species, those SnO_2 nuclei that grew along their preferential growth orientation could grow up to form nanorods. This agrees well with our previous study on the effect of RF power in the growth of SnO_2 nanorods from SnO_2 thin films using post plasma treatment [102]. This result has been published in [112].

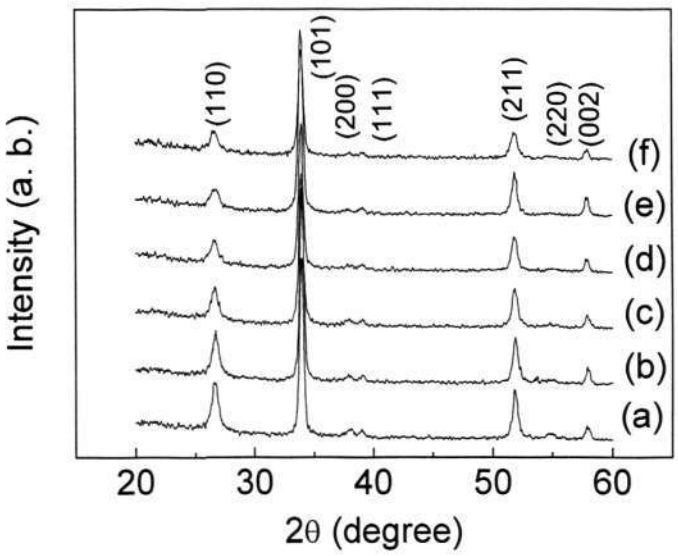

Figure 6-3 XRD patterns of SnO_2 thin films deposited at D_{sn} = 12 cm with RF power of (a) 400 W, (b) 600 W, (c) 800 W, (d) 1000 W, and (e) 1200 W for 2 hours.

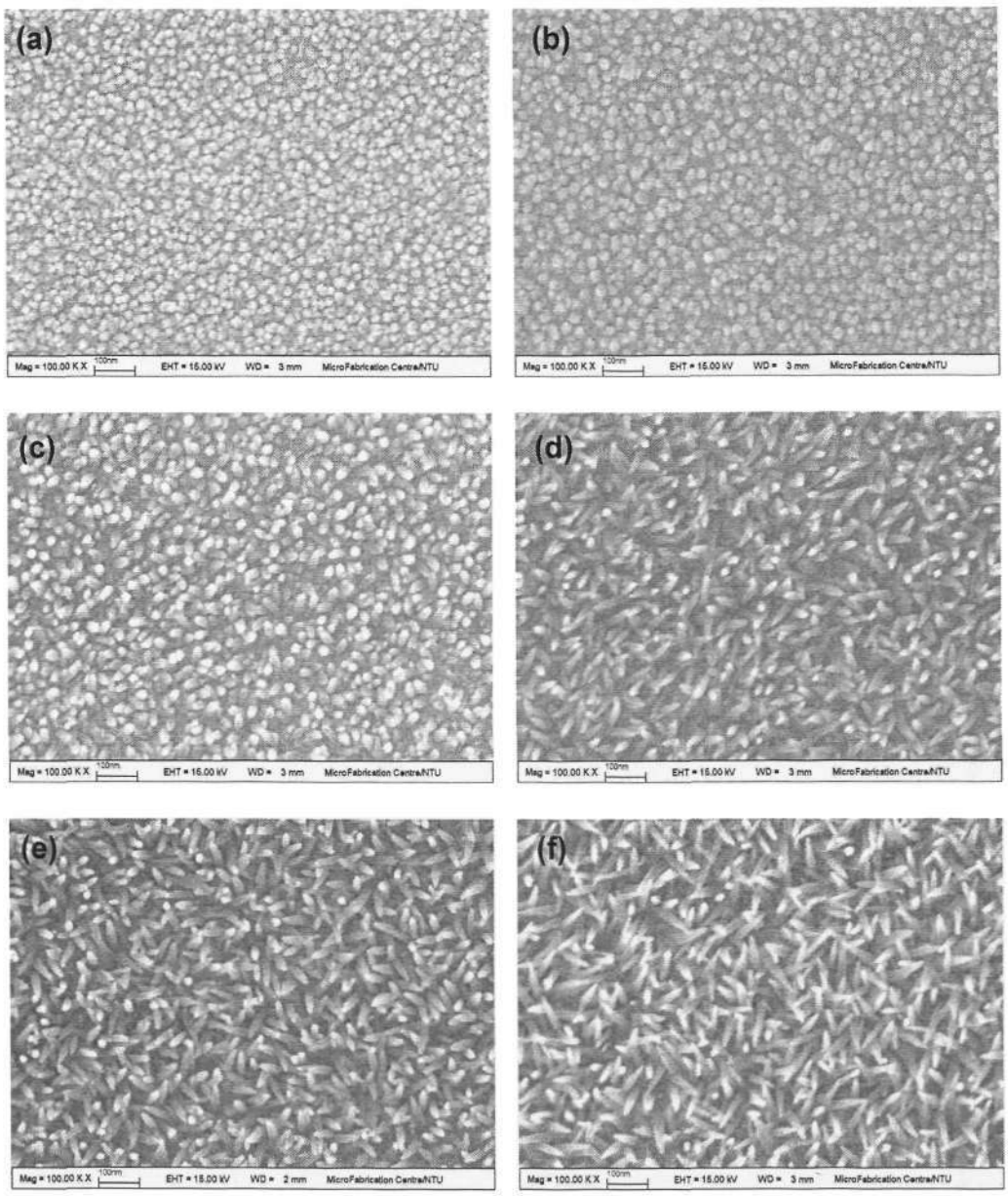

Figure 6-4 SEM images of SnO_2 nanorods deposited at D_{sn} = 12 cm with RF power of (a) 400 W, (b) 600 W, (c) 800 W, (d) 1000 W, (e) 1200 W, and (f) 1400 W for 2 hours.

6.2.4 Growth mechanism

Shown in figure 6-5(a) is the TEM image of the SnO_2 nanorods array. The SnO_2 nanorods were connected with each other at the roots and randomly stretched outward at the tips. The nanorods are 5 – 16 nm in diameter and 160 – 250 nm in length. Figure

6-5(b) shows a HRTEM image of a typical SnO_2 nanorod. The clear lattice images observed by the HRTEM indicate that the nanorod is a single crystal. Analysis of HRTEM image using FFT reconstruction confirmed the formation of rutile-structured SnO_2 with lattice constants a = 4.737 Å and c = 3.186 Å. The facets of the nanorods were parallel to the {110} planes and the growth direction of the nanorod is determined to be [110]. It is known that the growth habit of crystals is related to the relative growth rate of various crystal faces bounding the crystal, which is mainly determined by the internal structure of a given crystal as well as is affected by growth conditions. For a crystal with an anisotropic crystallographic structure, the direction of the crystal face with the corner of the coordination polyhedron occurring at the interface possesses fast growth rate, and the directions of the crystal face with the edge and with the face of the coordination polyhedron occurring at the interface have the second fastest and the slowest growth rates, respectively [113]. SnO_2 crystallizes in point group symmetry 4/mmm and space group $P4_2/mnm$ (D_{4h}^{14}) with Sn and O in 2a and 4f positions, respectively. The low index (110) face of SnO_2 is the thermodynamically most-stable bulk termination [114-116] and has the lowest surface energy [117,118]. The sequence of surface energy per crystal face is (110) < (100) < (101) << (001) [97]. Besides the great stability of (110) faces, it has been demonstrated that this surface provides the best efficiency for the chemisorption and dissociation of oxygenated compounds at the SnO_2 interface owing to the lowest interatomic distances between tin atoms as compared to (101) and (111) faces [97,119].

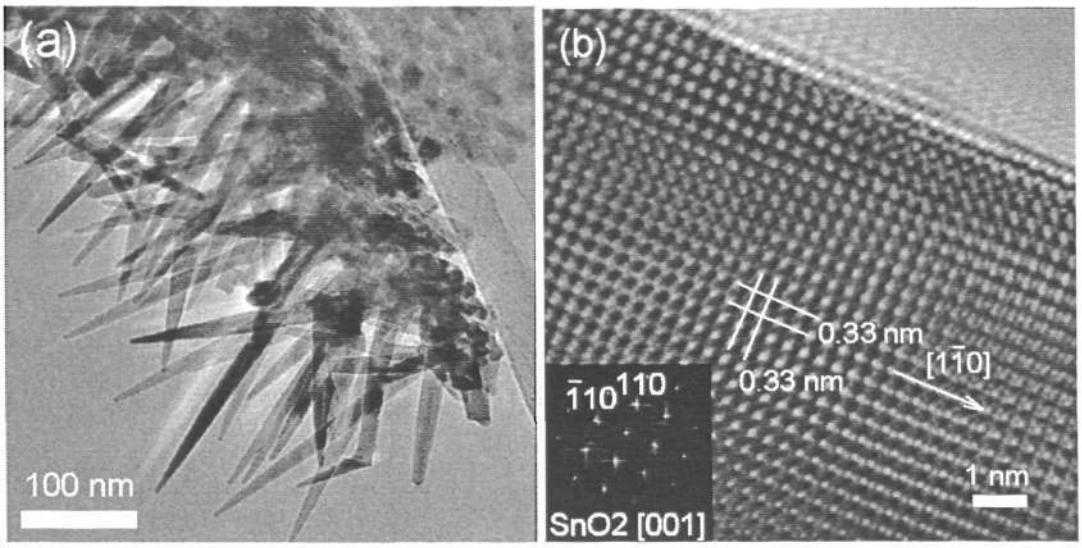

Figure 6-5 (a) Bright field TEM image of SnO_2 nanorods array and (b) HRTEM image the SnO_2 nanorod (inset is FFT of the HRTEM image).

The direct one-step deposition of SnO_2 nanorods array using the ICP-CVD system can be classified as quasi 1-D (Q1D) nanostructures that are grown by catalyst-free synthesis. Such a self-organization process is referred to as a "vapor-solid" (VS) mechanism. In this process, the vapor generated by evaporation, chemical reduction or gaseous reaction is transported and deposited onto a substrate to form Q1D nanostructure [120,121]. The initially deposited molecules formed seed crystals serving as the nucleation sites. As a result, they facilitated directional growth to minimize the surface energy [19]. In many cases, the VS growth process works in an analogous way to the "vapor-liquid-solid" (VLS) mechanism, differing in that one component of the gaseous atoms in VS process might play the role of the catalyst itself [122]. It was proposed that minimization of surface free energy primarily governed the VS process [123,124].

The various deposition durations was carried out to depict the various growth stages of the nanorods by VS mechanism. The deposition duration has been varied from 20 to

120 minutes for SnO_2 nanorods deposited at D_{sn} = 12 cm with a RF power of 1200 W. Figure 6-6 shows the SEM images of the SnO_2 nanorods deposited for (a) 20 min, (b) 40 min, (c) 60 min, (d) 80 min, and (e) 120 min. At the early stage of growth within 20 min, a seed layer of polycrystalline SnO_2 grains serving as the nucleation sites for subsequent nanorods growth was observed as shown in figure 6-6(a). With the increase in deposition duration as captured in figures 6-6(b)-(e), the nanorods were formed and grew longer along their preferred growth orientation forming uniformly distributed nanorods array.

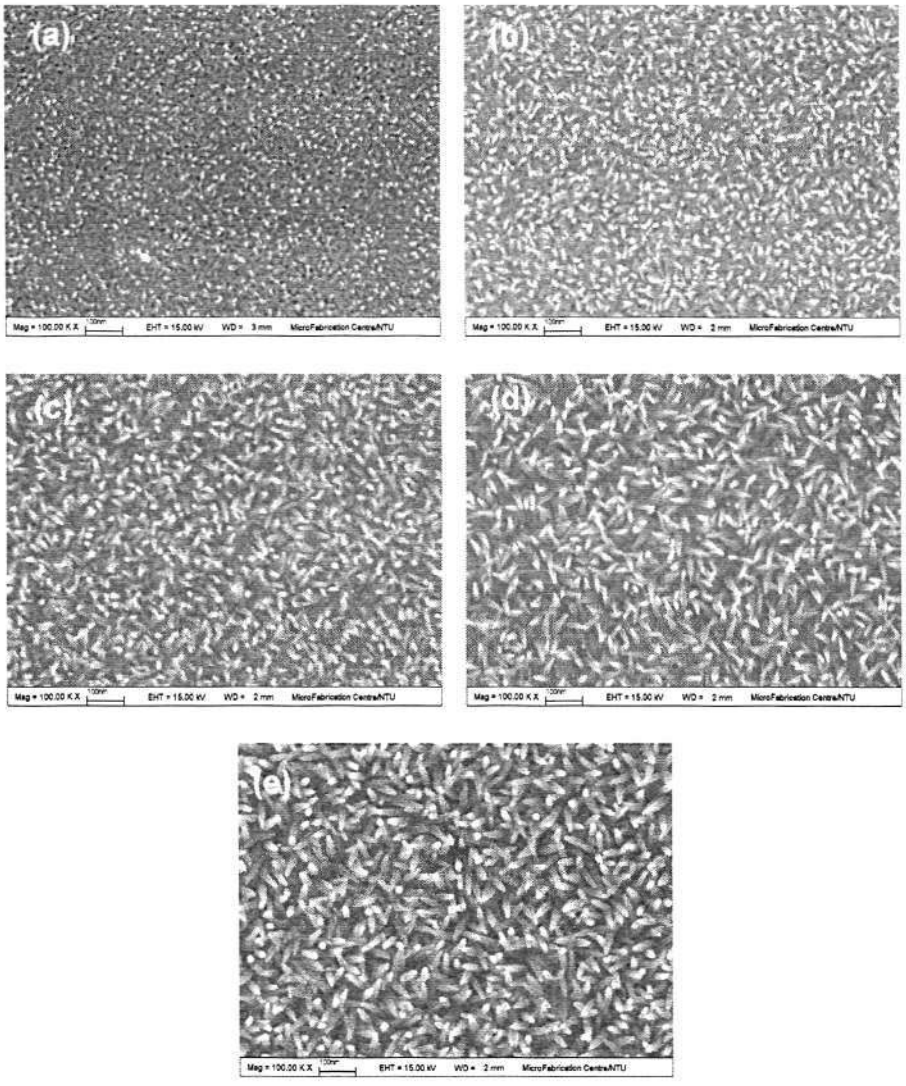

Figure 6-6 SEM images of the SnO_2 nanorods deposited at *Dsn* = 12 cm with RF power of 1200 W for (a) 20 min, (b) 40 min, (c) 60 min, (d) 80 min, and (e) 120 min.

6.2.5 Gas sensing properties

The gas sensing properties of as-deposited SnO_2 nanorods array to CO and H_2 have been studied. The nanorods array is anticipated to deliver enhanced gas sensing sensitivity due to the large surface area similar to the SnO_2 nanorod thin films presented in chapter five. Figure 6-7 shows the gas sensitivity of the as-deposited SnO_2 nanorods array to 1000 ppm CO and H_2 in air as a function of operating temperature. For CO and H_2 detection, no optimal operating temperature was found for the range of operating temperatures from 150 – 450 °C. The highest sensitivity was 10.7 and 4.5 at 450 °C for both H_2 and CO gas respectively.

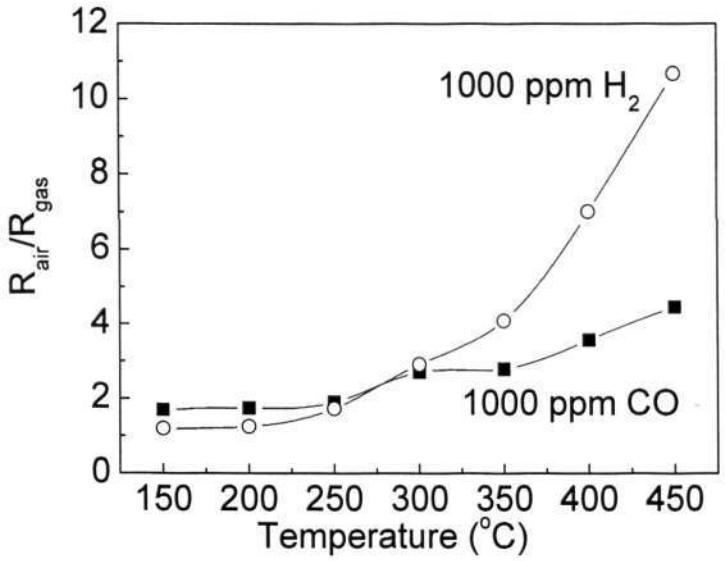

Figure 6-7 CO and H_2 gas sensitivity vs. operating temperature of the as-deposited SnO_2 nanorods array.

6.2.5.1 Surface doping with Pd

Surface modification and microstructure optimization of SnO_2-based sensor materials have been demonstrated to be an effective way to obtain high gas sensitivity and selectivity [90,91,93]. The addition of some foreign metal have been shown to

improve the detection of various kinds of gases by enhancing the sensitivity and reducing the optimum operating temperature. In this investigation, 2 nm Pd clusters were deposited on the SnO_2 nanorod arrays by electron beam evaporation of Pd metal. Figure 6-8(a) shows the evenly distributed Pd nanoparticles on the surface of SnO_2 nanorod arrays. The Pd nanoparticles are hemisphere-shaped with a diameter between 2 – 6 nm as shown in figure 6-8(b).

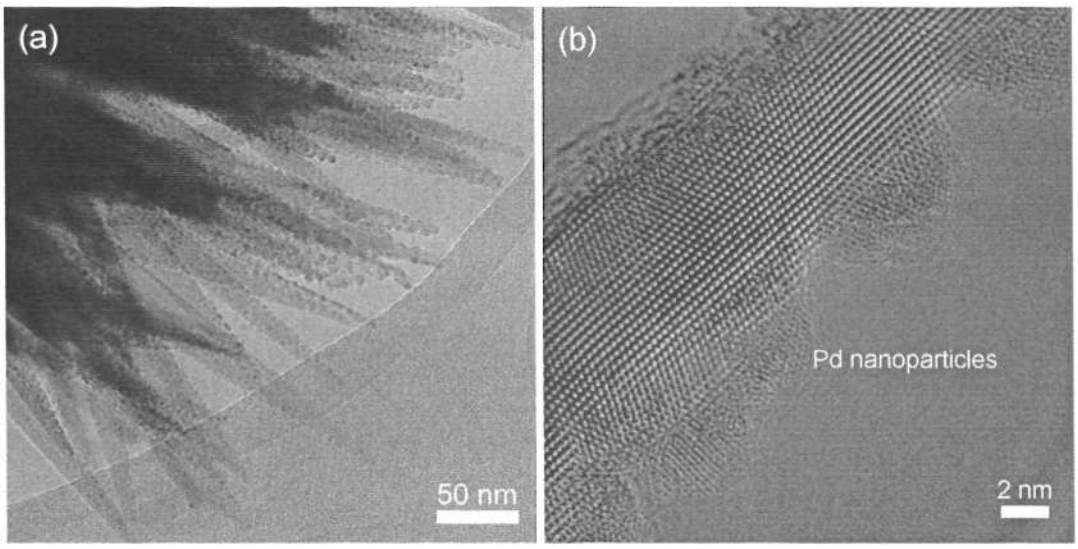

Figure 6-8 (a) Bright filed TEM image and (b) HRTEM image of the Pd-doped SnO_2 nanorods.

Figure 6-9 shows the gas sensitivity vs. operating temperature of the Pd-doped SnO_2 nanorods array. Obviously, samples with Pd doping always have higher sensitivity than those without doping. For pristine SnO_2 nanorods arrays, the sensitivity increases with the elevated operating temperature and no maximum sensitivity is observed for operating temperature up to 450 °C. The optimal temperature for CO detection shifts to 400 °C with sensitivity increase of about threefold after Pd doping. While for the H_2 gas, the optimal temperature of H_2 shifts to 400 °C and the sensitivity is about 6 times better than that of pristine sample. It shows that Pd doping is an effective way to

improve the gas sensitivity and selectivity of H_2. Both chemical and electronic sensitizations are believed to have contributed to the enhanced sensing performance to H_2, similar to the depiction of Pd-doped SnO_2 nanorods thin film in chapter five.

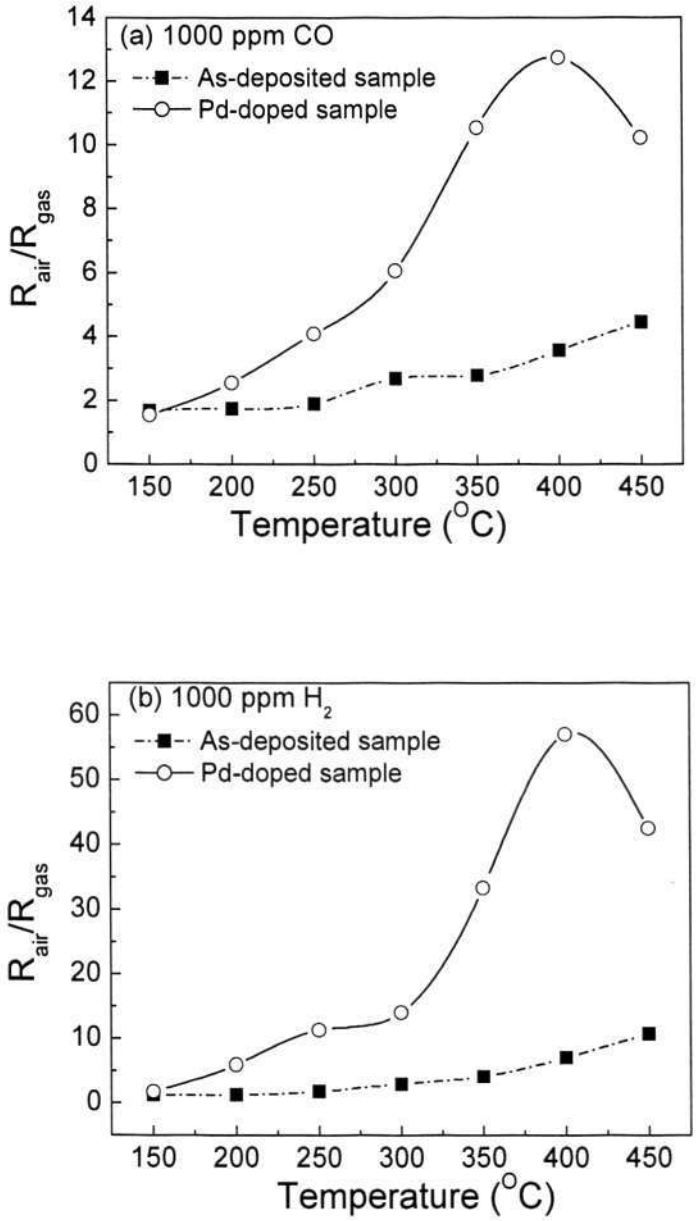

Figure 6-9 (a) CO and (b) H_2 gas sensitivity vs. operating temperature of the as-deposited and Pd-doped SnO_2 nanorods array.

6.2.5.2 Oxygen vacancies effect

The electrical conductivity of conductance-type SnO_2 gas sensor arises primarily from the presence of oxygen vacancies that act as electron donors in the natural non-stoichiometric SnO_2 material. Oxygen vacancies in the SnO_2 material, and hence its stoichiometry can be altered through exposure to oxidizing or reducing ambient at elevated temperature. For the as-deposited SnO_2 nanorods array, annealing in air ambient has been carried out with the aim to investigate the effect of oxygen vacancies on the gas sensing properties.

The as-deposited SnO_2 nanorods array was subjected to post thermal annealing in air for 2 hours at 600 °C, 800 °C, and 1000 °C. Figure 6-10 shows the SEM micrographs of plane view and cross-sectional view of (a) as-deposited SnO_2 nanorods array post annealed at (b) 600 °C, (c) 800 °C, and (d) 1000 °C. Annealing promotes grain growth and the diameter of the SnO_2 nanorods was found to increase along with the higher annealing temperatures.

The gas sensing properties of the as-deposited and post annealed SnO_2 nanorods array were compared. Shown in figure 6-11 is the CO and H_2 sensitivity vs. operating temperature of the as-deposited and post annealed SnO_2 nanorods array at 600 °C, 800 °C, and 1000 °C. Compared to the as-deposited nanorods array, all the post annealed sensors showed better sensitivity to both CO and H_2. The nanorods array annealed at 600 °C showed the highest sensitivity among the tested sensors, together with a reduction of optimal operating temperature in both CO and H_2 detection.

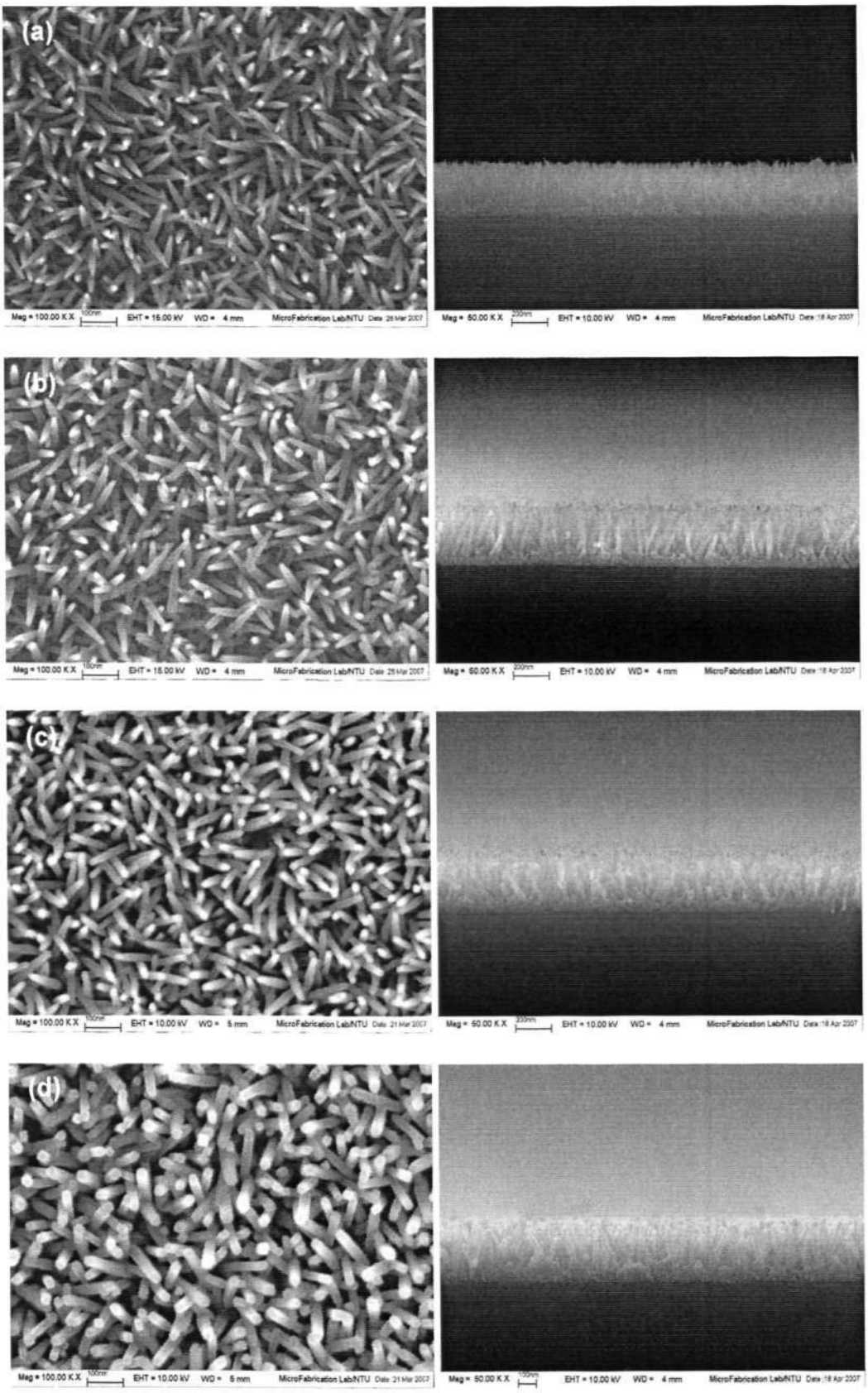

Figure 6-10 SEM micrographs of the plane view and cross-sectional view of (a) as-deposited SnO_2 nanorods array post annealed at (b) 600 °C, (c) 800 °C, and (d) 1000 °C.

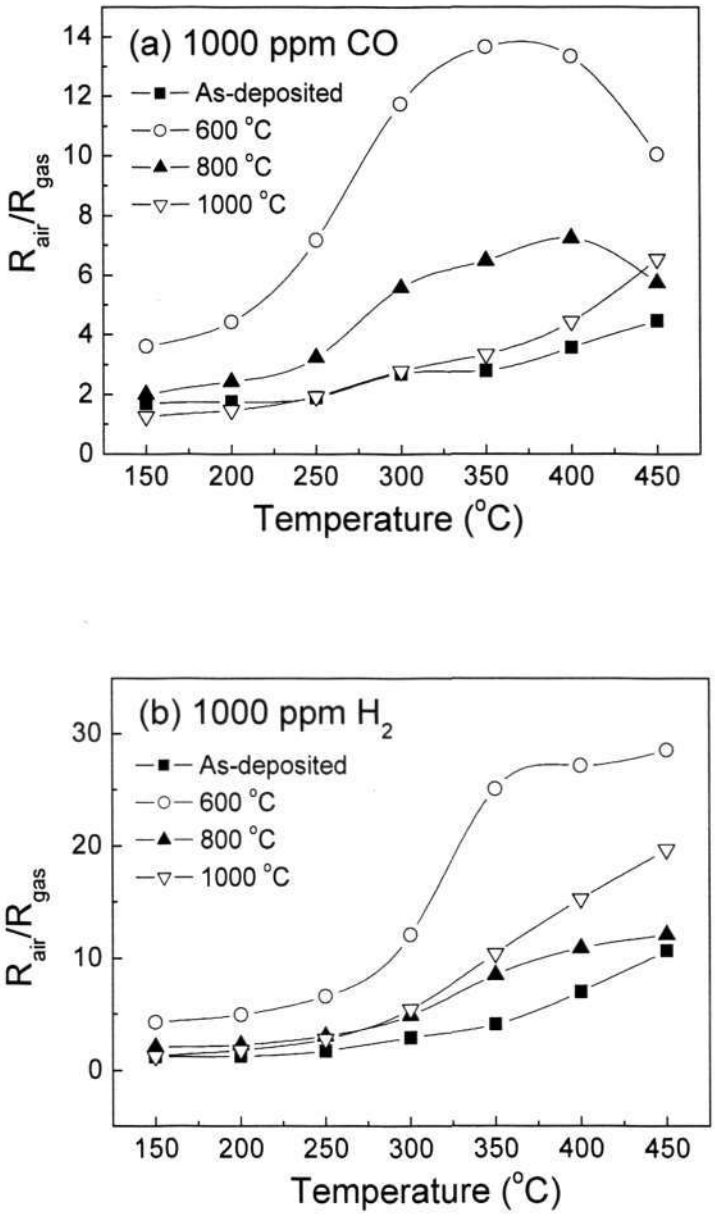

Figure 6-11 (a) CO and (b) H_2 sensitivity vs. operating temperature of the as-deposited and post annealed SnO_2 nanorods array at 600 °C, 800 °C, and 1000 °C.

The XPS characterization was performed to analyze any core level shift of peak binding energy and to determine the stoichiometry of the SnO_2 nanorods array annealed at different temperatures. Figure 6-12 shows the survey spectrum of the as-

deposited SnO_2 nanorods array. The XPS spectrum exhibits a good purity where only Sn and O related core levels are detected apart from the C 1s peak. Figure 6-13 shows the set of corresponding XPS spectra of both O 1s and Sn 3d for (a) as-deposited SnO_2 nanorods array post annealed at (b) 600 °C, (c) 800 °C, and (d) 1000 °C. The binding energy scale was referenced to C 1s level at 285.0 eV, for carbon contamination at the surface. No evident shift of binding energy was observed for both O 1s and Sn 3d core levels after post annealing at different temperatures.

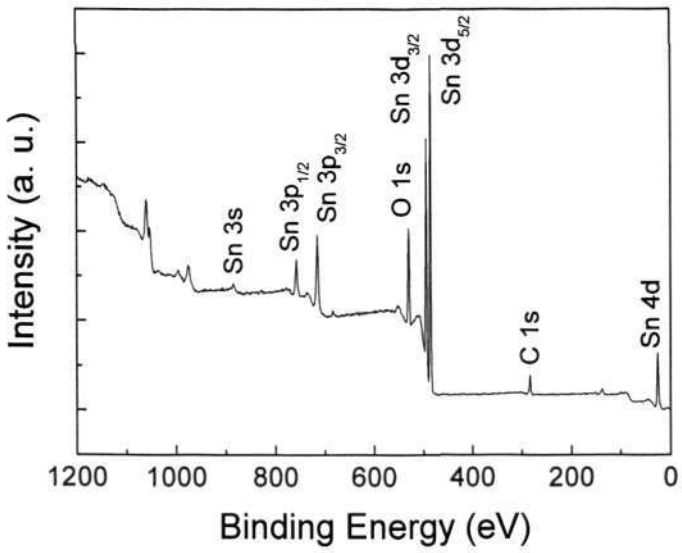

Figure 6-12 XPS survey spectrum of as-deposited SnO_2 nanorods array.

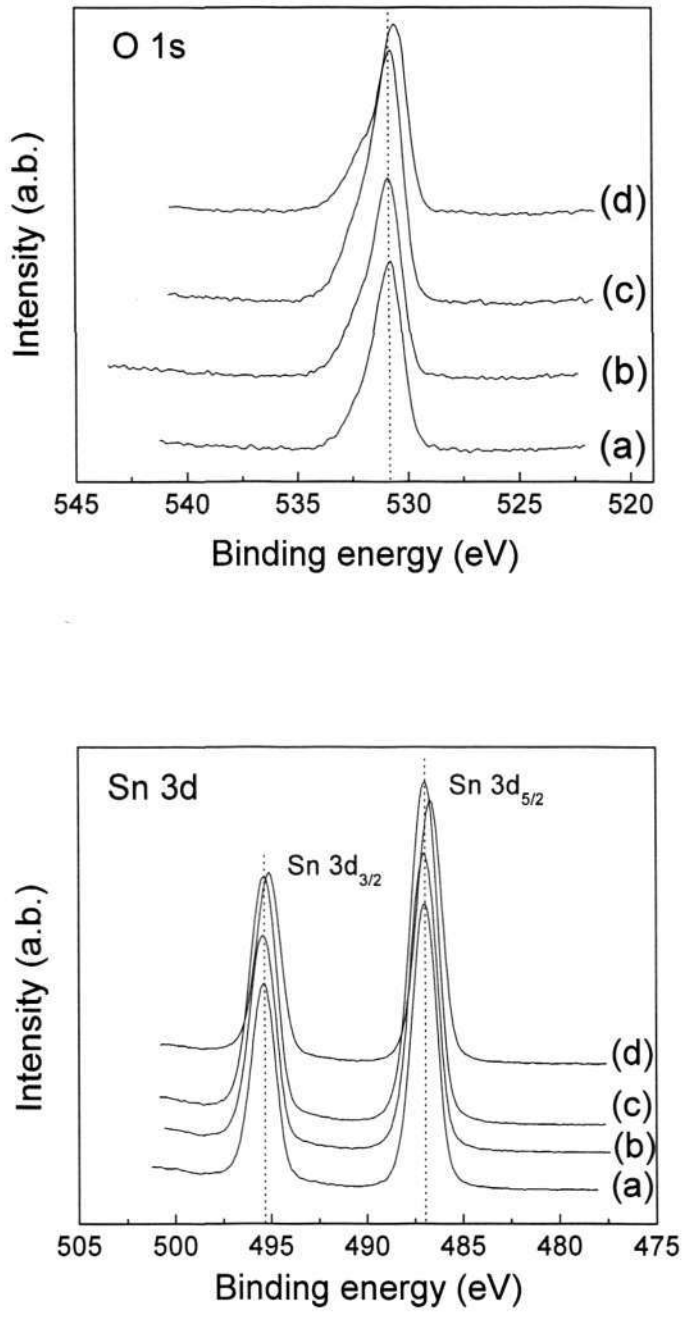

Figure 6-13 XPS spectra of (a) as-deposited SnO_2 nanorods array post annealed at (b) 600 °C, (c) 800 °C, and (d) 1000 °C.

Figure 6-14 shows the O 1s line of the as-deposited SnO_2 nanorods array. A simple visual shape analysis indicates that it is wide, asymmetrical and exhibits a shoulder at

the high binding energy side of the spectrum. This suggests that it is built up of a mixture of two components and can be deconvoluted to obtain the constituting components. The main component located at binding energy (BE) about 530.7 eV corresponds to the O–Sn^{4+} bonding, as taken from the NIST database [125]. The other component of BE at about 531.6 eV is attributed to the oxygen impurities other than the lattice oxygen. Although many types of oxygen impurities can be considered from the physically adsorbed molecules to the chemisorbed species such as O_2^-, O^- and O^{2-} [126], it is considered that negatively-charged oxygen impurities, or the chemisorbed species are the more probable components considering the BE value between the lattice oxygen and oxygen molecule (543.1 eV) [127].

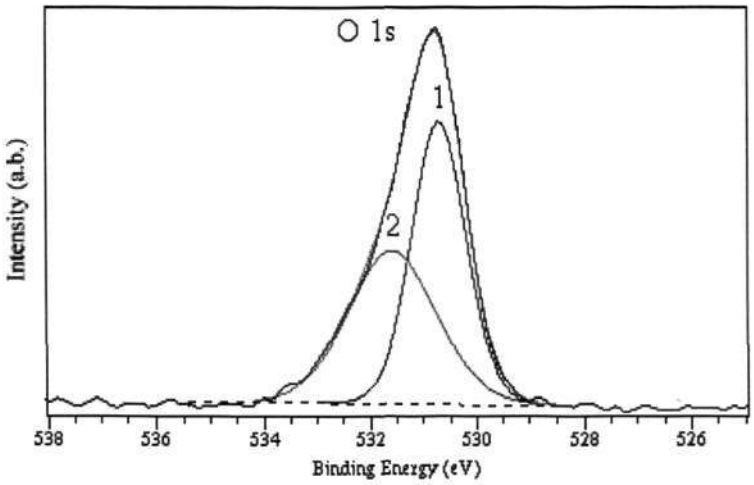

Figure 6-14 O 1s XPS spectrum of as-deposited SnO_2 nanorods array fitted with two simulation peaks. Peak (1) represents the oxygen of the SnO_2 lattice (O-Sn^{4+}) and peak (2) represents chemisorbed oxygen species.

For the SnO_2 nanorods array post annealed at 600 °C, the visual shape analysis of the O 1s line as shown in figure 6-15 indicates a similar characteristic compared to that of as-deposited nanorods array. The O 1s line deconvolution result showed that the main component with BE at 530.8 eV corresponds to the O-Sn^{4+} bonding while the other

component with BE at 532.2 eV belongs to the chemisorbed oxygen species. The deconvolution of O 1s line for SnO_2 nanorods array annealed at other temperatures showed a mixture of the two components identical to the as-deposited and post annealed SnO_2 nanorods array at 600 °C.

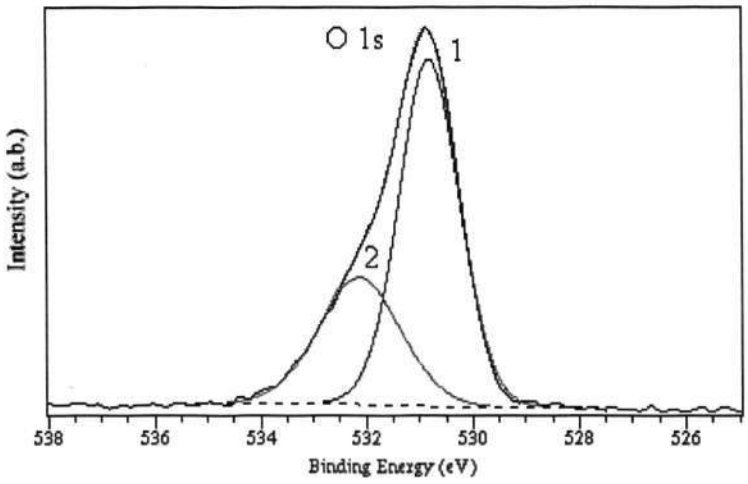

Figure 6-15 O 1s XPS spectrum of the SnO_2 nanorods array post annealed at 600 °C fitted with two simulation peaks. Peak (1) represents the oxygen of the SnO_2 lattice ($O\text{-}Sn^{4+}$) and peak (2) represents chemisorbed oxygen species.

The stoichiometry of the as-deposited and post annealed SnO_2 nanorods array, defined as the relative integrated intensity of $O\text{-}Sn^{4+}$ component (denoted at $O_{lattice}$) and Sn 3d XPS peaks is shown in table 6-1. The relative concentration of the $[O_{total}]/[Sn]$ that takes into account the chemisorbed species is also shown in the table. The thermal annealing in air ambient has increased the overall oxygen concentration $[O_{total}]$ of the as-deposited SnO_2 nanorods array. According to Chiu and co workers [128], the higher ratio of oxygen of the thermally treated SnO_2 suggests that more oxygen species existed as lattice oxygen in the metal oxide or as surface-adsorbed oxygen. Therefore, more electrons produced from the defect reactions increased the conductivity of the

thermally treated SnO_2 upon exposure to reducing gas, thus gave rise to a higher sensitivity. However, our results showed that the highest gas sensitivity came from SnO_2 nanorods array post annealed at 600 °C (figure 6-11) which does not have the highest $[O_{total}]/[Sn]$ compared to other nanorods arrays (table 6-1).

SnO_2 nanorods array	Relative concentration $[O_{lattice}]/[Sn]$	Relative concentration $[O_{total}]/[Sn]$
As-deposited	0.99	1.86
Annealed at 600 °C	1.41	2.10
Annealed at 800 °C	1.31	2.15
Annealed at 1000 °C	1.30	2.24

Table 6-1 The relative concentration $[O_{lattice}]/[Sn]$ and $[O_{total}]/[Sn]$ for different SnO_2 nanorods arrays.

It has been reported the SnO_{2-x} thin films with a low value of x have a high sensitivity compared to those with a high x value because there is more Sn^{4+} that can be reduced to Sn^{2+} by reducing gases [129,130]. The more stoichiometric SnO_2 is therefore anticipated to deliver a high gas response to reducing gases. In this context, the SnO_2 nanorods array post annealed at 600 °C with the highest $[O_{lattice}]/[Sn]$ ratio have shown the highest sensitivity to CO and H_2 among the as-deposited and post annealed SnO_2 nanorods array (figure 6-11).

The gas sensitivity of SnO_2 is originated from the electron transfer between SnO_2 and gases absorbed on its surface. SnO_2 is an n-type semiconductor because it virtually contains oxygen vacancies. Physisorbed oxygen on the SnO_2 surface accepts electrons from SnO_2 to form chemisorbed oxygen, $O_{2,ads}^-$ or O_{ads}^-, thereby inducing a depletion region in SnO_2. In an atmosphere containing reducing gas, chemisorbed oxygen ions

react with the reducing gas and release electrons into the conduction band of SnO_2, consequently increasing its conductivity [131,132]. The electron capture and release reactions can be written as follow:

Electron capture: $\frac{1}{2} O_{2\,(gas)} + e^- \rightarrow O_{ads}^-$ (6-1)

Electron release: $H_{2\,(gas)} + O_{ads}^- \rightarrow H_2O_{\,(gas)} + e^-$ (6-2)

These two processes may involve oxygen vacancy and lattice oxygen with the sensing material [133,134]. The required reactions are shown as follows:

$$\frac{1}{2} O_{2\,(gas)} + e^- \rightarrow O_{ads}^- \quad (6\text{-}3)$$

$$V_o^{\bullet\bullet} + O_{ads}^- + e^- \rightarrow O_o^x \quad (6\text{-}4)$$

$$H_{2\,(gas)} \rightarrow H_{2\,ads} \quad (6\text{-}5)$$

$$H_{2\,ads} + O_o^x \rightarrow H_2O_{(gas)} + V_o^{\bullet\bullet} + 2e^- \quad (6\text{-}6)$$

where $V_o^{\bullet\bullet}$ represents an oxygen vacancy and O_o^x represents an O^{2-} ion occupying the regular oxygen lattice site. A reduction in oxygen vacancies will drive equation (6-6) in the forward direction, which will lower the resistance measured in H_2 containing ambient (R_{gas}) and improve the gas sensitivity. However, low oxygen vacancies will also retard the conversion of O_{ads}^- to O_o^x (equation (6-4)) and consequently slowdown the forward reaction shown by equation (6-6). Therefore, an optimal oxygen vacancy concentration is required for the two reactions to be in equilibrium [135]. In our case, the SnO_2 nanorods array post annealed at 600 °C with the highest $[O_{lattice}]/[Sn]$ ratio possessed the optimal oxygen vacancy concentration and thus gave the highest sensitivity compared to other nanorods arrays. Since the atomic concentrations calculated from XPS spectra are not absolutely precise, the exact amount of oxygen vacancies for achieving the best sensitivity still needs further investigation.

Besides thermal annealing, the as-deposited SnO_2 nanorods arrays were subjected to O_2 plasma treatment using the same ICP-CVD setup. Plasma treatment is a very effective technology in surface modification for a variety of materials. Plasma containing electrons, ions, radicals, and neutral molecules strongly interacts with surfaces, and as a result, chemical and physical modifications occur on the surfaces [136]. Kim and co workers used a plasma treatment technique to reduce surface defects such as oxygen vacancies on TiO_2 surfaces [137]. They investigated the influence of different gas plasma treatments of TiO_2 film on the photoelectric performance of dye-sensitized solar cells (DSSCs). Liu and co workers applied O_2 plasma treatment to suppress the chemisorption sites, primarily the oxygen deficiency sites on surface and also the oxygen vacancies in ZnO, which results in enhancement of the UV detection properties [138].

The as-deposited SnO_2 nanorods array was subjected to 1200 W O_2 plasma treatment for 20 min, 40 min and 120 min respectively. Figure 6-16 shows the SEM micrographs of the (a) as-deposited SnO_2 nanorods array post O_2 plasma treated for (b) 20 min, (c) 40 min, and (d) 120 min. No notable changes on microstructures were observed after O_2 plasma treatment, which could possibly attributed to the weak sputtering strength of pure O_2 plasma as discussed in chapter five. The preserved nanorods array structure is desired as our aim is to study the possibility of chemical modification on oxygen vacancies by using O_2 plasma treatment.

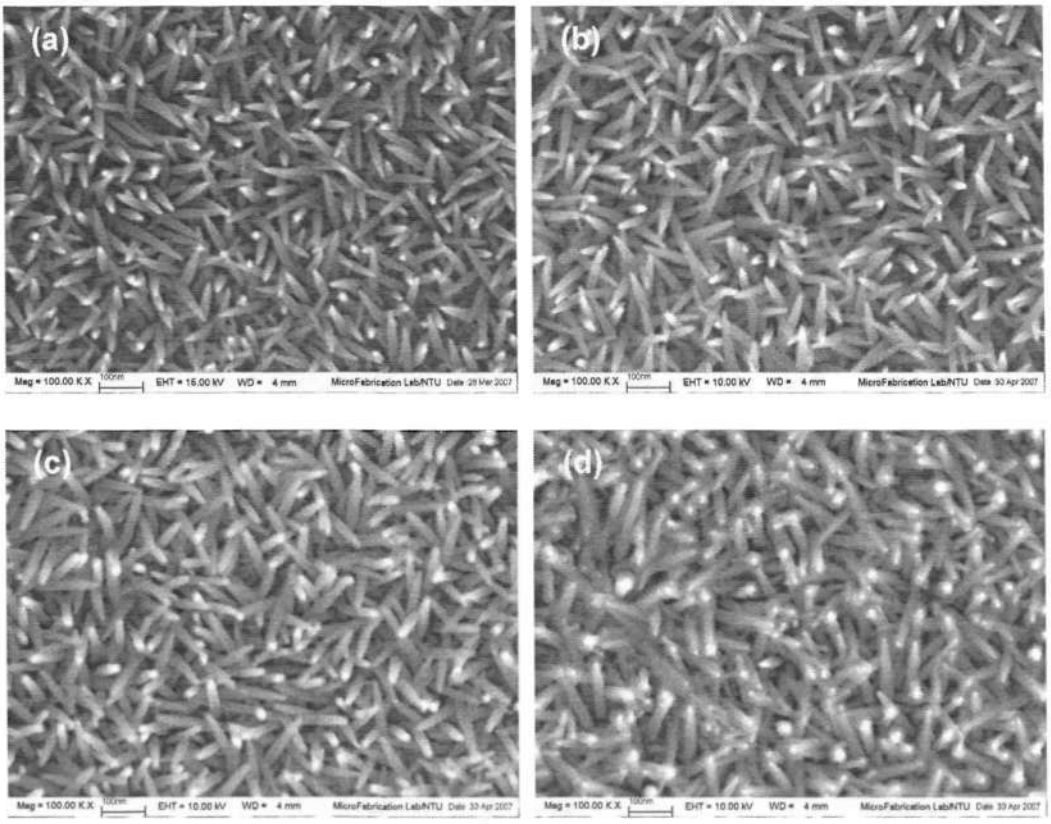

Figure 6-16 SEM micrographs of the (a) as-deposited SnO_2 nanorods array post O_2 plasma treated for (b) 20 min, (c) 40 min, and (d) 120 min.

Figure 6-17 shows the CO and H_2 sensitivity vs. operating temperatures of the as-deposited and post O_2 plasma treated SnO_2 nanorods array for 20 min, 40 min and 120 min. The post O_2 plasma treated SnO_2 nanorods array showed improved gas sensitivity compared to the as-deposited nanorods array. The highest sensitivity to CO and H_2 was observed for SnO_2 nanorods array treated in O_2 plasma for 40 min. The highest sensitivity value obtained in the range of investigated operating temperature was better compared to SnO_2 nanorods array post annealed at 600 °C shown in figure 6-11.

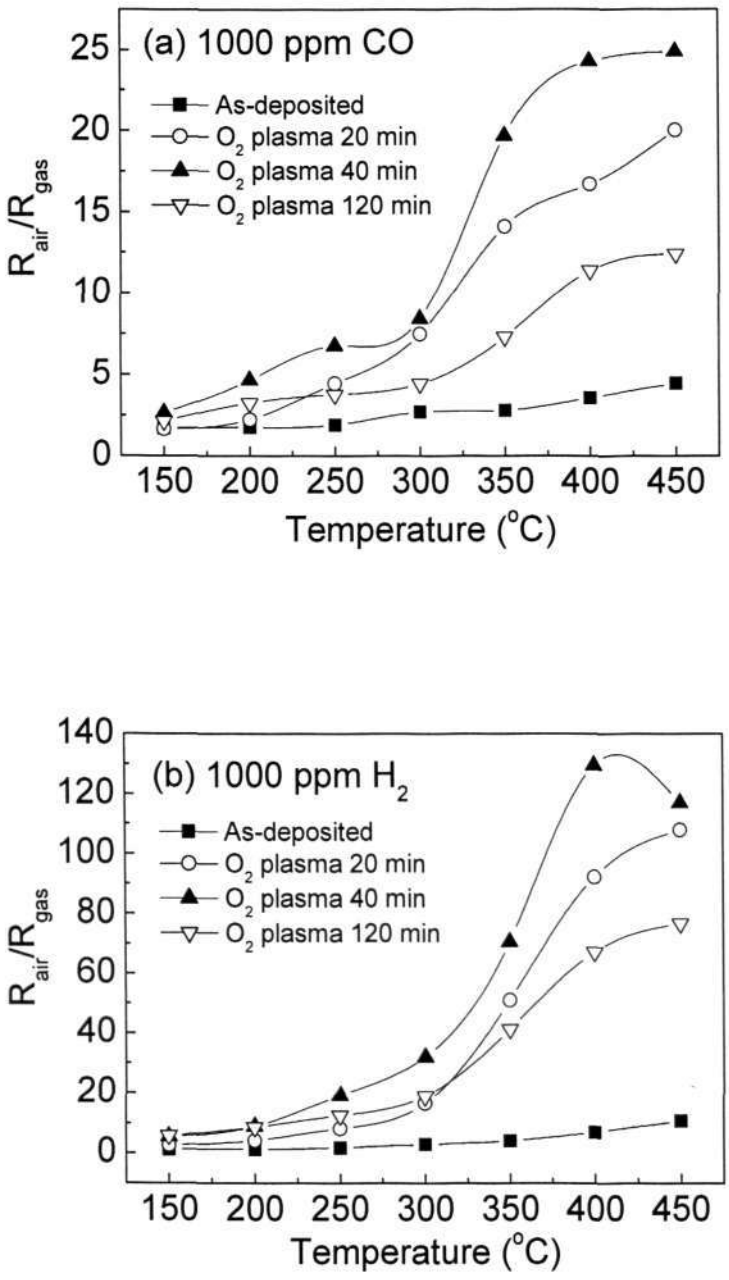

Figure 6-17 (a) CO and (b) H_2 vs. operating temperatures of the as-deposited and post O_2 plasma treated SnO_2 nanorods array for 20 min, 40 min, and 120 min.

Figure 6-18 shows the XPS spectra of both O 1s and Sn 3d for (a) as-deposited SnO_2 nanorods array post O_2 plasma treated for (b) 20 min, (c) 40 min, and (d) 120 min. The

binding energy scale was referenced to C 1s level at 285.0 eV, for carbon contamination at the surface. In the O 1s XPS spectra, the SnO_2 nanorods array treated in O_2 plasma for 20 min and 40 min shows an evident mixture of 2 peak components of equally strong intensity. For the SnO_2 nanorods array treated in O_2 plasma for 120 min, there exists a shift by approximately 2 eV towards the higher binding energy compared to the nanorods array without post plasma treatment. In the Sn 3d spectra, an evident shift of approximately 2.4 eV towards the higher binding energy is observed for SnO_2 nanorods array treated in O_2 plasma for 120 min while no apparent shift is noted for the SnO_2 nanorods array treated in O_2 plasma for 20 min and 40 min compared to the as-deposited nanorods array without post O_2 plasma treatment.

The deconvolution results of O 1s line of the SnO_2 nanorods array post treated in O_2 plasma for (a) 20 min, (b) 40 min, and (c) 120 min are shown in figure 6-19. In figures 6-19(a) and 6-19(b), the component labeled as peak '1' is located at BE of 530.8 eV, which corresponds to the $O–Sn^{4+}$ bonding, taken from the NIST database [125]. The prominent peak '2' component with BE of 532.4 eV could be attributed to the chemisorbed oxygen species. In figure 6-19(c), the decomposition procedure of O 1s line shows two peaks located at BE of 532.7 eV and 534.2 eV respectively. The peak labeled '1' could be assigned to the chemisorbed oxygen species while peak labeled '2' could be related to the O 1s core level of SiO_2 , used as an insulation layer to separate the Si substrate from the SnO_2 nanorods array. The long duration of O_2 plasma treatment seemed to reduce the thickness of Sn layer as evidenced by a great reduction of Sn core level related peaks and the presence of Si peak in the survey spectrum shown in figure 6-20. The detection of Si peak in the survey spectrum leads to the assignation of peak labeled '2' to O 1s core level of SiO_2 in figure 6-19c.

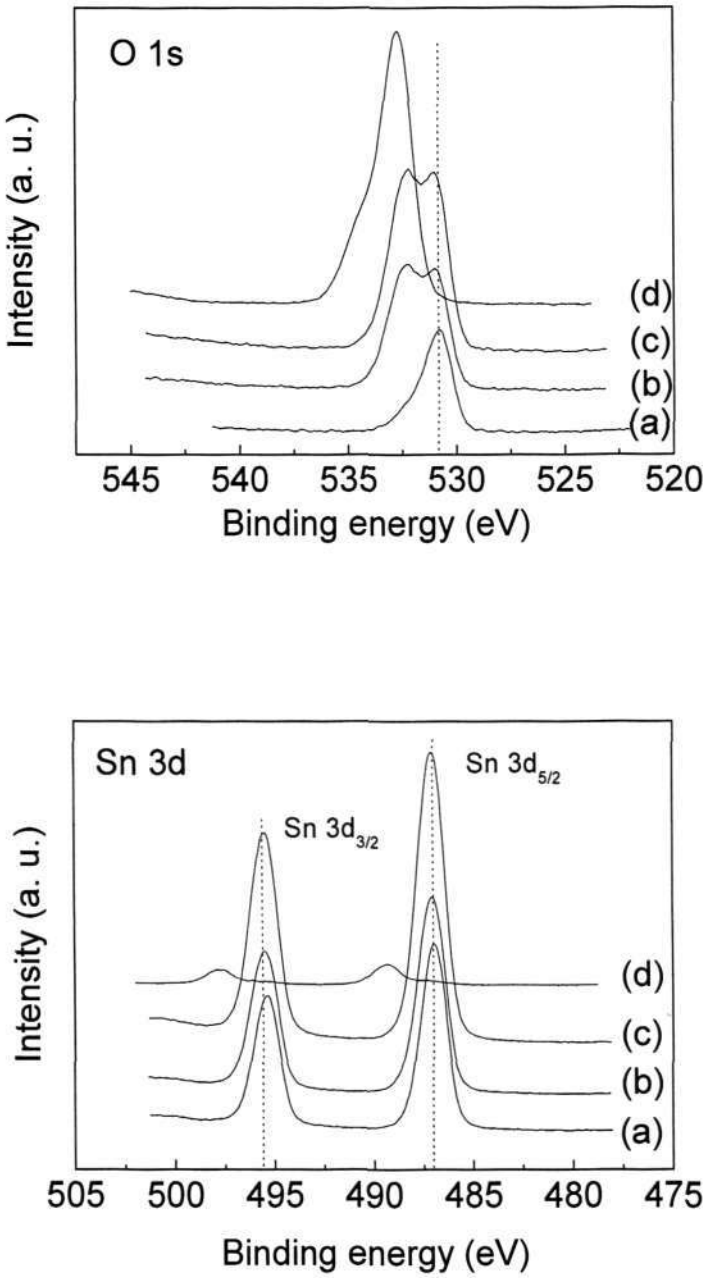

Figure 6-18 XPS spectra of the (a) as-deposited SnO_2 nanorods array post O_2 plasma treated for (b) 20 min, (c) 40 min, and (d) 120 min.

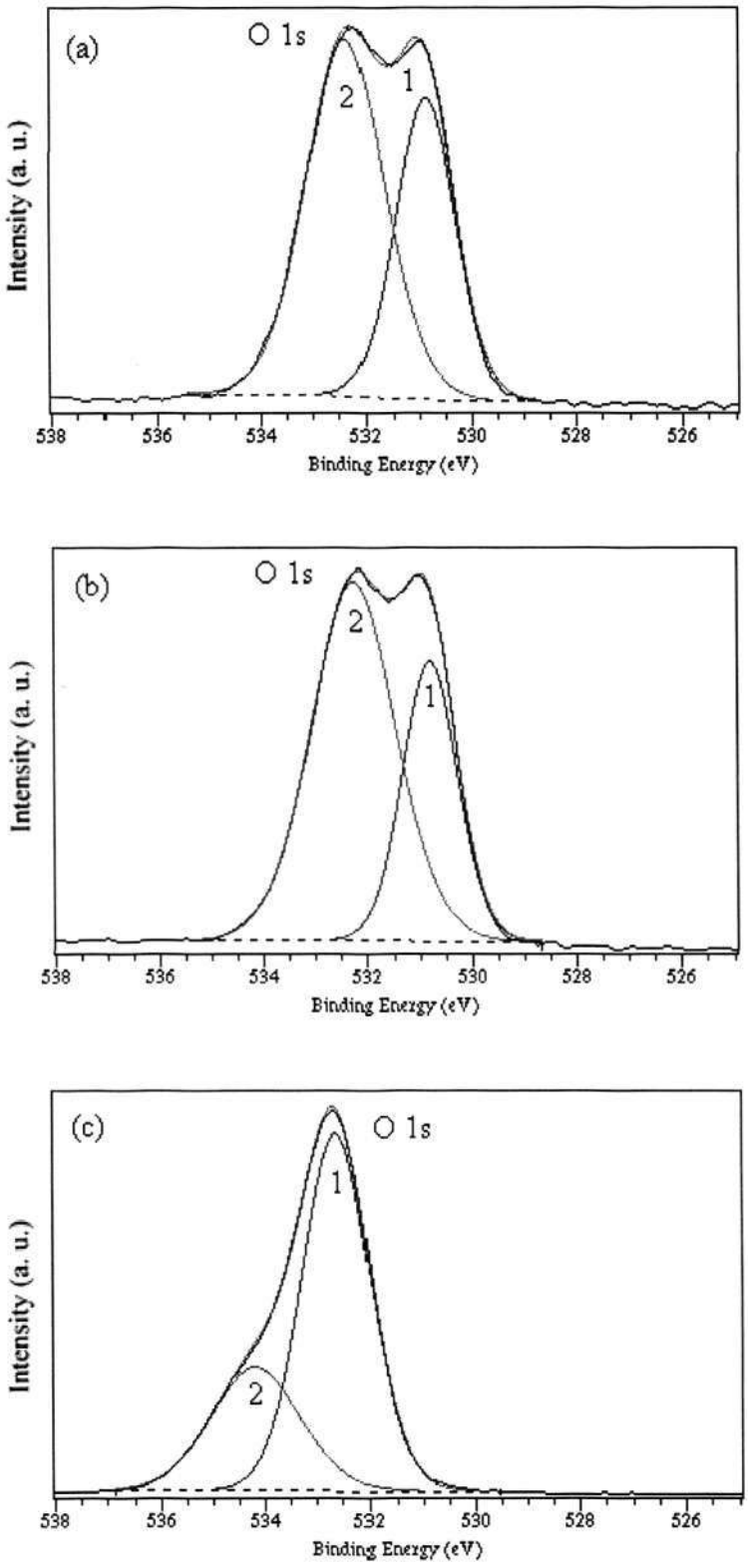

Figure 6-19 O 1s XPS spectra with two decomposited components (peak 1 and 2) of the as-deposited SnO_2 nanorods array post treated in O_2 plasma for (a) 20 min, (b) 40 min, and (c) 120 min.

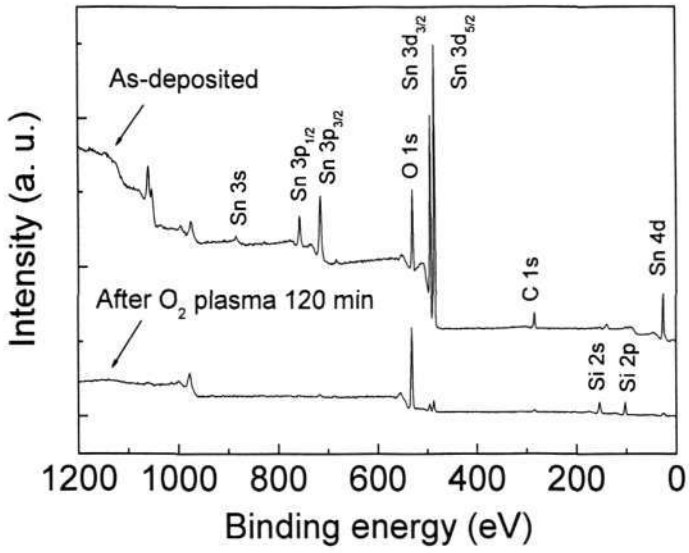

Figure 6-20 XPS survey spectra of as-deposited and post O_2 plasma treated SnO_2 nanorods array for 20 min.

The relative concentration $[O_{lattice}]/[Sn]$ of the SnO_2 nanorods array post treated in O_2 plasma for 20 min and 40 min is 1.40 and 1.18 respectively, which are both higher than the as-deposited SnO_2 nanorods array with a $[O_{lattice}]/[Sn]$ of 0.99. However, the $[O_{lattice}]/[O_{total}]$ ratio indeed decreased with longer duration in O_2 plasma treatment for the SnO_2 nanorods array as shown in table 6-2. Meanwhile, there has been an increase in the concentration of chemisorbed oxygen species $[O_{ads}]$ with the increase of plasma treatment duration. The enhancement in the gas sensitivity of the O_2 plasma treated nanorods array shown in figure 6-17 could be attributed to the presence of high concentration of chemisorbed oxygen species on the surface of the SnO_2 nanorods array. During oxygen plasma treatment, oxygen is added to the SnO_2 nanorods array in the form of chemisorbed oxygen species on the surface rather than into the lattice as in thermal annealing method. Chemisorbed oxygen species can be expected to be more reactive than lattice oxygen [139] and this explains the much better sensitivity

achieved by the O_2 plasma treated SnO_2 nanorods array when compared to the post annealed nanorods array.

		SnO_2 nanorods array					
		As-deposited		O_2 plasma 20 min		O_2 plasma 40 min	
Element		Main peak (eV)	At (%)	Main peak (eV)	At (%)	Main peak (eV)	At (%)
O 1s	O^- (lattice)	530.71	25.85	530.88	23.39	530.85	19.89
	O^- (adsorbed)	531.60	22.73	532.39	36.14	532.31	39.12
$[O_{lattice}]/[O_{total}]$ (%)		53.2		39.3		33.7	
$[O_{ads}]/[O_{total}]$ (%)		46.8		60.7		66.3	

Table 6-2 Average core level BEs and atomic concentrations (At %) of O 1s of as-deposited SnO_2 nanorods array post O_2 plasma treated for different durations.

6.3 SnO_2 nanocolumns array by direct liquid injection ICP-CVD

6.3.1 Experimental details

In this section, the SnO_2 thin films deposited by liquid injection ICP-CVD system will be presented. Dibutyltin diacetate (Aldrich, 98% purity), $(C_4H_9)_2Sn(OOCCH_3)_2$, was dissolved in tetrahydrofuran (THF) and the resulted 0.1 M solution was used as the precursor. The precursor in solution form was delivered into the Lintec vaporizer by high pressure Ar acting as the push gas. The precursor flow rate was controlled at 50 mg/min. The precursor was totally evaporated in the vaporizer held at 150 °C and the vapor was carried into the chamber by 50 sccm Ar gas. 100 sccm O_2 was introduced into the plasma as the reaction gas. No additional heating was applied to the substrate during deposition.

6.3.2 Effect of substrate-nozzle distance D_{sn}

Figure 6-21 show the XRD patterns of the SnO_2 films deposited at a substrate-nozzle distance D_{sn} = (a) 10 cm, (b) 12 cm, (c) 14 cm and (d) 16 cm for 40 minutes. All peaks can be indexed as Cassiterite SnO_2 (PDF 41-1445), and the (101) preferential orientation was observed for the films.

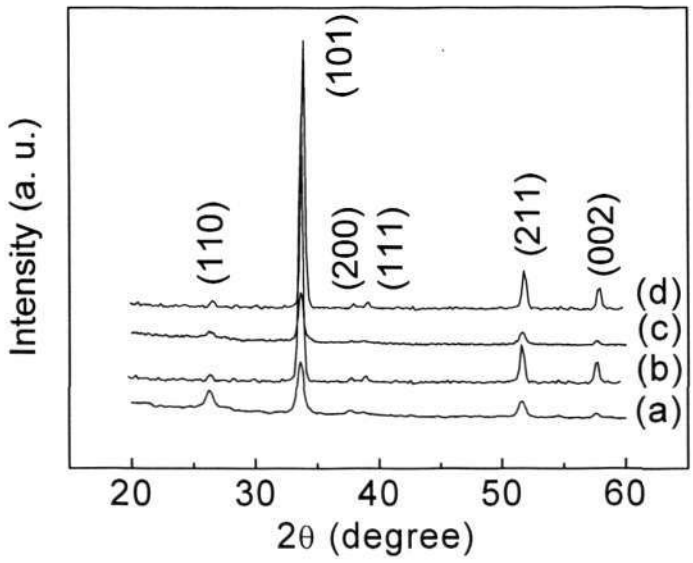

Figure 6-21 XRD patterns of the SnO_2 nanocolumns array deposited at D_{sn} = (a) 10 cm, (b) 12 cm, (c) 14 cm, and (d) 16 cm for 40 min.

Figure 6-22 shows the SEM micrographs of the SnO_2 thin films deposited at D_{sn} = (a) 10 cm, (b) 12 cm, (c) 14 cm and (d) 16 cm for 40 minutes. The grains in the SnO_2 nanocolumns array deposited at 10 cm were rod-like and the grain size was about 45 × 110 nm (figure 6-22(a)). Uniform square rods in the size of 43.5 × 100 nm were observed in the SnO_2 nanocolumns array deposited at 12 cm (figure 6-22(b)). With the D_{sn} increased to 14 cm and 16 cm, the rods shape changed to cylinder and the size of the rods decreased to Ø29 × 70 nm for D_{sn} = 14 cm and Ø17 × 87 nm for D_{sn} = 16 cm respectively (figure 6-22(c) and 6-22(d)). Figure 6-23 shows the effect of the substrate

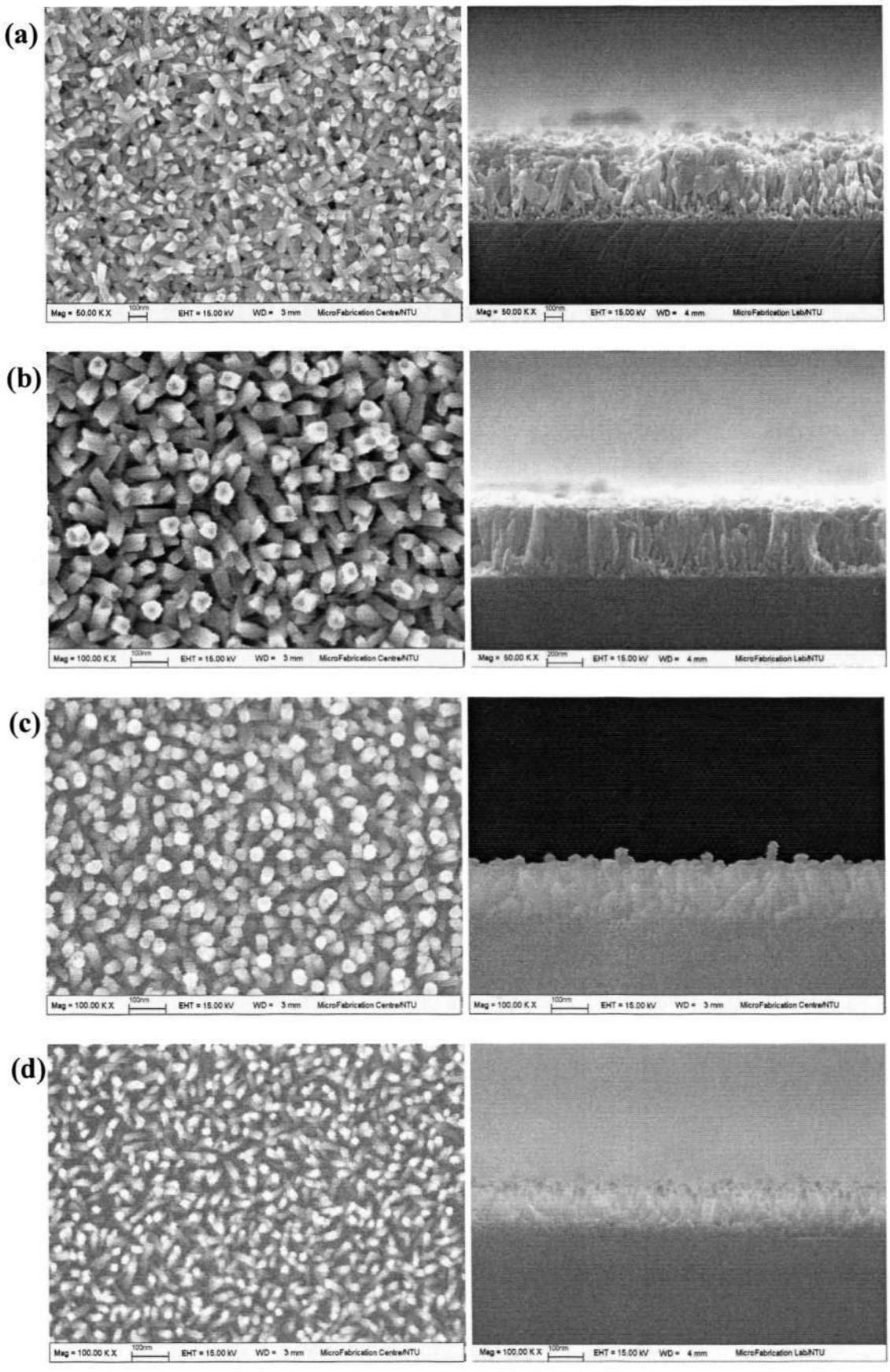

Figure 6-22 SEM micrographs of the SnO_2 nanocolumns array deposited at D_{sn} = (a) 10 cm, (b) 12cm, (c) 14 cm and (d) 16 cm for 40 minutes.

distance on the thickness and grain size of the SnO_2 nanocolumns array. It showed that the SnO_2 nanocolumn thickness and the grain size decreased with the increase of the substrate distance from the nozzle inlet.

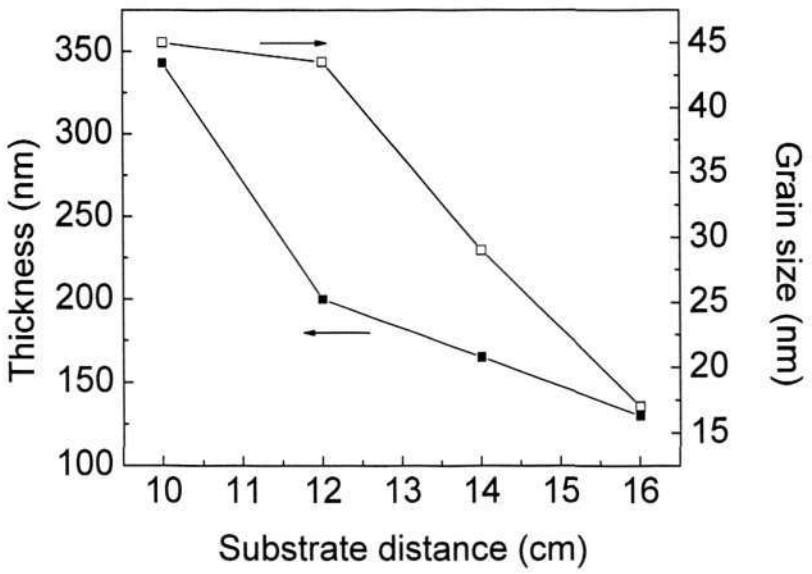

Figure 6-23 Effect of the substrate-nozzle distance D_{sn} on the thickness and grain size of the SnO_2 nanocolumns array.

Figure 6-24(a) shows the TEM image of SnO_2 nanocolumns array deposited at D_{sn} = 12 cm. It revealed the columnar and solid microstructure of the nanocolumns. The clear lattice fringes of HRTEM image of the SnO_2 nanocolumn shown in Figure 6-24(b) indicated a single crystal structure of the nanocolumn. The lattice spacing is 3.1 Å, corresponding to the (001) plane of tetragonal rutile crystal structure of SnO_2.

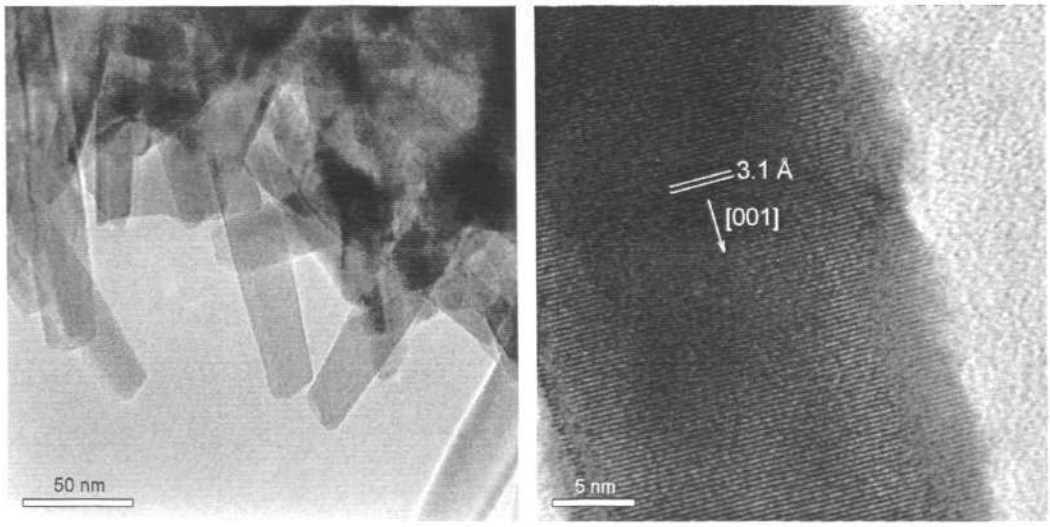

Figure 6-24 (a) TEM and (b) HRTEM images of the SnO_2 nanocolumns deposited at D_{sn} = 12 cm [140].

6.3.3 Gas sensing properties

The gas sensing properties of the SnO_2 nanocolumns array to CO and H_2 were characterized. Figure 6-25 shows the sensing response of the SnO_2 nanocolumns array to 1000 ppm CO and H_2 at increasing operating temperature range of 150 to 450 °C. The as-deposited SnO_2 nanocolumns array show poor response to 1000 ppm CO, while the response to 1000 ppm H_2 is much better. Specifically, the sensitivity to 1000 ppm H_2 at 400 °C is 17, which is 3 times better than that of CO. The sensing performance of the as-deposited SnO_2 nanocolumns array is comparable to that of SnO_2 nanorods array shown in figure 6-7.

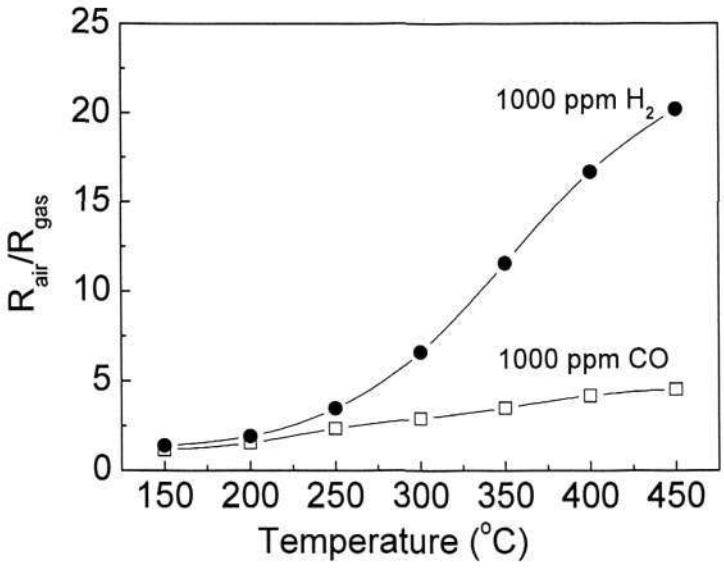

Figure 6-25 CO and H_2 gas sensitivity vs. operating temperature of the as-deposited SnO_2 nanocolumns array.

In the direct liquid injection ICP-CVD process, a lot of solvent vapor was admitted into the plasma together with the precursor vapor. The incomplete decomposition of the organic vapor caused carbon contamination to the deposited arrays. The composition analysis by XPS showed that there are around 7 at% carbon residues in the as-deposited nanocolumns array, which could have contributed to the poor sensing results of the nanocolumns array gas sensor. To verify this, the as-deposited SnO_2 nanocolumns array were post-annealed in air at 600 °C for 2 hours. After annealing, the sensing response of the SnO_2 nanocolumns array to 1000 ppm CO and H_2 increased remarkably. The sensitivity at the optimal operating temperature of 400 °C is 3 times and 2 times better for CO and H_2 respectively as depicted in figure 6-26. The previous results in section 6.2.5.2 also show that gas sensitivity of SnO_2 nanorods array can be greatly enhanced by O_2 plasma treatment. The as-deposited SnO_2 nanocolumns array were also subjected to 1200 W O_2 plasma treatment. After 1200 W

O_2 plasma treatment for 40 min, the sensing response increased dramatically (figure 6-26). The response to both 1000 ppm CO and H_2 increased around 7 times with the sensitivity of the O_2 plasma-treated sample to 1000 ppm H_2 achieving a value of 160.

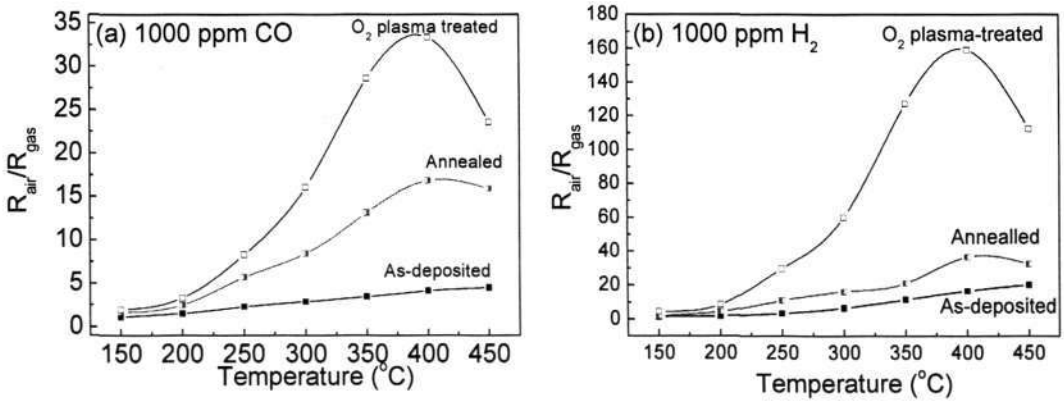

Figure 6-26 Sensing response vs. operating temperature of the SnO_2 nanocolumns array to (a) 1000 ppm CO and (b) 1000 ppm H_2 in air [140].

The sensing response curves of the as-deposited, annealed and plasma-treated nanocolumns array to three successive cycles of step change of 100 ppm H_2 at operating temperature of 400 °C are shown in figure 6-27. All the three nanocolumns array sensors show good repeatability with full recovery in air during the three cycles. The sensitivity of the O_2 plasma-treated nanocolumns is the highest among the three sensors. Furthermore, from the steep changes of the resistance in the response curves shown in figure 6-27, the O_2 plasma-treated nanocolumns possess much shorter response and recovery time as compared to the as-deposited nanocolumns.

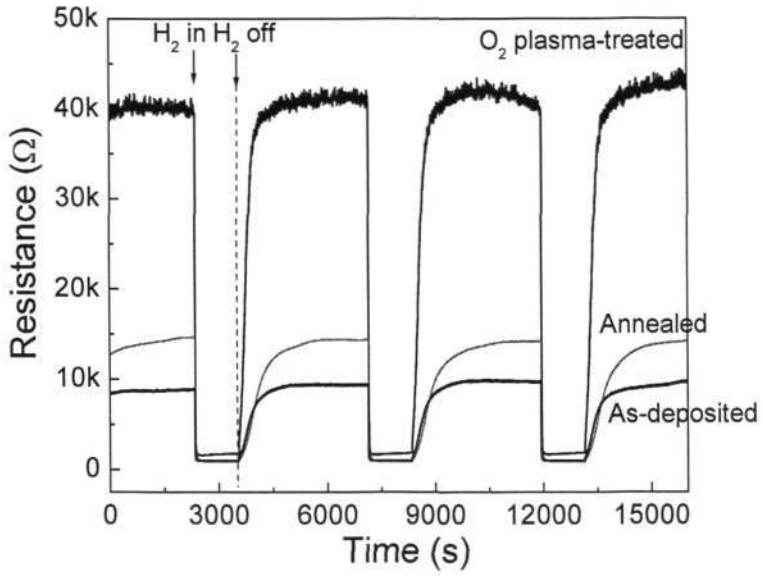

Figure 6-27 Sensing response of the as-deposited, post annealed and O_2 plasma treated nanocolumns array to three successive cycles of step change of 100 ppm H_2 at the operating temperature of 400 °C [140].

These results showed that the sensing performance of the SnO_2 nanocolumn arrays has been remarkably enhanced by post-annealing and especially by O_2 plasma treatment. The improvement of sensing properties is believed to be closely related to the chemical change of the oxygen and Sn in the nanostructures. Therefore, the XPS characterization was carried out to analyze the valence state of O and Sn species in the nanocolumns before and after annealing and O_2 plasma treatment.

Figure 6-28 shows the evolution of the Sn 3d peak and O 1s peak of the as-deposited SnO_2 nanocolumns array, as well as those after annealing at 600 °C in air for 2 hours and 1200 W O_2 plasma treatment for 40 min. The Sn 3d peak shifted continuously towards the lower binding energy for both the annealed and O_2 plasma-treated

nanocolumns in comparison to the as-deposited nanocolumns and the intensity was also found to decrease accordingly (figure 6-28(a)). It is obvious that the O 1s peaks of the O_2 plasma-treated sample contain two peaks: one at a low binding energy of 530.7 eV and the other at a higher binding energy of 532.3 eV. The O 1s peaks of the as-deposited and annealed nanocolumns can also be deconvoluted into two peaks by mixed Lorentzian-Gaussian fitting (figure 6-28(b)). The O 1s peaks centered at lower binding energy of 530.4 eV belongs to the lattice oxygen in the as-deposited nanocolumns. The O 1s peaks at higher binding energy of 531.7 eV in the as-deposited and annealed nanocolumns belong to the chemisorbed oxygen. It is interesting to note the high binding energy peak of O_2 plasma-treated nanocolumns shifts to a much higher value of 532.3 eV. It should be closely related with the increased chemisorbed oxygen on the nanocolumns during intensive O_2 plasma treatment.

The XPS results of SnO_2 nanocolumns array were found to be consistent with that of SnO_2 nanorods array, which was discussed in detail in the previous section 6.2.5.2. The enhanced gas sensing response was due to the introduction of reactive chemisorbed oxygen species on the nanocolumns surface, especially in the case of nanocolumns that were post-treated in the O_2 plasma. The presence of chemisorbed oxygen species gives rise to the large increase in the sensor resistance (as shown in figure 6-27) and thus delivering a better sensing performance than the as-deposited nanocolumns array.

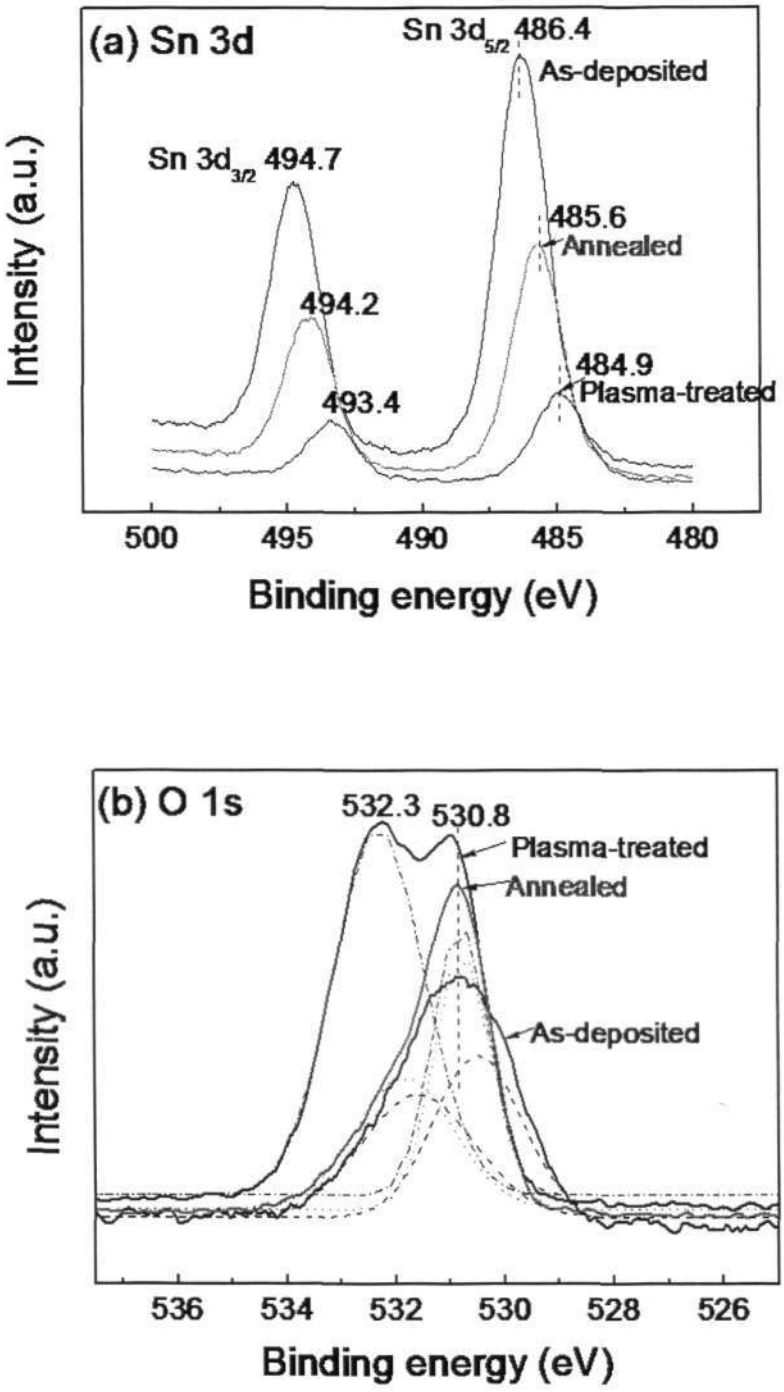

Figure 6-28 (a) Sn 3d peaks and (b) O 1s peaks (solid lines) of as-deposited, annealed and O_2 plasma-treated nanocolumns. The dash lines, dot lines and dash-dot lines are the fitting curves of O 1s peaks of as-deposited, annealed and O_2 plasma-treated nanocolumns, respectively [140].

CHAPTER SEVEN

CONCLUSIONS AND RECOMMENDATIONS

7.1 Conclusions

Nanocrystalline SnO_2 thin films were prepared by the custom-designed ICP-CVD system using bubbler delivery of chemical precursors. The effects of substrate-nozzle distance, RF power, and gas flow ratio of Ar/O_2 on the microstructures, grain size and film thickness were characterized. The gas sensing response of the nanocrystalline SnO_2 thin films deposited at various substrate-nozzle distances was characterized. The nanostructures with different structural parameters were found to influence the resulting gas sensing properties. Hybrid structure of 1-D SnO_2 nanorods formed on 2-D SnO_2 thin films were successfully prepared by subjecting the as-deposited SnO_2 thin films to post plasma treatment using the same ICP-CVD setup. The effects of RF power, gas flow ratio of Ar/O_2, type of plasma on the formation of nanorods were systematically studied. A sputtering-redeposition mechanism was proposed to shed light on the growth of SnO_2 nanorods on 2-D thin films via plasma surface modification. Such findings have put forward exciting opportunities in tailoring the microstructures of the films deposited by the custom-designed ICP-CVD system.

The gas sensing properties of as-deposited and post plasma treated SnO_2 thin films were comparatively studied. The sensitivity to CO, H_2 and ethanol has increased twofold and above, together with a significant decrease in optimal operating temperature up to 130 °C. The better sensitivity achieved with the post plasma treated SnO_2 thin films was attributed to the highly porous structure created by the randomly oriented 1-D nanorods rooted in the 2-D thin films which enabled both analyte and the background gas to access all the surfaces of SnO_2 nanorods as well as the SnO_2 thin film. Surface addition with Pd noble metal was proven to further enhance the sensitivity and selectivity of the nanorods SnO_2 thin film towards H_2 gas in particular with 6 times better sensitivity compared to the un-doped SnO_2 nanorods thin films.

Direct one-step SnO_2 nanorods array was successfully prepared using a reduced flow rate of carrier gas and oxygen into the chamber of ICP-CVD system. The effects of substrate-nozzle distance and RF power on the nanorods array formation were studied and the associated growth mechanism was attributed to the vapor-solid growth, where a seed layer that served as the nucleation sites for subsequent directional growth was formed by the initially deposited molecules. The directional growth along [110] was achieved with the minimum surface energy of crystal face. The gas sensing properties were comparatively studied for as-deposited and Pd-doped SnO_2 nanorods arrays, with the latter showing 6 times better sensitivity to H_2 at a reduced optimal temperature of 400 °C. Post thermal annealed and post oxygen plasma treated SnO_2 nanorods arrays also showed enhanced sensitivity to CO and H_2 compared to the as-deposited samples, especially the 40-minutes post oxygen plasma treated sensor showed 13 times higher sensitivity to H_2. The role of oxygen vacancies and chemisorbed oxygen species for the improved gas sensing properties were substantiated by the XPS characterization

results for the post annealed and post oxygen plasma treated SnO_2 nanorod arrays respectively. With the use of direct liquid injection ICP-CVD, SnO_2 nanocolumn arrays were also successfully prepared in a direct simple manner. The effect of substrate-nozzle distance on the formation of nanocolumn arrays was studied. The gas sensing properties of nanocolumn arrays show similarity with that of the nanorod arrays, where the gas sensing response could be enhanced 7 times after post treatment in oxygen plasma. The role of chemisorbed oxygen in optimizing the gas sensor response was elucidated by the XPS analysis.

7.2 Recommendations for future research

SnO_2 nanostructures prepared by ICP-CVD technique, in particular the hybrid 1-D nanorods SnO_2 thin films and 1-D SnO_2 nanorods and nanocolumns arrays have shown good application as gas sensing materials. Future research work could focus on the study of single 1-D SnO_2 nanorod as nanoscale gas sensor operating at room temperature ambient. The conductivity of the 1-D nanostructures could vary from a fully nonconductive state to a highly conductive state entirely on the basis of the chemistry transpiring at its surface. This could translate to better sensitivity and selectivity properties in terms of chemical sensing. For example, Yang's group reported that the SnO_2 nanoribbon nanosensors can detect ppm-level of NO_2 at room temperature under UV light [23]. Similarly, Xia and co-workers have developed a solution route for the synthesis of SnO_2 nanowires that exhibit enhanced sensitivity towards CO, ethanol, and H_2 at ambient temperature [104]. The SnO_2 nanorods grown by ICP-CVD technique could be fabricated into single nanorod gas sensors and investigated for its room-temperature sensing capabilities. The ultimate goal is to develop a smart single-chip sensor, wherein many sensors, each with its unique

chemical properties, are integrated together and their output signals processed simultaneously.

Some preliminary results in this direction have been obtained where single SnO_2 nanorod gas sensors have been realized using focused ion beam (FIB) technique. Firstly, the SnO_2 nanorods collected from the substrate were ultrasonically dispersed in ethanol and ac dielectrophoresis was utilized to align and manipulate the nanorods on the cross-structured Au/Ti electrodes. Next, both ends of the nanorod were connected to a pair of Au/Ti electrodes via Pt stripes deposited using a Micrion 9500EX Focused Ion Beam system. The fabricated SnO_2 single nanorod gas sensing device is shown in figure 7-1.

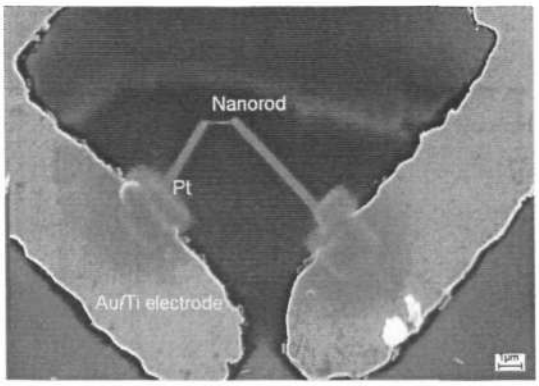

Figure 7-1 SEM image of the single SnO_2 nanorod gas sensing device fabricated by FIB [141].

Figure 7-2 shows the response of the SnO_2 single nanorod gas sensor to 100 ppm H_2. It was found that the nanorod sensor exhibited repeatable response to H_2 at room temperature as shown in figure 7-2(a). At a higher operating temperature of 200 °C, higher sensitivity, reversibility and faster response was achieved (figure 7-2(b)). The sensitivity of the nanorod sensor to other reducing gases such as ethanol, methane, and CO was also evaluated. No obvious response was detected in the range of operating

temperature from ambient to 200 °C. Hence the SnO_2 single nanorod sensor shows good selectivity to H_2 gas. Further enhancement may be realized by surface functionalization with noble metal.

The SnO_2 single nanorod sensor can be further configured as a FET structure with an additional terminal besides the two Au/Ti electrodes that act as source and drain. In such way the Fermi level within the band gap of the nanorod can be varied and used to control the surface process electronically. The nanorod can act as a conductive channel that joins the source and drain electrode. Tuning of the metal oxide properties in a FET configuration has been reported in the literatures [24,142].

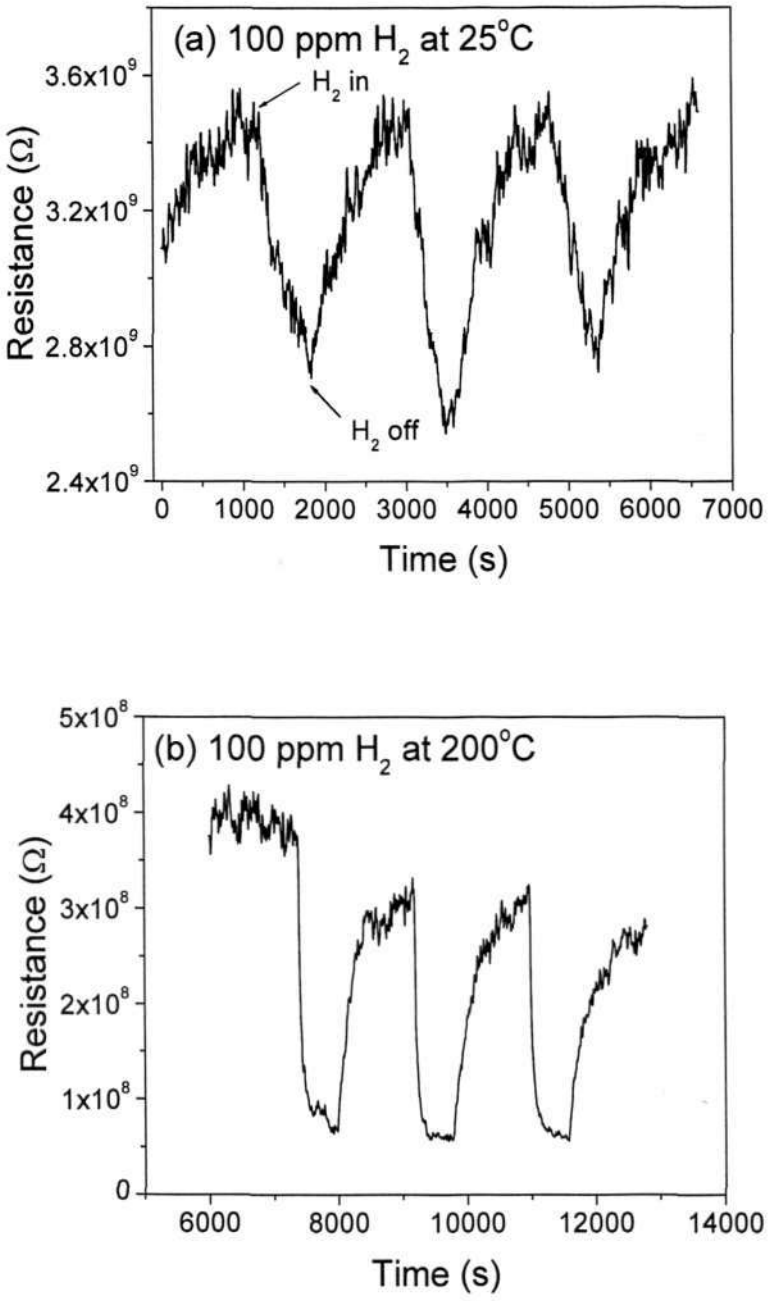

Figure 7-2 The response of the SnO_2 single nanorod gas sensor to 100 ppm H_2 [141].

AUTHOR'S PUBLICATIONS

International Journal Papers:

1. H. Huang, **Y. C. Lee**, C. L. Chow, O. K. Tan, M. S. Tse, J. Guo, T. White, "Plasma treatment of SnO_2 nanocolumn arrays deposited by liquid injection plasma-enhanced chemical vapor deposition for gas sensors", Sensors & Actuators B 138 (2009) 201 – 206.
2. H. Huang, **Y. C. Lee**, O. K. Tan, W. Zhou, N. Peng, Q. Zhang, "High sensitivity SnO_2 single-nanorod sensors for the detection of H2 gas at low temperature", Nanotechnology 20 (2009) 115501.
3. **Y. C. Lee**, Hui Huang, O. K. Tan, M. S. Tse, "Semiconductor gas sensor based on Pd-doped SnO2 nanorod thin films", Sensors & Actuators B 132 (2008) 239-242.
4. **Y. C. Lee**, O. K. Tan, H. Huang, M. S. Tse, H. W. Lau, "SnO_2 nanorods prepared by inductively coupled plasma-enhanced chemical vapor deposition", IEEE Transactions on Nanotechnology 6 (2007) 465-468.
5. **Y. C. Lee**, O. K. Tan, H. Huang, M. S. Tse, "Deposition and gas sensing properties of tin oxide thin films by inductively coupled plasma chemical vapor deposition", Journal of Electroceramics 16 (2006) 507-509.
6. H. Huang, O. K. Tan, **Y. C. Lee**, M. S. Tse, J. Guo, T. White, "In situ growth of SnO_2 nanorods by plasma treatment of SnO_2 thin films", Nanotechnology 17 (2006) 3668 – 3672.
7. H. Huang, O. K. Tan, **Y. C. Lee**, M. S. Tse, J. Guo, T. White, "Effects of plasma treatment on the growth of SnO_2 nanorods from SnO2 thin films", Nanotechnology 17 (2006) 743 – 746.

8. H. Huang, O. K. Tan, **Y. C. Lee**, M. S. Tse, "Preparation and characterization of nanocrystalline SnO_2 thin films by PECVD", Journal of Crystal Growth 288 (2006) 70 – 74.

9. H. Huang, O. K. Tan, **Y. C. Lee**, T. D. Tran, M. S. Tse, "Semiconductor gas sensor based on tin oxide nanorods prepared by plasma-enhanced chemical vapor deposition with postplasma treatment", Applied Physics Letters 87 (2005) 163123.

10. **Y. C. Lee**, O. K. Tan, M. S. Tse, A. Srivastava, "Deposition of nanostructured thin films using an inductively coupled plasma chemical vapor deposition technique", Ceramics International 30 (2004) 1869 – 1872.

Conference Papers:

1. H. Huang, **Y. C. Lee**, O. K. Tan, W. Zhou, N. Peng, Q. Zhang, "Fabrication and sensing properties of SnO_2 single nanorod gas sensors", International Conference on Materials for Advanced Technologies 2007, Symposium E: Nanodevices and Nanofabrication, 1 – 6 July 2007, Singapore.

2. **Y. C. Lee**, O. K. Tan, H. Huang, M. S. Tse, H. W. Lau, "SnO_2 nanorods prepared by inductively coupled plasma-chemical vapor deposition", 6th IEEE Conference on Nanotechnology, 16 – 20 July 2006, Ohio, USA.

3. O.K. Tan, H. Huang, **Y.C. Lee**, M.S. Tse, "Surface modification to improve the gas sensing properties of the SnO_2 thin films", The Asia-Pacific Conference of Transducers and Micro-Nano Technology (APCOT), 25 – 28 June 2006, Singapore.

4. O. K. Tan, H. Huang, **Y.C. Lee**, C. Y. Ong, M. S. Tse, "Surface modification and functionalization of nanostructured SnO_2 thin films for gas sensors", The 11th International Meeting on Chemical Sensors, 16 – 19 July 2006, Brescia,

Italy.

5. H. Huang, O. K. Tan, **Y. C. Lee**, M. S. Tse, Systhesis and characterization of SnO_2 nanorods thin films as gas sensing materials, 2nd MRS-S Conference on Advanced Materials, 18 – 20 Jan 2006, Singapore.

6. **Y. C. Lee,** O. K. Tan, H. Huang, M. S. Tse, "Growth and characterization of SnO_2 nanorod array by plasma-enhanced chemical vapor deposition", 2nd MRS-S Conference on Advanced Materials, 18 – 20 Jan 2006, Singapore.

7. O. K. Tan, **Y. C. Lee**, H. Huang, M. S. Tse, "Synthesis and characterization of SnO_2 nanorods thin films as gas sensing materials", 6th East Asian Conference on Chemical Sensors, 6 – 9 Nov 2005, Guilin, China (Invited).

8. H. Huang, **Y. C. Lee**, O. K. Tan, and M. S. Tse, "Plasma surface modification and gas sensing properties of SnO2 thin films deposited by PECVD", 4th IEEE International Conference on Sensors, Irvine, California, USA, 31 Oct – 3 Nov 2005.

9. H. Huang, **Y. C. Lee**, O. K. Tan, and M. S. Tse, "Preparation and CO gas sensing properties of nanocrystalline SnO2 thin films deposited by PECVD", 9th International Conference on Advanced Materials & ICMAT-2005, Symposium M: Photonics Materials and Devices, 3 – 8 July 2005, Singapore.

10. **Y. C. Lee**, O. K. Tan, H. Huang, M. S. Tse, "Structural and Gas Sensing Properties of SnO_2 thin films by ICP-CVD with post plasma treatment process", 9th International Conference on Advanced Materials & ICMAT-2005, Symposium O: Functional Ceramic Materials and Thin Films, 3 – 8 July 2005, Singapore.

11. H. Huang, **Y. C. Lee**, T. D. Truong, O. K. Tan, M. S. Tse, and X. Yao, "Preparation and enhanced gas sensing properties of SnO_2 thin films with

nanorods prepared by PECVD", 4th Asian Meeting on Electroceramics AMEC-4, 27 – 30 June 2005,.Hangzhou, China.

Book Chapters:

1. Hui Huang, **Yi-Chau Lee** and Ooi-Kiang Tan, "Low-dimensional nanostructured materials for chemical sensing applications" in Handbook of Nanoceramics and Their Based Nanodevices, T. Y. Tseng and H. S. Nalwa, Eds., American Scientific Publishers, Volume 5 (2009) 103-145.
2. Hui Huang, **Yi-Chau Lee**, Hua Gong, Ooi-Kiang Tan, "Growth and Properties of Nanorod Arrays", in Encyclopedia of Nanoscience and Nanotechnology, H. S. Nalwa, Eds., American Scientific Publishers (2008) accepted and in press.

BIBLIOGRAPHY

[1] X. H. Qiu, G. C. Qi, Y. L. Yang, and C. Wang, "Electrostatic characteristics of nanostructures investigated using electric force microscopy", Journal of Solid State Chemistry 181 (2008) 1670-1677.

[2] K. L. Klein, A. V. Melechko, T. E. McKnight, S. T. Retterer, P. D. Rack, J. D. Fowlkes, D. C. Joy, and M. L. Simpson, "Surface characterization and functionalization of carbon nanofibers", Journal of Applied Physics 103 (2008) 061301-061326.

[3] K. Nielsch L. Niinist M. Knez, "Synthesis and surface engineering of complex nanostructures by atomic layer deposition", Advanced Materials 19 (2007) 3425-3438.

[4] Q. Zhang, S.-J. Liu, and S.-H. Yu, "Recent advances in oriented attachment growth and synthesis of functional materials: concept, evidence, mechanism, and future", Journal of Materials Chemistry 19 (2009) 191-207.

[5] F. Chen and J. Chen, "Storage of hydrogen and lithium in inorganic nanotubes and nanowires", Journal of Materials Research 21 (2006) 2744-2757.

[6] G. Kiriakidis, D. Dovinos, and M. Suchea, "Sensing using nanostructured metal oxide thin films", Proc. SPIE 6370 (2006) 63700V

[7] P. V. Kamat, "Quantum dot solar cells. Semiconductor nanocrystals as light harvesters", Journal of Physical Chemistry C 112 (2008) 18737-18753.

[8] L. Zhang and Thomas J. Webster, "Nanotechnology and nanomaterials: Promises for improved tissue regeneration", Nano Today 4 (2009) 66-80.

[9] P. Moriarty, "Nanostructured materials", Reports on Progress in Physics 64 (2001) 297-381.

[10] C. N. R. Rao and A. K. Cheetham, in "Nanomaterials Handbook", Y. Gogotsi, Eds., CRC Press, Boca Raton, 2006.

[11] X. Chen and Samuel S. Mao, "Synthesis of titanium dioxide (TiO_2) nanomaterials", Journal of Nanoscience and Nanotechnology 6 (2006) 906-925.

[12] V. Uskokovic, "Nanomaterials and nanotechnologies: approaching the crest of this big wave", Current Nanoscience 4 (2008) 119-129.

[13] N. Yamazoe and K. Shimanoe, in "Science and Technology of Chemiresistor Gas Sensors", D. K. Aswal and S. K. Gupta, Eds., Nova Science Publishers, New York, 2007.

[14] C. Xu, J. Tamaki, N. Miura, and N. Yamazoe, "Grain size effects on gas sensitivity of porous SnO_2-based elements", Sensors and Actuators B 3 (1991) 147-155.

[15] N. Yamazoe, "New approaches for improving semiconductor gas sensors", Sensors and Actuators B 5 (1991) 7-19.

[16] E. Comini, "Metal oxide nano-crystals for gas sensing", Analytica Chimica Acta 568 (2006) 28-40.

[17] E. Comini, C. Baratto, G. Faglia, M. Ferroni, A. Vomiero, and G. Sberveglieri, "Quasi-one dimensional metal oxide semiconductors: Preparation, characterization and application as chemical sensors", Progress in Materials Science 54 (2009) 1-67.

[18] N. Wang, Y. Cai, and R. Q. Zhang, "Growth of nanowires", Materials Science and Engineering: R: Reports 60 (2008) 1-51.

[19] J. G. Lu, P. Chang, and Z. Fan, "Quasi-one-dimensional metal oxide materials - synthesis, properties and applications", Materials Science and Engineering: R: Reports 52 (2006) 49-91.

[20] C. M. Lieber and Z. L. Wang, "Functional nanowires", MRS Bulletin 32 (2007) 99-104.

[21] E. Comini, G. Faglia, and G. Sberveglieri, "Stable and highly sensitive gas sensors based on semiconducting oxide nanobelts", Applied Physics Letters 81 (2002) 1869-1871.

[22] A. Kolmakov, "The effect of morphology and surface doping on sensitization of quasi-1D metal oxide nanowire gas sensors", Proc. SPIE 6370 (2006) 63700X.

[23] M. Law, H. Kind, B. Messer, F. Kim, and P. Yang, "Photochemical sensing of NO_2 with SnO_2 nanoribbon nanosensors at room temperature", Angewandte Chemie International Edition 41 (2002) 2405-2408.

[24] Y. Zhang, A. Kolmakov, S. Chretien, H. Metiu, and M. Moskovits, "Control of catalytic reactions at the surface a metal oxide nanowire by manipulating electron density inside it", Nano Letters 4 (2004) 403-407.

[25] G. Sberveglieri, C. Baratto, E. Comini, G. Faglia, M. Ferroni, A. Ponzoni, and A. Vomiero, "Synthesis and characterization of semiconducting nanowires for gas sensing", Sensors and Actuators B: Chemical 121 (2007) 208-213.

[26] S. Mathur and S. Barth, "Molecule-based chemical vapor growth of aligned SnO_2 nanowires and branched SnO_2/V_2O_5 heterostructures", Small 3 (2007) 2070-2075.

[27] D. M. Qu, P. X. Yan, J. B. Chang, D. Yan, J. Z. Liu, G. H. Yue, R. F. Zhuo, and H. T. Feng, "Nanowires and nanowire-nanosheet junctions of SnO2 nanostructures", Materials Letters 61 (2007) 2255-2258.

[28] L. C. Tien, S. J. Pearton, D. P. Norton, and F. Ren, "Synthesis and characterization of single crystalline SnO2 nanorods by high-pressure pulsed laser deposition", Applied Physics A: Materials Science & Processing 91 (2008) 29-32.

[29] O. Lupan, L. Chow, G. Chai, H. Heinrich, S. Park, and A. Schulte, "Synthesis of one-dimensional SnO2 nanorods via a hydrothermal technique", Physica E: Low-dimensional Systems and Nanostructures 41 (2009) 533-536.

[30] J.-H. Park, D.-G. Lim, Y.-J. Choi, D.-W. Kim, K.-J. Choi, and J.-G. Park, "Laterally grown SnO_2 nanowires and their NO_2 gas sensing characteristics ", 7th IEEE International Conference on Nanotechnology - IEEE-NANO 2007, Proceedings, Hong Kong, (2007) 1054-1057.

[31] F. Paraguay-Delgado, W. Antúnez-Flores, M. Miki-Yoshida, A. Aguilar-Elguezabal, P. Santiago, R. Diaz, and A. Ascencio, "Structural analysis and growing mechanisms for long SnO_2 nanorods synthesized by spray pyrolysis", Nanotechnology 16 (2005) 688-694.

[32] A. Hulanicki, S. Glab, and F. Ingman, "Chemical sensors definitions and classifications", Pure and Applied Chemistry 63 (1991) 1247-1250.

[33] V. Dermane and R. Sanjinés, in "Gas Sensors - Principles, Operations and Developments", G. Sberveglieri, Eds., Kluwer Academic Publishers, Dordrecht, 1992.

[34] D. E. Williams, "Semiconducting oxides as gas-sensitive resistors", Sensors and Actuators B 57 (1999) 1-16.

[35] W. Brattain and J. Bardeen, "Surface properties of germanium", Bell System Technical Journal 32 (1953).

[36] T. Seiyama, A. Kato, K. Fujishi, and M. Nagatami, "A new detector for gaseous components using semiconductive thin films", Analytical Chemistry 34 (1962) 1502-1503.

[37] N. Taguchi, "Gas detecting device", US Patent 3,695,848 (1970).

[38] S. Matsuura, "New developments and applications of gas sensors in Japan", Sensors and Actuators B 13-14 (1993) 7-11.

[39] Y. Shimizu and M. Egashira, "Basic aspects and challenges of semiconductor gas sensors", Materials Research Bulletin 24 (1999) 18-24.

[40] N. Barsan, M. Schweizer-Berberich, and W. Göpel, "Fundamental and practical aspects in the design of nanoscaled SnO_2 gas sensors: a status report", Fresenius' Journal of Analytical Chemistry 365 (1999) 287-304.

[41] N. Yamazoe, G. Sakai, and K. Shimanoe, "Oxide semiconductor gas sensors", Catalysis Surveys from Asia 7 (2003) 63-75.

[42] H. Ogawa, M. Nishikawa, and A. Abe, "Hall measurement studies and an electrical conduction model of tin oxide ultrafine particle films", Journal of Applied Physics 53 (1982) 4448-4454.

[43] M. Batzill and U. Diebold, "The surface and materials science of tin oxide", Progress in Surface Science 79 (2005) 47-154.

[44] M. E. Franke, T. J. Koplin, and U. Simon, "Metal and metal oxide nanoparticles in chemiresistors: does the nanoscale matter?" Small 2 (2006) 36-50.

[45] T.-H. Jung, S.-I. Kwon, J.-H. Park, D.-G. Lim, Y.-J. Choi, and J.-G. Park, "SnO2 nanowires bridged across trenched electrodes and their gas-sensing characteristics", Applied Physics A: Materials Science & Processing 91 (2008) 707-710.

[46] M.-R. Yang, S.-Y. Chu, and R.-C. Chang, "Synthesis and study of the SnO2 nanowires growth", Sensors and Actuators B: Chemical 122 (2007) 269-273.

[47] G. X. Wang, J. S. Park, M. S. Park, and X. L. Gou, "Synthesis and high gas sensitivity of tin oxide nanotubes", Sensors and Actuators B: Chemical 131 (2008) 313-317.

[48] H. Zhao, Y. Li, L. Yang, and X. Wu, "Synthesis, characterization and gas-sensing property for C_2H_5OH of SnO_2 nanorods", Materials Chemistry and Physics 112 (2008) 244-248.

[49] Z. Ying, Q. Wan, Z. T. Song, and S. L. Feng, "SnO 2 nanowhiskers and their ethanol sensing characteristics", Nanotechnology 15 (2004) 1682.

[50] Y. Shen, T. Yamazaki, Z. Liu, D. Meng, T. Kikuta, N. Nakatani, M. Saito, and M. Mori, "Microstructure and H2 gas sensing properties of undoped and Pd-doped SnO2 nanowires", Sensors and Actuators B: Chemical 135 (2009) 524-529.

[51] N. Van Hieu, H.-R. Kim, B.-K. Ju, and J.-H. Lee, "Enhanced performance of SnO2 nanowires ethanol sensor by functionalizing with La2O3", Sensors and Actuators B: Chemical 133 (2008) 228-234.

[52] Q. Wan and T. H. Wang, "Single-crystalline Sb-doped SnO_2 nanowires: synthesis and gas sensor application", Chemical Communications (2005) 3841-3843.

[53] J. D. Prades, R. Jimenez-Diaz, F. Hernandez-Ramirez, S. Barth, A. Cirera, A. Romano-Rodriguez, S. Mathur, and J. R. Morante, "Ultralow power consumption gas sensors based on self-heated individual nanowires", Applied Physics Letters 93 (2008) 123110.

[54] F. Hernández-Ramírez, A. Tarancón, O. Casals, J. Arbiol, A. Romano-Rodríguez, and J. R. Morante, "High response and stability in CO and humidity measures using a single SnO2 nanowire", Sensors and Actuators B: Chemical 121 (2007) 3-17.

[55] A. Tischner, A. Köck, T. Maier, C. Edtmaier, C. Gspan, and G. Kothleitner, "Tin oxide nanocrystalline films and nanowires for gas sensing applications", Microelectronic Engineering 86 (2009) 1258-1261.

[56] A. Kolmakov, Y. Zhang, G. Cheng, and M. Moskovits, "Detection of CO and O_2 using tin oxide nanowire sensors", Advanced Materials 15 (2003) 997-1000.

[57] F. Hernandez-Ramirez, S. Barth, A. Tarancon, O. Casals, E. Pellicer, J. Rodriguez, A. Romano-Rodriguez, J. R. Morante, and S. Mathur, "Water vapor detection with individual tin oxide nanowires", Nanotechnology 18 (2007) 424016.

[58] D. C. Meier, S. Semancik, B. Button, E. Strelcov, and A. Kolmakov, "Coupling nanowire chemiresistors with MEMS microhotplate gas sensing platforms", Applied Physics Letters 91 (2007) 063118-063113.

[59] A. Kolmakov, X. Chen, and M. Moskovits, "Functionalizing Nanowires with Catalytic Nanoparticles for Gas Sensing Application", Journal of Nanoscience and Nanotechnology 8 (2008) 111-121.

[60] F. Xia, P. Yang, Y. Sun, Y. Wu, B. Mayers, B. Gates, Y. Yin, F. Kim, and H. Yan, "One-dimensional nanostructures: synthesis, characterization, and applications", Advanced Materials 15 (2003) 353-389.

[61] A. Kolmakov and M. Moskovits, "Chemical sensing and catalysis by one-dimensional metal-oxide nanostructures", Annual Review of Materials Research 34 (2004) 151-180.

[62] M. Zheng, G. Li, X. Zhang, S. Huang, Y. Lei, and L. Zhang, "Fabrication and structural characterization of large-scale uniform SnO_2 nanowire array embedded in anodic alumina membrane", Chemistry of Materials 13 (2001) 3859-3861.

[63] H. C. Shin, J. Dong, and M. Liu, "Porous tin oxides prepared using an anodic oxidation process", Advanced Materials 16 (2004) 237-240.

[64] K. H. Wu and S. Y. Lu, "Fabrication of array of nanoporous tin oxide nanorods with electrochemical processes", Electrochemical and Solid State Letters 8 (2005) D9-D11.

[65] T. Hamaguchi, N. Yabuki, M. Uno, S. Yamanaka, M. Egashira, Y. Shimizu, and T. Hyodo, "Synthesis and H_2 gas sensing properties of tin oxide nanohole arrays with various electrodes", Sensors and Actuators B 113 (2006) 852-856.

[66] M. J. Hampden-Smith, T. T. Kodas, and A. Ludviksson, in "Chemistry of Advanced Materials An Overview", L. V. Interrante and M. J. Hampden-Smith, Eds., Wiley-VCH, New York, 1998.

[67] V. Godyak, in "Electron Kinetics and Applications of Glow Discharges", U. Kortshagen and L. D. Tsendin, Eds., Plenum Press, New York, 1998.

[68] W. L. Johnson, in "High Density Plasma Sources: Designs, Physics, and Performance", O. A. Popov, Eds., Noyes Publications, New Jersey, 1995.

[69] A. Anders, J. Pelletier, and D. M. Goebel, in "Handbook of Plasma Immersion Ion Implantation and Deposition", A. Anders, Eds., John Wiley & Sons, New York, 2000.

[70] J. H. Keller, "New and possible future trends in inductively coupled plasma (ICPs) for semiconductor processing", Plasma Physics & Control Fusion 39 (1997) 437-443.

[71] J. E. Stevens, in "Handbook of Advanced Plasma Processing Techniques", R. J. Shul and S. J. Pearton, Eds., Springer, New York, 2000.

[72] B. D. Cullity, Elements of X-ray Diffraction, Addison-Wesley, Reading, 1956.

[73] J. G. Partridge, M. R. Field, J. L. Peng, A. Z. Sadek, K. Kalantar-zadeh, J. D. Plessis, and D. G. McCulloch, "Nanostructured SnO 2 films prepared from evaporated Sn and their application as gas sensors", Nanotechnology 19 (2008) 125504.

[74] C. Luyo, I. Fábregas, L. Reyes, J. L. Solís, J. Rodríguez, W. Estrada, and R. J. Candal, "SnO2 thin-films prepared by a spray-gel pyrolysis: Influence of sol properties on film morphologies", Thin Solid Films 516 (2007) 25-33.

[75] X. Du and S. M. George, "Thickness dependence of sensor response for CO gas sensing by tin oxide films grown using atomic layer deposition", Sensors and Actuators B: Chemical 135 (2008) 152-160.

[76] C. Jin, T. Yamazaki, K. Ito, T. Kikuta, and N. Nakatani, "H_2S sensing property of porous SnO2 sputtered films coated with various doping films", Vacuum 80 (2006) 723-725.

[77] P. Y. Liu, J. F. Chen, and W. D. Sun, "Characterizations of SnO2 and SnO2:Sb thin films prepared by PECVD", Vacuum 76 (2004) 7-11.

[78] Y. Wu, M. Tong, X. He, Y. Zhang, and G. Dai, "Thin film sensors of SnO2-CuO-SnO2 sandwich structure to H2S", Sensors and Actuators B: Chemical 79 (2001) 187-191.

[79] J. Lančok, A. Santoni, M. Penza, S. Loreti, I. Menicucci, C. Minarini, and M. Jelinek, "Tin oxide thin films prepared by laser-assisted metal-organic CVD: Structural and gas sensing properties", Surface and Coatings Technology 200 (2005) 1057-1060.

[80] F. Hellegouarc'h, F. Arefi-Khonsari, R. Planade, and J. Amouroux, "PECVD prepared SnO_2 thin films for ethanol sensors", Sensors and Actuators B: Chemical 73 (2001) 27-34.

[81] S.-K. Song, "Characteristics of SnO_x films deposited by reactive-ion-assisted deposition", Physical Review B 60 (1999) 11137-11148.

[82] S.-K. Song, D. Kim, S. Kim, S.-K. Koh, H.-J. Jung, J.-Y. Lee, and H.-K. Baik, "Structure and chemical characteristics of tin oxide films prepared by reactive-ion-assisted deposition as a function of oxygen ion beam energy", Journal of Materials Research 15 (2000) 1911-1921.

[83] Hui Huang, O. K. Tan, Y. C. Lee, and M. S. Tse, "Preparation and characterization of nanocrystalline SnO2 thin films by PECVD", Journal of Crystal Growth 288 (2006) 70-74.

[84] J. J. Robbins, R. T. Alexander, W. Xiao, T. L. Vincent, and C. A. Wolden, "An investigation of tin oxide plasma-enhanced chemical vapor deposition using optical emission spectroscopy", Thin Solid Films 406 (2002) 145-150.

[85] G. Korotcenkov, "The role of morphology and crystallographic structure of metal oxides in response of conductometric-type gas sensors", Materials Science and Engineering: R: Reports 61 (2008) 1-39.

[86] V. Brinzari, G. Korotcenkov, V. Golovanov, J. Schwank, V. Lantto, and S. Saukko, "Morphological rank of nano-scale tin dioxide films deposited by spray pyrolysis from $SnCl_4.5H_2O$ water solution", Thin Solid Films 408 (2002) 51-58.

[87] P. Méini, F. Parret, M. Guerrero, K. Soulantica, L. Erades, A. Maisonnat, and B. Chaudret, "CO response of a nanostructured SnO_2 gas sensor doped with palladium and platinum", Sensors and Actuators B: Chemical 103 (2004) 111-114.

[88] G. Korotcenkov, V. Macsanov, V. Brinzari, V. Tolstoy, J. Schwank, A. Cornet, and J. Morante, "Influence of Cu-, Fe-, Co-, and Mn-oxide nanoclusters on sensing behavior of SnO2 films", Thin Solid Films 467 (2004) 209-214.

[89] C.-H. Han, S.-D. Han, and S. P. Khatkar, "Enhancement of H_2-sensing properties of F-doped SnO_2 sensor by surface modification with SiO_2", Sensors 6 (2006) 492-502.

[90] Y. Ozaki, S. Suzuki, M. Morimitsu, and M. Matsunaga, "Long-term stability of SnO_2-based CO sensor", Chemical Sensors Supplement B 14 (1998) 125-128.

[91] Y. Ozaki, S. Suzuki, M. Morimitsu, and M. Matsunaga, "Effects of thiourea treatment on the sensing properties and stability of SnO_2-based CO gas sensors", Journal of The Electrochemical Society 147 (2000) 1589-1591.

[92] O. K. Tan, W. Zhu, Q. Yan, and L. B. Kong, "Size effect and gas sensing characteristics of nanocrystalline $x$$SnO_2$-(1-$x$)$\alpha$-$Fe_2O_3$ ethanol sensors", Sensors and Actuators B 65 (2000) 361-365.

[93] T. Hyodo, S. Abe, Y. Shimizu, and M. Egashira, "Gas-sensing properties of ordered mesoporous SnO_2 and effects of coatings thereof", Sensors and Actuators B 93 (2003) 590-600.

[94] Hui Huang, O. K. Tan, Y. C. Lee, T. D. Tran, M. S. Tse, and X. Yao, "Semiconductor gas sensor based on tin oxide nanorods prepared by plasma-enhanced chemical vapor deposition with postplasma treatment", Applied Physics Letters 87 (2005) 163123.

[95] C. Xu, X. Zhao, S. Liu, and Wang. G., "Large-scale synthesis of rutile SnO_2 nanorods", Solid State Communications 125 (2003) 301-304.

[96] Y. Liu, J. Dong, and M. Liu, "Well aligned 'nano-box-beams' of SnO_2", Advanced Materials 16 (2004) 353-356.

[97] L. Vayssieres and M. Graetzel, "Highly ordered SnO_2 nanorod arrays from controlled aqueous growth", Angewandte Chemie International Edition 43 (2004) 3666-3670.

[98] D. Zhang, L. Sun, J. Yin, and C. Yan, "Low-temperature fabrication of highly crystalline SnO_2 nanorods", Advanced Materials 15 (2003) 1022-1025.

[99] Z. Liu, D. Zhang, S. Han, C. Li, T. Tang, W. Jin, X. Liu, B. Lei, and C. Zhou, "Laser ablation synthesis and electron transport studies of tin oxide nanowires", Advanced Materials 15 (2003) 1754-1757.

[100] J. X. Wang, D. F. Liu, X. Q. Yan, H. J. Yuan, L. J. Ci, Z. P. Zhou, Y. Gao, L. Song, L. F. Liu, W. Y. Zhou, G. Wang, and S. S. Xie, "Growth of SnO2 nanowires with uniform branched structures", Solid State Communications 130 (2004) 89-94.

[101] Hui Huang, O. K. Tan, Y. C. Lee, M. S. Tse, J. Guo, and T. White, "In situ growth of SnO_2 nanorods by plasma treatment of SnO_2 thin films", Nanotechnology 17 (2006) 3668-3672.

[102] Hui Huang, O. K. Tan, Y. C. Lee, M. S. Tse, J. Guo, and T. White, "Effects of plasma treatment on the growth of SnO_2 nanorods from SnO_2 thin films", Nanotechnology 17 (2006) 743-746.

[103] N. L. Wu, S. Y. Wang, and I. A. Rusakova, "Inhibition of crystallite growth in the sol-gel synthesis of nanocrystalline metal oxides", Science 285 (1999) 1375-1377.

[104] Y. Wang, X. Jiang, and Y. Xia, "A solution-phase, precursor route to polycrystalline SnO_2 nanowires that can be used for gas sensing under ambient conditions", Journal of the American Chemical Society 125 (2003) 16176-16177.

[105] G. Korotcenkov, "Gas response control through structural and chemical modification of metal oxide films: state of the art and approaches", Sensors and Actuators B 107 (2005) 209-232.

[106] Y. C. Lee, Hui Huang, O. K. Tan, and M. S. Tse, "Semiconductor gas sensor based on Pd-doped SnO2 nanorod thin films", Sensors and Actuators B: Chemical 132 (2008) 239-242.

[107] G. De, A. Licciulli, C. Massaro, A. Quirini, R. Rella, P. Siciliano, and L. Vasanelli, "Sol-gel derived pure and palladium activated tin oxide films for gas-sensing applications", Sensors and Actuators B 55 (1999) 134-139.

[108] G. Korotcenkov, V. Brinzari, Y. Boris, M. Ivanov, J. Schwank, and J. Morante, "Influence of surface Pd doping on gas sensing characteristics of SnO_2 thin films deposited by spray pirolysis", Thin Solid Films 436 (2003) 119-126.

[109] S. H. Kim, K. T. Lee, S. Lee, J. H. Moon, and B.-T. Lee, "Effects of Pt/Pd co-doping on the sensitivity of SnO_2 thin film sensors", Japanese Journal of Applied Physics 41 (2002) L1002-L1005.

[110] V. N. Mishra and R. P. Agarwal, "Sensitivity, response and recovery time of SnO_2 based thick-film sensor array for H_2, CO, CH_4 and LPG", Microelectronics Journal 29 (1998) 861-874.

[111] A. Kolmakov, D. O. Klenov, Y. Lilach, S. Stemmer, and M. Moskovits, "Enhanced gas sensing by individual SnO_2 nanowires and nanobelts functionalized with Pd catalyst particles", Nano Letters 5 (2005) 667-673.

[112] Y.C. Lee, O. K. Tan, Hui Huang, M. S. Tse, and H. W. Lau, "SnO_2 nanorods prepared by inductively coupled plasma-enhanced chemical vapor deposition", IEEE Transaction on Nanotechnology 6 (2007) 465-468.

[113] J. I. Pancove, Optical Processes in Semiconductor, Prentice Hall, New York, 1971.

[114] D. F. Cox, T. B. Fryberger, and S. Semancik, "Oxygen vacancies and defect electronic states on the SnO_2(110)-*1x1* surface ", Physical Review B 38 (1988) 2072-2083.

[115] V. A. Gercher, D. F. Cox, and J.-M. Themlin, "Oxygen-vacancy-controlled chemistry on a metal oxide surface: methanol dissociation and oxidation on SnO_2(110)", Surface Science 306 (1994) 279-293.

[116] M. Batzill, K. Katsiev, and U. Diebold, "Surface morphologies of SnO_2(110)", Surface Science 529 (2003) 295-311.

[117] J. Oviedo and M. J. Gillan, "Energetics and structure of stoichiometric SnO_2 surfaces studied by first-principles calculations", Surface Science 463 (2000) 93-101.

[118] A. Beltrán, J. Andrés, E. Longo, and E. R. Leite, "Thermodynamic argument about SnO_2 nanoribbon growth", Applied Physics Letters 83 (2003) 635-637.

[119] V. Brinzari, G. Korotcenkov, V. Golovanov, J. Schwank, V. Lantto, and S. Saukko, "Morphological rank of nano-scale tin dioxide films deposited by spray pyrolysis from $SnCl_4.5H_2O$ water solution", Thin Solid Films 408 (2002) 51-58.

[120] C. N. R. Rao, F. L. Deepak, G. Gundiah, and A. Govindaraj, "Inorganic nanowires", Progress in Solid State Chemistry 31 (2003) 5-147.

[121] Z. W. Pan, Z. R. Dai, and Z. L. Wang, "Nanobelts of semiconducting oxides", Science 291 (2001) 1947-1949.

[122] H. Z. Zhang, Y. C. Kong, Y. Z. Wang, X. Du, Z. G. Bai, J. J. Wang, D. P. Yu, Y. Ding, Q. L. Hang, and S. Q. Feng, "Ga_2O_3 nanowires prepared by physical evaporation", Solid State Communications 109 (1999) 677-682.

[123] J. M. Blakely and K. A. Jackson, "Growth of crystal whiskers", The Journal of Chemical Physics 37 (1962) 428-430.

[124] G. W. Sears, "A mechanism of whisker growth", Acta Metallurgica 3 (1955) 367-369.

[125] http://srdata.nist.gov/xps.

[126] N. Yamazoe, J. Fuchigami, M. Kishikawa, and T. Seiyama, "Interactions of tin oxide surface with O_2, H_2O and H_2", Surface Science 86 (1979) 335-344.

[127] B. Yea, H. Sasaki, T. Osaki, K. Sugahara, and R. Konishi, "Investigation of substrate-dependent characteristics of SnO_2 thin films with hall effect, x-ray diffraction, x-ray photoelectron spectroscopy and atomic force microscopy measurements", Japanese Journal of Applied Physics 38 (1999) 2103-2107.

[128] H.-C. Chiu and C.-S. Yeh, "Hydrothermal synthesis of SnO_2 nanoparticles and their gas-sensing of alcohol", Journal of Physical Chemistry C 111 (2007) 7256-7259.

[129] K. S. Yoo, N. W. Cho, H. S. Song, and H. J. Jung, "Surface morphology and gas-sensing characterisitcs of SnO_{2-x} thin films oxidized from Sn films", Sensors and Actuators B 24/25 (1995) 474-477.

[130] Z. Tang, G. Jiang, P.C. H. Chan, J. K. O. Sin, and S. S. Lau, "Theory and experiements on r.f. sputtered tin oxide thin-films for gas sensing applications", Sensors and Actuators B 43 (1997) 161-164.

[131] H. Windischmann and P. Mark, "A model for the operation of a thin-film SnO_x conductance-modulation carbon monoxide sensor", Journal of The Electrochemical Society 126 (1979) 627-633.

[132] D. Kohl, "Surface processes in the detection of reducing gases with SnO_2-based devices", Sensors and Actuators 18 (1989) 71-113.

[133] A. M. Azad, S. A. Akbar, S. G. Mhaisalkar, L. D. Birkefeld, and K. S. Goto, "Solid-state gas sensors: a review", Journal of The Electrochemical Society 139 (1992) 3690-3704.

[134] H. Meixner, J. Gerblinger, U. Lampe, and M. Fleischer, "Thin-film gas sensors based on semiconducting metal oxides", Sensors and Actuators B 23 (1995) 119-125.

[135] J. S. Chen, H. L. Li, and J. L. Huang, "Structural and CO sensing characteristics of Ti-added SnO_2 thin films", Applied Surface Science 187 (2002) 305-312.

[136] N. Inagaki, Plasma Surface Modification and Plasma Polymerization, Technomic, Lancaster, 1996.

[137] Y. Kim, C.-H. Yoon, K.-J. Kim, and Y. Lee, "Surface modification of porous nanocrystalline TiO_2 films for dye-sensitized solar cell application by various gas plasmas", Journal of Vacuum Science and Technology A 25 (2007) 1219-1225.

[138] M. Liu and H. K. Kim, "Ultraviolet detection with ultrathin ZnO epitaxial films treated with oxygen plasma", Applied Physics Letters 84 (2004) 173-175.

[139] V. E. Henrich, "The surface of metal oxides", Reports on Progress in Physics 48 (1985) 1481-1542.

[140] Hui Huang, Y. C. Lee, C. L. Chow, O. K. Tan, M. S. Tse, J. Guo, and T. White, "Plasma treatment of SnO_2 nanocolumn arrays deposited by liquid injection plasma-enhanced chemical vapor deposition for gas sensors", Sensors and Actuators B 138 (2009) 201-206.

[141] Hui Huang, Y. C. Lee, O. K. Tan, W. Zhou, N. Peng, and Q. Zhang, "High sensitivity SnO_2 single-nanorod sensors for the detection of H_2 gas at low temperature", Nanotechnology 20 (2009) 115501.

[142] M. S. Arnold, P. Avouris, Z. W. Pan, and Z. L. Wang, "Field-effect transistors based on single semiconducting oxide nanobelts", Journal of Physical Chemistry B 107 (2003) 659-663.